Fabrication of Fresnel Zone Plates for Soft X-Ray and EUV Microscopy by Ion Beam Lithography

Dissertation

zur
Erlangung des Doktorgrades (Dr. rer. nat.)
der
Mathematisch-Naturwissenschaftlichen Fakultät
der
Rheinischen Friedrich-Wilhelms-Universität Bonn

vorgelegt von

Johannes Overbuschmann

geb. Lenz
aus Gnas / Österreich

Bonn 2014

Angefertigt mit Genehmigung der Mathematisch-Naturwissenschaftlichen Fakultät
der Rheinischen Friedrich-Wilhelms-Universität Bonn

1. Gutachter: Prof. Dr. Stefan Linden
2. Gutachter: Prof. Dr. Ulrich Benjamin Kaupp

Tag der Promotion: 21.11.2014

Erscheinungsjahr: 2014

Abstract

Fresnel zone plates are used as lenses for microscopes in the extreme ultraviolet (EUV) and the soft X-ray (SXR) parts of the electromagnetic spectrum. This thesis describes a novel approach for the fabrication of these zone plates using ion beam lithography (IBL) by focused ion beam milling (FIB). Compared to the commonly used methods, IBL simplifies zone plate fabrication to one single step and shows at the same time almost no material limitations. FIB milling is routinely used for many applications in science and technology. However, its beneficial characteristics have not been fully exploited for the fabrication of X-ray optical elements. Within this thesis, gold-palladium zone plates with outermost zone widths of $\Delta r = 121\,\mathrm{nm}$ were fabricated using a standard laboratory FIB system. A drift correction strategy was developed to keep the FIB system stable for the fabrication time of several hours. For the first time IBL-fabricated zone plates were applied in a full field EUV microscope, based on a laser-induced plasma source. The functioning of the zone plates was confirmed by achieving imaging resolutions of $R = 172\,\mathrm{nm}$ at a wavelength of $\lambda = 13\,\mathrm{nm}$. To increase resolution, zone plates were fabricated using an FIB system that has been optimized for lithography applications. Structure sizes could be reduced to 53% of the original value. Zone plates with outermost zone widths of $\Delta r = 64\,\mathrm{nm}$ were fabricated on indium-tin-oxide (ITO) samples and applied in a soft X-ray microscope at $\lambda = 2.3\,\mathrm{nm}$. Imaging resolution of $R = 83\,\mathrm{nm}$ could be achieved at the electron storage ring PETRA III. Freestanding grating structures show the perspective of IBL for the fabrication of 20 nm structures. This seem to be achievable for *Fresnel* zone plates in the near future, which makes IBL a promising new method for the fabrication of X-ray optical elements.

Veröffentlichungen

J. Overbuschmann, J. Hengster, S. Irsen and T. Wilhein
Fabrication of Fresnel zone plates by ion-beam lithography and application as objective lenses in extreme ultraviolet microscopy at 13 nm wavelength
Optics Letters **37**, 5100-5102 (2012)

P. Wessels, M. Schlie, M. Wieland, J. Ewald, G. Abbati, S. Baumbach, **J. Overbuschmann**, T. Nisius, A. Vogel, A. Neumann, A. Meents, J. Viefhaus, H. P. Oepen, G. Meier, T. Wilhein and M. Drescher
XMCD microscopy with synchronized soft X-ray and laser pulses at PETRA III for time-resolved studies
*Journal of Physics: Conference Series **463**, 012023 (2013)*

J. Lenz, N. Krupp, T. Wilhein and S. Irsen
Nanofabrication of Optical Elements for SXR and EUV Applications: Ion Beam Lithography as a New Approach
AIP Conference Proceedings **1365**, 104 (2011)

J. Lenz, T. Wilhein and S. Irsen
Nanofabrication of diffractive elements for soft x-ray and extreme ultraviolet applications using ion beam lithography
Applied Physics Letters **95**, 191118 (2009)

Contents

1 Introduction

Microscopes enable us to see details beyond the limits of the human eye. However, a standard light microscope cannot resolve structures below 200 nm due to the wavelength of visible light. One approach to increase resolution is X-ray microscopy. Modern X-ray microscopes can resolve 20 nm and less [Kirz and Jacobsen, 2009]. Here, no longer the wavelength, but rather the properties of the used lenses determine the achievable resolution.

Glass lenses cannot be used for X-rays due to their low refractive power and high absorption. Instead, *Fresnel* zone plates, a special type of circular diffraction grating are used as lenses instead. A zone plate is a periodic structure, consisting of concentric rings. The distance between two adjacent rings decreases from the center of the zone plate to its outside. The smallest distance between two rings defines the imaging resolution in the X-ray microscope [Michette, 1986].

From the beginnings of X-ray microscopy in the 1970s [Niemann et al., 1974], the fabrication of zone plates has always been one of the key technological problems. Electron beam lithography (EBL) became the method of choice for zone plate fabrication with structures smaller than 20 nm. After selective exposure of an electron resist by the electron beam, the resist structures are transferred to a suitable zone plate material by a combination of etching and plating steps. In 2005, *Chao et al.* realized zone plates with 15 nm structure size [Chao et al., 2005]. Only small improvements have been made since then [Chao et al., 2012, Vila-Comamala et al., 2009, Reinspach et al., 2009]. The main reason for this is the so called »proximity effect«, which will physically limit the structure size to approximately 10 nm. Besides the structure size, the efficiency of a zone plate is a second crucial property. Efficiency depends on the used wavelength in combination with the material of the zone plate. EBL-based processes are only developed for a few metals like gold, nickel and tungsten. Particularly to extend X-ray microscopy to smaller wavelengths, new zone plate materials are needed.

This thesis describes a novel approach for the fabrication of *Fresnel* zone plates using ion beam lithography (IBL) by focused ion beam (FIB) milling. IBL is promising for the following reasons: Firstly, IBL allows zone plate fabrication in one single step. The zones of a zone

plate are directly written into a substrate. Compared to EBL-based processes, structure transfer steps are not needed. Secondly, IBL is not limited by the proximity effect. Thus, the physical limit of ion beam-based processes may be lower compared to EBL. Thirdly, almost all available materials can be processed. IBL works on the principle of sputtering, a process based on the transfer of momentum from an incident ion to a target atom. Additionally, it is easy to use a broad variety of materials for IBL while EBL is only established for few materials. One drawback of the IBL-based approach is the long exposure time that is needed to fabricate zone plates in the FIB system. Compared to EBL, where times are in the range of minutes, IBL-fabricated zone plates are milled within several hours. During that time, drift of the ion beam relative to the zone plate substrate occurs. This drift has to be measured and corrected to avoid zone plate pattern distortion.

Beginning with a description of light-matter interactions for extreme ultraviolet radiation (EUV) and soft X-rays (SXR), the second chapter of this thesis gives an overview of light sources. The most commonly used optical elements in the EUV and SXR spectrum are described before *Fresnel* zone plates are handled. A description of the state of zone plate fabrication technology finishes the chapter. Chapter 3 covers the used materials and experimental methods, namely thin film deposition techniques, FIB systems and laser-induced plasma sources. In chapter 4, experiments on linear diffraction gratings are described briefly. They have been made to show the principle suitability of IBL for the fabrication of X-ray optical elements. Chapter 5 presents the results of zone plate fabrication with a standard laboratory FIB system, as well as experiments with an FIB system optimized for IBL. The zone plates are tested in full-field X-ray microscopes. Within the last chapter, a summary and a discussion of the achieved results are given.

2 Extreme Ultraviolet and Soft X-Ray Radiation

Within the electromagnetic spectrum, the wavelength regimes from 0.1 to 5 nm (photon energies of approx. 10 keV to 250 eV) and from 5 to 40 nm (approx. 250 to 30 eV) are referred to as soft X-ray (SXR) and extreme ultraviolet (EUV) region, respectively. The energies of SXR and EUV photons are in the range of the binding energies of inner shell electrons and are therefore interesting, e.g. for elemental mapping of carbon, nitrogen and oxygen. Unfortunately, these atomic energy levels lead to high absorption for most known materials. This is the main reason to use other optical concepts than in the visible light regime. The transmission of glass lenses for example is insufficient below $\lambda \approx 200\,\mathrm{nm}$. Even gases show strong absorption for EUV and SXR photons. This makes it necessary to perform optical experiments in vacuum. Besides high absorption, the refractive index of many materials is near or below unity. For this reason, optical elements for the SXR and EUV regime are mostly thin structures (thickness $<150\,\mathrm{nm}$), and their working principle is often based on diffraction.

Figure 2.1 shows the electromagnetic spectrum from the infrared down to hard X-rays combined with absorption edges of e.g. silicon and carbon. The regions of ultraviolet (UV) and visible light (VIS) are mainly covered by refractive optical elements. The hard X-ray regime extends the EUV and SXR spectrum on the lower wavelength limit. Here, the light-matter interaction is characterized by less absorption and less phase shift compared to the SXR region, making it even more difficult to find appropriate optical elements.

Natural sources of soft X-rays and EUV radiation are supernova remnants and active galactic nuclei [Voges, 1993]. On earth, the brightest man-made light sources are based on synchrotron radiation, free electron lasers and plasma emission [Attwood, 2007, Michette, 1986].

2.1 Light-Matter Interaction at Short Wavelengths

When X-ray photons interact with matter, several processes are involved: Elastic scattering like *Thomson* scattering from single atomic electrons or *Rayleigh* (coherent) scattering, orig-

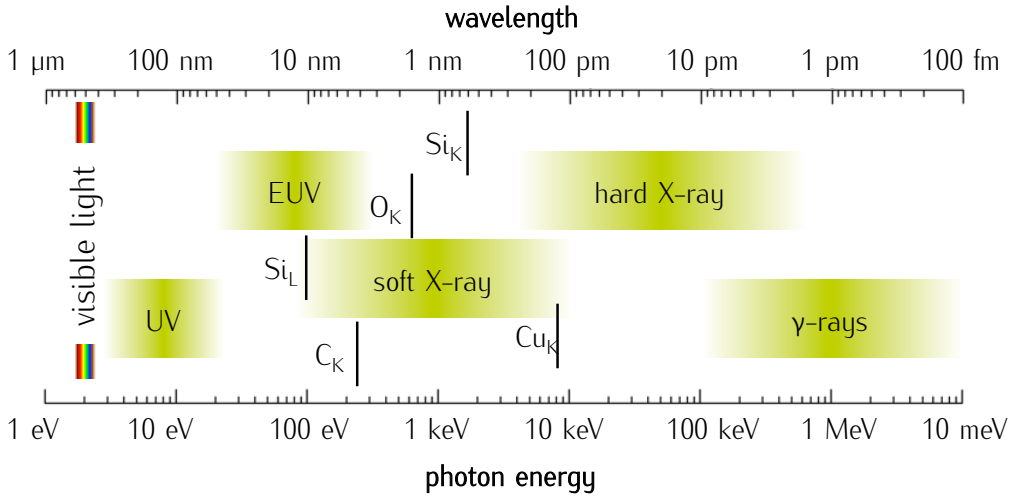

Figure 2.1: Schematic overview of the electromagnetic spectrum from visible light via UV and X-rays down to γ-rays. EUV and SXR photons are shown in combination with absorption edges of silicon (Si_L; 12.5 nm; 99.2 eV and Si_K; 0.67 nm; 1.8 keV), carbon (C_K; 4.37 nm; 284 eV), oxygen (O_K; 2.28 nm; 543 eV) and copper (Cu_K; 0.138 nm; 8.98 keV). Values from [Attwood, 2007].

inating from strongly bound electrons that act cooperatively. Interference effects like *Bragg* diffraction originate from these processes as the phase-relationship between incident and scattered beam stays well defined. Additionally, there are inelastic processes like *Compton* (incoherent) scattering from free (or loosely bound) electrons as well as photoelectric absorption leading to the excitation or ionization of an atom. In the soft X-ray and EUV region, coherent and incoherent scattering contribute less than 1%. Hence, the dominant process is photoelectric absorption [Michette, 1986]. Nevertheless, it is useful to consider all processes to find the complex index of refraction and thus a description for the photon-matter interaction:

Starting from *Maxwells* equations, one can derive the vector wave equation for transverse waves of the form $e^{-i(\omega t - \vec{k}\cdot\vec{r})}$ [Attwood, 2007]:

$$\left(\frac{\partial^2}{\partial t^2} - c^2\nabla^2\right)\vec{E}_T(\vec{r},t) = -\frac{1}{\epsilon_0}\frac{\partial \vec{J}_T(\vec{r},t)}{\partial t}. \tag{2.1}$$

Here, $c \equiv 1/\sqrt{\mu_0 \cdot \varepsilon_0}$ is the vacuum phase velocity of light, $\vec{E}$ describes the electric field and $\vec{J}$ the current density. In case of transverse waves, one considers $\vec{E}$ and $\vec{J}$ to be perpendicular to the wave vector $\vec{k}$. This is indicated by the index T. To generally determine $\vec{J}$, one has to sum up all contributing electrons in the considered volume. For the description of the refractive index for EUV and SXR photons, we only consider scattering in forward

direction, where the phase is conserved and thus the position of individual electrons is irrelevant [Attwood, 2007]. Within these restrictions, the wave equation can be written as

$$\left(\frac{\partial^2}{\partial t^2} - \frac{c^2}{n^2(\omega)} \nabla^2 \right) \vec{E}_T(\vec{r}, t) = 0, \tag{2.2}$$

with the complex refractive index $n(\omega)$, approximated for SXR and EUV frequencies:

$$n(\omega) = 1 - \frac{1}{2} \frac{e^2 n_a}{\varepsilon_0 m} \sum_s \frac{g_s}{(\omega^2 - \omega_s^2) + i\gamma\omega}. \tag{2.3}$$

It describes the sum of all oscillatory motions induced by an electromagnetic wave with frequency ω. The oscillator strength g_s denotes the number of electrons associated with a given resonance frequency ω_s, so that $\sum_s g_s = Z$. Z is the total number of electrons (with mass m) per atom. The number density n_a describes the average number of atoms per unit volume, γ is a dissipative factor and ε_0 the permittivity of vacuum. [Attwood, 2007]

Rewriting equation 2.3 by introducing the classical electron radius

$$r_e = \frac{e^2}{4\pi\epsilon_0 m c^2}$$

and the frequency-dependent atomic scattering factor for forward direction (denoted by the superscript 0)

$$f^0(\omega) = \sum_s \frac{g_s \omega^2}{(\omega^2 - \omega_s^2) + i\gamma\omega} = f_1^0(\omega) - i f_2^0(\omega),$$

leads to a more simple form for $n(\omega)$:

$$n(\omega) = 1 - \frac{n_a r_e \lambda^2}{2\pi} f^0(\omega) = 1 - \frac{n_a r_e \lambda^2}{2\pi} [f_1^0(\omega) - i f_2^0(\omega)] \tag{2.4}$$

In the equation, $f^0(\omega)$ is written in terms of its complex components f_1^0 and f_2^0. The real component f_1^0 is hereby describing the change in phase velocity, whereas the imaginary part f_2^0 changes the amplitude of the wave and is therefore responsible for absorption. Both are highly dependent on the photon energy, especially near absorption edges. For photon energies much higher than the electron binding energy, the scattering behavior is similar to free electrons, f_1^0 approaches Z and f_2^0 goes to zero [Attwood, 2007].

It is common to present the influence of these scattering factors on the complex index of refraction by the substitutes

$$\delta = \frac{n_a r_e \lambda^2}{2\pi} f_1^0(\omega) \qquad \text{and} \qquad \beta = \frac{n_a r_e \lambda^2}{2\pi} f_2^0(\omega). \tag{2.5}$$

This leads to the common representation of the complex index of refraction:

$$n(\omega) = 1 - \delta + i\beta. \tag{2.6}$$

Here, δ describes the phase shift and β the absorption of an electromagnetic wave traveling through matter. Values of f_1^0 and f_2^0, and thus for δ and β at SXR and EUV wavelengths were systematically measured by *Henke et al.* for all elements up to uranium (Z=92). For example, gold at $\lambda = 13\,\text{nm}$ shows values of $f_1^0 = 21.1$ and $f_2^0 = 9.7$, as well as $\delta = 9.4 \cdot 10^{-2}$ and $\beta = 4.3 \cdot 10^{-2}$ [Henke et al., 1993].

To link the complex index of refraction to the propagation of an electromagnetic wave of the form

$$\vec{E}(\vec{r}, t) = \vec{E_0} \cdot e^{-i(\omega t - \vec{k} \cdot \vec{r})} \tag{2.7}$$

we consider the dispersion relation

$$\frac{\omega}{k} = \frac{c}{n} = \frac{c}{1 - \delta + i\beta}. \tag{2.8}$$

Solving for $\vec{k}$ regarding the propagation direction $\vec{k} \cdot \vec{r} = kr$ leads to

$$\begin{aligned} \vec{E}(\vec{r}, t) &= \vec{E_0} \cdot e^{-i[\omega t - (\omega/c)(1-\delta+i\beta)r]} \\ \vec{E}(\vec{r}, t) &= \vec{E_0} \cdot \underbrace{e^{-i\omega(t-r/c)}}_{\text{vacuum propagation}} \cdot \underbrace{e^{-i(2\pi\delta/\lambda)r}}_{\text{phase shift}} \cdot \underbrace{e^{-(2\pi\beta/\lambda)r}}_{\text{decay}}. \end{aligned} \tag{2.9}$$

The first exponential term describes the wave as it would propagate in vacuum whereas the second and third can be identified as terms responsible for phase shift in matter and absorption [Attwood, 2007].

For visible light with photon energies lower than atomic inner shell excitations, the refractive index $(1 - \delta)$ of e.g. glass is >1, enabling effects like focusing of light in refractive lenses or total internal reflection in prisms. At high frequencies (UV and higher) and therefore beyond inner shell resonances, the refractive index can become less than 1, i.e. the phase velocity of EUV and SXR radiation can be larger compared to those observed for the propagation in vacuum. Hence, refractive focusing lenses for X-rays have to be shaped concavely and total external reflection occurs for incidence angles below the critical angle $\theta_c = \sqrt{2\delta}$.

Values of δ and β are very small for most materials in the SXR and EUV region. Due to high absorption, even in gaseous media, it is necessary to place all optical elements, beam paths and detectors in vacuum chambers. Typical 1/e attenuation lengths for metals are smaller than 50 nm and can be calculated as

$$l_{abs} = \frac{\lambda}{4\pi\beta}. \tag{2.10}$$

Figure 2.2 shows absorption lengths of materials that are important for X-ray and EUV microscopy. Particularly interesting for biological applications is the region in between the K-absorption edges of oxygen and carbon, from $\lambda = 2.28\,\text{nm}$ to $4.36\,\text{nm}$: the so called »water window«. Here, water is highly transparent, even at several microns thickness, whereas carbon-containing media like proteins are strongly absorbing. In contrast to electron microscopy, natural contrast is achieved without the need of heavy metal staining or special phase contrast techniques. Longer wavelengths are used if e.g. silicon-containing media is imaged in aqueous environment.

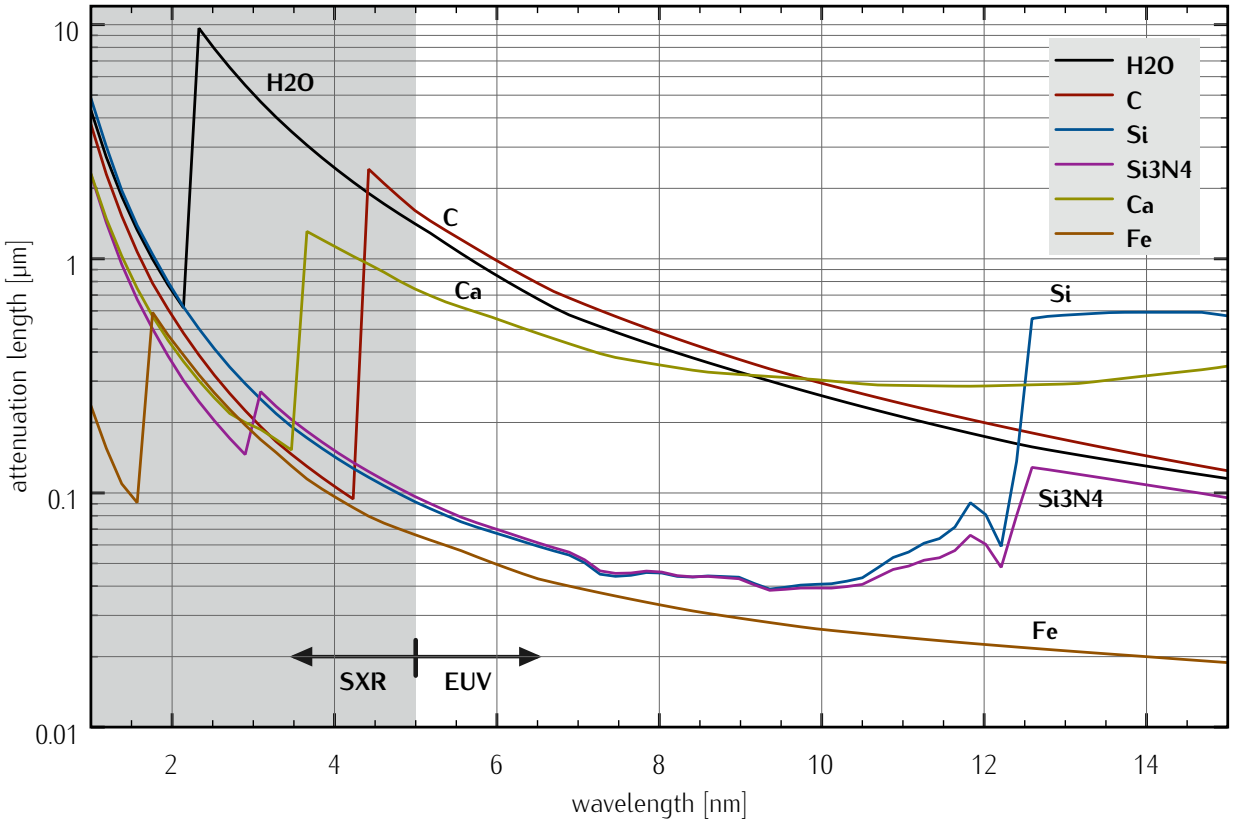

Figure 2.2: Attenuation length of SXR and EUV radiation in water, carbon, silicon, silicon nitride, calcium and iron. Values from [Henke et al., 1993].

2.2 X-ray Sources

Most modern soft X-ray and EUV light sources rely on one of two basic principles: (a) Deflection of fast moving charged particles [Michette, 1986]. This is used in synchrotron facilities, where relativistic electrons with $v \approx 0.99999999 \cdot c$ are forced to change their direction by magnetic fields. (b) Photon emission of atoms or ions, triggered by a change of their atomic excitation state. When an electron is transferred from a higher to a lower electronic state, the difference in energy can be emitted as a photon. The emitted light is spectrally narrow, as the energy differences are discrete.

2.2.1 Synchrotron Radiation

Synchrotron radiation facilities like *PETRA III* in Hamburg or *ELETTRA* in Trieste incorporate storage rings to deflect bunches of electrons at several GeV energies and produce radiation via bending magnets or insertion devices like undulators. Figure 2.3 shows a drawing of an electron storage ring and the schematic path of an electron passing an undulator.

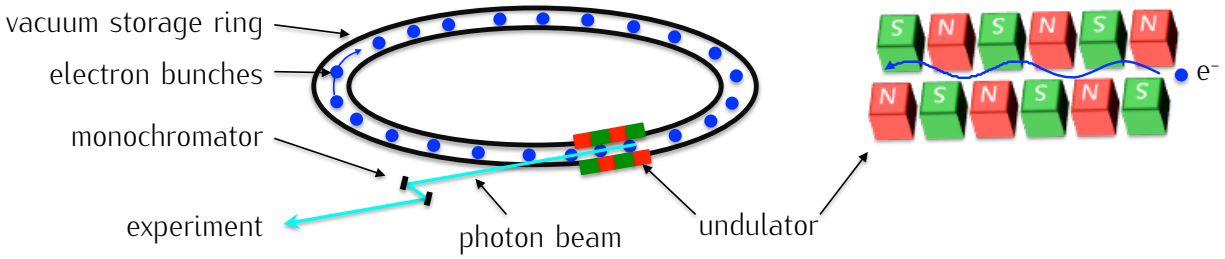

Figure 2.3: Schematic drawings of an X-ray emitting electron storage ring and an undulator. Electrons travel in a ring-shaped vacuum chamber. The electrons are deflected at bending magnets, wigglers, or undulators and emit synchrotron radiation. In undulators, electrons are forced to oscillate within an arrangement of magnets. The so produced light is spectrally filtered at a monochromator and guided to the experiment.

In principle, electron storage rings consist of straight segments, arranged in ring-shape and connected by bending magnets. Storage rings were inherently used for collider experiments. The bending magnets are used to change the propagation direction of the electron beam and were historically the first light sources for synchrotron radiation experiments. The spectrum

emitted from these bending magnets is a broad band of wavelengths. Spectral filtering has to be applied, if narrow bandwidth is needed.

Another possibility to transfer the kinetic energy of the electrons to electromagnetic radiation is the use of »undulators«. They are so-called »insertion devices« placed in the straight segments of the storage ring. Undulators produce much narrower spectral emission and consist of an periodic arrangement of dipole magnets that force the electron beam to perform an oscillation with the wavelength λ_u, corresponding to the periodicity of the magnetic field. The electron will therefore radiate during acceleration, according to a radiating dipole. In the frame of the fast electron passing the magnetic arrangement, its periodicity λ_u will be *Lorentz*-contracted to

$$\lambda' = \frac{\lambda_u}{\gamma}, \tag{2.11}$$

with the *Lorentz* factor

$$\gamma = \frac{1}{\sqrt{1-\beta^2}}. \tag{2.12}$$

Here, $\beta = v/c$ is the relative velocity of the electrons v and the speed of light in vacuum c. The emitted light therefore has the frequency

$$f' = \frac{c}{\lambda'} = \frac{c\gamma}{\lambda_u}. \tag{2.13}$$

For a stationary observer, f' is different due to the *Doppler* shift during emission. The strength of the shift depends on the relative velocity and therefore on the angle of observation θ. For the resulting X-rays, this leads to a radial dependence of the wavelength regarding the beam shape. The influence of the *Doppler* shift on the emitted light frequency, with relativistic effects considered, can be written as

$$f = \frac{f'}{\gamma(1-\beta\cdot\cos\theta)}. \tag{2.14}$$

Only considering the central part of the beam ($\theta = 0$) leads to

$$f = \frac{c}{\lambda_u(1-\beta)}. \tag{2.15}$$

As for electrons traveling near the speed of light $\beta = v/c \simeq 1$, equation 2.12 can be written as $1-\beta \simeq 1/(2\gamma^2)$. The emitted wavelength on the axis of the beam can therefore be calculated to

$$\lambda = \frac{\lambda_u}{2\gamma^2}. \tag{2.16}$$

This describes that the wavelength of the emitted electromagnetic radiation from an undulator depends on the periodicity of the magnetic arrangement and the *Lorentz* factor,

which is mainly a construction parameter of the synchrotron facility. As an example, for an undulator gap of $\lambda_u = 3\,\text{cm}$ and an electron energy of $E_e = 2\,\text{GeV}$ ($\gamma = E_e/mc^2 = 3914$), soft X-ray photons of $\lambda \approx 1\,\text{nm}$ are emitted [Attwood, 2007].

The spectral width of the undulators emission is dependent on the number of periods N the electron is forced to pass. In the central part of the beam ($\theta = 0$) it is given by

$$\frac{\Delta\lambda}{\lambda} = \frac{1}{nN}. \tag{2.17}$$

Here, $n = 1,3,5,\ldots$ denotes the order of interference, indicating that the undulator also emits higher harmonics [Michette, 1986]. Both for bending magnets and undulators, the photons are transported to the respective beam line tangential to the storage ring. In this way, several beam lines for different experimental applications are available at synchrotron radiation facilities.

2.2.2 Plasma Sources

In contrast to synchrotron facilities, laboratory light sources based on hot dense plasma enable similar experiments on laboratory scale at the cost of lower photon flux. The most common methods to ignite plasma for EUV and X-ray purposes are electric discharging or laser-heating [Lebert et al., 1999]. In general, plasma is referred to as one of the four classical states of matter. It describes an electrically neutral state where electrons are found spatially separated from their atomic core [Piel, 2010]. When the electrons and atoms recombine, energy can be dissipated in the form of electromagnetic radiation. The recombination of electrons and atoms can be classified into three different radiating processes [Attwood, 2007]:

Element-specific line emission: Electrons are transferred from one bound state to an energetically more favorable one (bound state to bound state transition). The energy of the emitted photon is determined by the energy difference of the states and therefore also on the periodic number of the respective atom. This form of radiating process is the most important one for laser-induced plasma sources as the out coming spectra are narrow lines ($\lambda/\Delta\lambda \approx 1000$). The spectral lines are broadened due to the finite lifetime of the states (natural line broadening), thermal movement of the affected particles (*Doppler* broadening) and due to collisions during emission (pressure broadening) [Hutchinson, 2002]. The state transitions responsible for X-ray emission are K- and L-shell dominated and thus relatively independent from the chemical bonds of the respective atoms, which are determined by the outer shell properties.

Bremsstrahlung: Originates from the interactions of freely moving electrons, which are deflected in the *Coulomb* field of the ions (free state to free state transition). The amount of energy released is dependent on the deflection angle and therefore on the closest distance between electron and ion. The emitted spectrum is a broad band of frequencies determined by the distribution of electron velocities.

Continuous recombination radiation: A continuous spectrum of frequencies is also produced by the recombination of freely moving electrons of different kinetic energies with ions (free state to bound state transition).

The plasma itself can be seen as a partially or fully ionized gas. It can be described by the interaction of the plasma particles, their positions, velocities and the acting forces originating from electric and magnetic fields, a complex many body problem [Klimontovich, 1967]. Other models average over individual particles and describe the dynamics of a plasma by velocity distributions[1] or by the help of hydrodynamics. Here, the plasma is handled like a fluid and described by parameters of density, temperature and pressure [Piel, 2010, Attwood, 2007].

Using an approach derived from *Planck's* law, one can calculate the required temperature of an ideal black body radiator to emit X-rays. Although a laser-driven plasma is not in thermal equilibrium, *Wien's* displacement law allows estimation of the lower limit of plasma temperature that has to be achieved:

$$\lambda_{max} = \frac{2.898 \cdot 10^6 \,\mathrm{nm\,K}}{T}. \tag{2.18}$$

By this, emission at $\lambda = 2\,\mathrm{nm}$ can be assigned to a temperature of $T \approx 1.5{\cdot}10^6\,\mathrm{K}$ to which a target has to be heated. Laser irradiation on a solid target with intensities of $I > 10^{15}\,\mathrm{W/m^2}$ causes ionization of atoms in a small volume and thus the formation of a »hot dense plasma« [Michette, 1990]. Although the energy of a single photon within the visible light regime ($E_{ph} \approx 2\,\mathrm{eV}$) is not sufficiently high to address inner shell transitions of most materials ($\Delta E > 100\,\mathrm{eV}$), ionization can be achieved. This can be explained by multi-photon processes or by electrons that tunnel out of the *Coulomb* potential of the atom. This is possible, if the potential is reduced by the strong electric field that is applied by the laser [Attwood, 2007].

As plasmas tend to expand and therefore cool down rapidly, high amounts of energy have to be provided. On laboratory-scale, this is only possible for very short periods of time and can be achieved by table-top laser systems with pulse lengths in the nano second range and pulse energies $E > 10\,\mathrm{mJ}$. For describing the energy transfer from a laser to the plasma,

[1] Referred to as the »kinetic description« of a plasma.

the electron plasma frequency ω_p is an important parameter. It is the natural frequency at which electrons in the plasma tend to oscillate [Attwood, 2007]:

$$\omega_p = \sqrt{\frac{e^2 n_e}{\epsilon_0 m}}. \tag{2.19}$$

Here, n_e is the electron density in the plasma, ϵ_0 is the permittivity of vacuum and e and m are the charge and the mass of an electron.

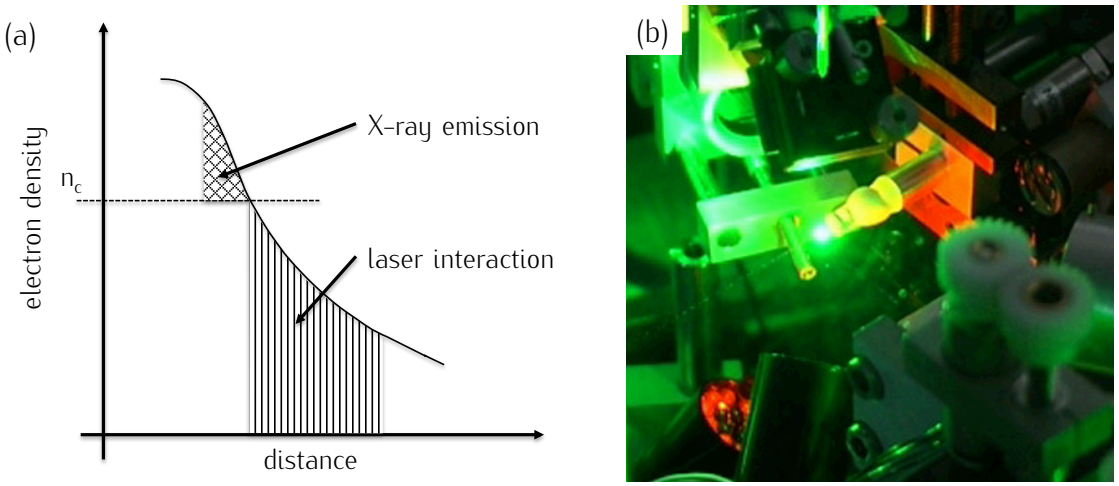

Figure 2.4: (a): Schematic plot of the electron density n_e in a hot dense plasma produced in the focal point of a pulsed laser. As the plasma evolves, a density gradient arises. Laser light can only be absorbed in volumes where the critical electron density n_c is not exceeded. At the critical density, where the laser frequency ω_L matches the natural electron plasma frequency ω_p, light is reflected by the plasma. X-ray emission originates only from volumes slightly above n_c. Scheme adapted from [Attwood, 2007]. (b): Photo showing the visible part of a laser-induced ethanol plasma.

The efficiency of heating up the plasma by a laser is determined by the electron density, the plasma frequency ω_p, and the frequency of the laser ω_L. Only the electrons are relevant, because the much heavier ions can be considered immobile for visible light frequencies. When the plasma is ignited, more and more atoms are ionized, electrons gain kinetic energy by inverse bremsstrahlung and expansion of the plasma starts. This leads to a gradient in electron density, as depicted in figure 2.4. In volumes where the critical electron density n_c is exceeded, photons of the laser cannot propagate any more, as this is only possible for electromagnetic waves with frequencies lower than the plasma frequency $\omega_L < \omega_p$. It

can be shown that the refractive index of the plasma for this case leads to total reflection of the laser light. The majority of X-ray emission occurs slightly beyond the borderline of critical density, where the density is higher and to where energy is transported by radiation and fast moving particles [Attwood, 2007]. Typical values for the critical density in a laser-induced plasma lie in the range of $n_c \approx 10^{21}\,\mathrm{cm}^{-3}$, i.e. at near-solid conditions. To attain intense X-ray and EUV emission on laboratory-scale, the use of solid (copper, tin) or liquid targets (ethanol, liquid nitrogen, water) has been shown to be most effective [Lee et al., 1987, Jansson et al., 2004, Rymell and Hertz, 1993, Berglund et al., 1998, Vogt et al., 2001]. The target is hereby provided to the focused laser as gas puff, liquid jet or solid substrate.

2.3 Optical Elements for X-Rays

This section gives an overview of optical elements that are used to absorb, deflect and focus soft X-rays. Due to the short wavelengths and the resulting high values for absorption and small phase shifts, these optical elements are very different compared to visible light optics.

2.3.1 Filter Elements

For many X-ray optical applications the use of spectral filter elements with a broad absorption characteristic is necessary. For example, at laser-induced plasma sources, the laser light and the visible part of the plasma emission have to be blocked. Especially stray light originating from the laser would otherwise overpower the experiment or even damage the sensitive optical detectors. Additionally, it is often desired (a) to separate different vacuum compartments and (b) to spectrally isolate emission lines. For example at synchrotron facilities, it is useful to separate the beamline vacuum system (pressure typically $<10^{-9}$ mbar) from the experiment vacuum chambers ($\approx 10^{-7}$ mbar).

For the described purposes of vacuum separation and spectral filtering, metal foils (Ti, V, Al, Zr, etc.) with thicknesses of 100 to 400 nm are used as filter elements. The diameter of these foils is determined by the desired beam diameter at the position of the filter element. Typically, this is larger than 5 mm, which makes the foils extremely fragile. Additionally, the foils are sensitive to fast particle bombardment observed as debris at laser-induced plasma sources. This limits their lifetime to some ten hours [Schaefer et al., 2009b]. Foils

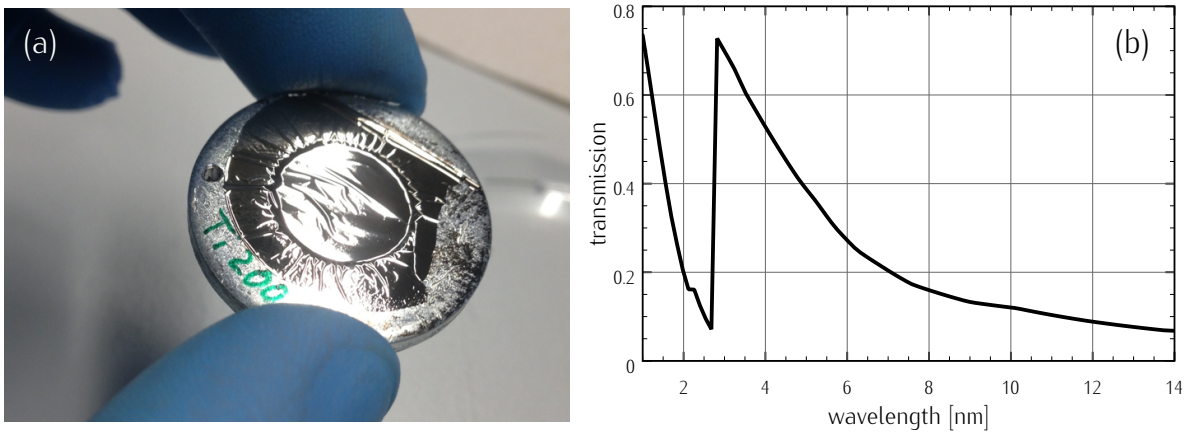

Figure 2.5: (a) Thin titanium foil (thickness 200 nm) and (b) its spectral transmission in the SXR and EUV spectrum. The foil can be used for soft X-ray experiments between $\lambda = 3$ nm and 5 nm. It also acts as filter element for visible light. Transmission data from [Henke et al., 1993].

for common applications and wavelengths are commercially available[2]. Foils for special applications or wavelengths can be fabricated by electron beam evaporation of a layer of NaCl onto a flat glass substrate. Afterwards, the desired metal is deposited onto the NaCl layer. By slowly immersing the glass into water, the salt is dissolved and the thin metal film floats on the water surface due to surface tension. It can be skimmed off by a suitable ring-shaped carrier and mounted on a filter holder like shown in figure 2.5. The depicted foil shows high transmission between λ=3 nm and λ=5 nm and absorbs visible light as well as the remaining soft X-ray and EUV spectrum. Summarizing, these thin foils are used for the following tasks in short wavelength optics:

- Suppression of visible light (stray light and plasma emission)
- Suppression of spectral lines that are not used in the experiment
- Vacuum separation
- Protection of optical components from condensation and fast particles

2.3.2 Multilayer Mirrors

For the interaction of soft X-ray photons with matter, the real part of the complex index of refraction $1 - \delta$ is slightly less than unity and therefore often lower than that of vacuum ($n = 1$). In this case, total external reflection can occur, if the critical angle $\theta_c = \sqrt{2\delta}$ is reached, typically lower than 5° (measured from the surface). This also means that the

[2] For example at Lebow Co., Goleta, CA, U.S.A.

reflection coefficients in normal incidence are negligible for all known single-layer solid materials in vacuum. To overcome this, multilayer mirrors are used in EUV and soft X-ray applications. In principle, they rely on the effect of constructive interference of a high number of weak reflections that sum up to a substantially larger reflection signal.

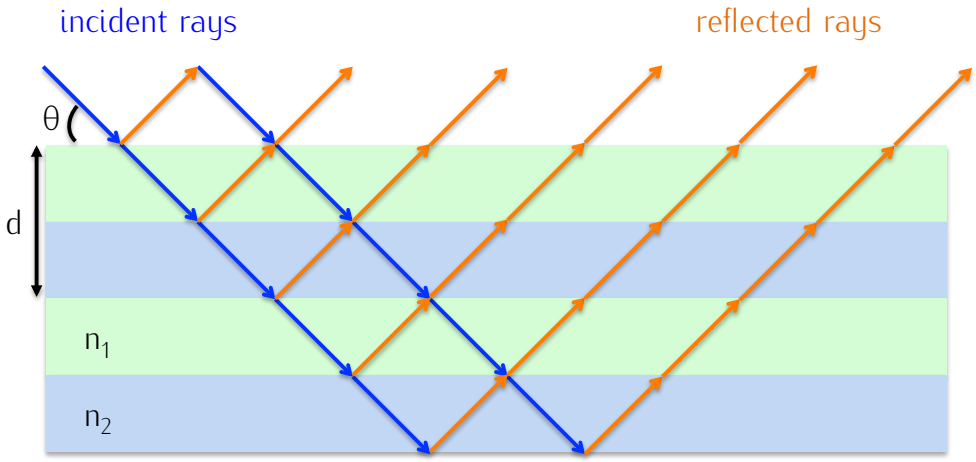

Figure 2.6: Principle of X-ray reflection under the angle θ at a multilayer structure of two materials of refractive indices n_1 and n_2 and period d. Although one single reflection from an interface is very small, the superposition of all reflections results in very high reflection coefficients by constructive interference.

The condition for this effect is similar to the one observed in Bragg reflection of hard X-rays or electrons from crystal planes [Michette, 1986]. Figure 2.6 shows the basic principle of the process. The path difference of two rays (reflected at different interfaces) has to be an multiple of the used wavelength λ, in order to show constructive interference:

$$m\lambda = 2d \cdot \sin\theta. \tag{2.20}$$

Here, d is the period of the multilayer structure and $m = 1, 2, 3, \ldots$ denotes the diffraction order. This condition cannot be fulfilled by crystal planes in the SXR and EUV spectrum, as the typical plane distance is in the range of Å. Therefore, thicker »artificial« crystal planes have to be realized. This is done by alternating layers of different materials ($1-5\,\mathrm{nm}$). The *Bragg* condition for such multilayer structures has to be corrected for the occurring refraction at the material interfaces [Attwood, 2007]:

$$m\lambda = 2d \cdot \sin\theta \sqrt{1 - \frac{4\overline{\delta} d^2}{m^2\lambda^2}}. \tag{2.21}$$

In this equation, $\overline{\delta}$ is the weighted real part of the two materials' refractive indices[3] [Spiller, 1994]. To choose suitable materials, the normal-incidence reflectivity at an interface of two materials with complex refractive indices $n_1 = 1 - \delta_1 + i\beta_1$ and $n_2 = 1 - \delta_2 + i\beta_2$ can be calculated by the *Fresnel* formulas:

$$R_\perp \approx \frac{(\Delta\delta)^2 + (\Delta\beta)^2}{4}. \tag{2.22}$$

Here, $\Delta\delta = \delta_1 - \delta_2$ and $\Delta\beta = \beta_1 - \beta_2$. So, maximum reflectivity can be achieved by alternating layers of materials with high differences in both δ and β.

By these means, plane and curved multilayer mirrors can be fabricated for wavelengths of $\lambda = 1 \ldots 20\,\text{nm}$ by e.g. material combinations of molybdenum and silicon. Typically, these mirrors consist of $N > 20$ periods with which their spectral bandpass gets $\lambda/\Delta\lambda = N^{-1}$ [Attwood, 2007]. Suitable multilayer mirrors can therefore also be operated as monochromating devices. As an example, a MoSi mirror optimized for normal incidence at $\lambda = 13\,\text{nm}$ would have a multilayer period of $d \approx 6\,\text{nm}$ and would show up to 70% reflectivity. Regarding soft X-ray wavelengths, the attainable reflectivity decreases to $< 5\%$ because the thickness of the required layers ($\approx \lambda/4$) gets smaller. At the same time the requirements for the deposition techniques in terms of surface roughness and thickness control increase. So, non-ideal fabrication techniques are the reason for the lower reflectivity at smaller wavelengths.

2.3.3 Diffractive Elements

Optical elements based on diffraction are widely used in soft X-ray and EUV optics as they show high efficiency compared to refractive optics. Gratings are for example used for spectral investigation of plasma emission [Fiedorowicz et al., 1999] or the spectral filtering of synchrotron radiation [Li-Jun et al., 1994]. Fresnel zone plates, the most important substitutes for classic lenses, are used as condenser optics and objective lenses in X-ray microscopes [Vogt et al., 2006, Niemann et al., 1976]. Furthermore, all kinds of diffractive structures are used as key elements for interferometric experiments in the X-ray regime [Lindblom et al., 2007].

Linear gratings are the simplest type of periodic diffractive structure used in X-ray optics. They can be fabricated as transmission gratings for normal incidence and as reflection

[3] $\overline{\delta} = (d_1\delta_1 + d_2\delta_2)/(d_1 + d_2)$ for layer thicknesses d_1, d_2 and real parts of the refractive indices δ_1, δ_2.

gratings for grazing incidence applications. For the work described herein, the spectral characterization of the laser-induced plasma source was performed with a slit grating spectrograph. Therefore, only transmission gratings will be described. For attaining lower total absorption, gratings for soft X-ray and EUV purposes are often fabricated as free standing optics, i.e. no supporting foil (e.g. silicon nitride) is used. Here, the end parts of the grating bars are fixed at a higher order support mesh (see figure 2.7).

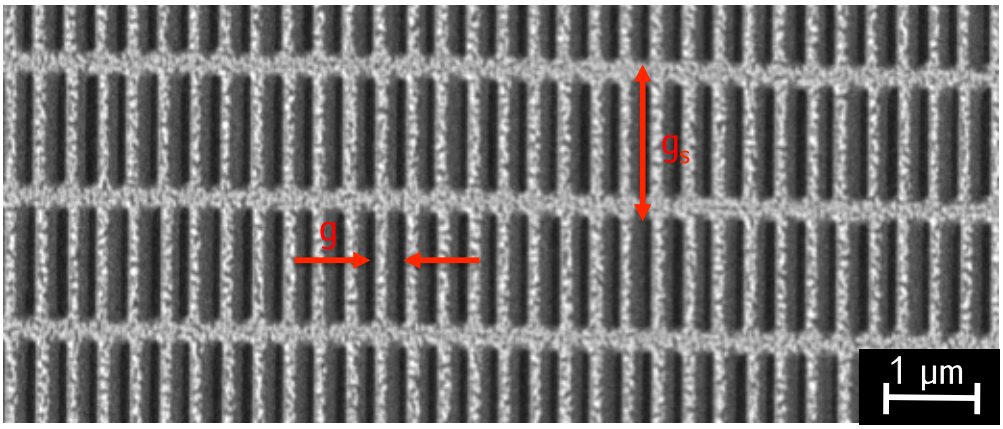

Figure 2.7: Freestanding Si_3N_4 diffraction grating with grating constant g = 363 nm fabricated by ion beam lithography. The grating bars are stabilized by a support structure with g_s=1.5 µm periodicity. [Lenz et al., 2009]

The basic properties of light passing through a diffraction grating can be described by the *Huygens–Fresnel* principle. Each gap of a grating can be seen as a point source of light, so the resulting wavefront is formed by interference of the given point sources. Regarding the path difference of light originating from two neighboring (coherently illuminated) gaps and observed at a fixed point in far field, constructive or destructive interference can occur. Constructive interference can be observed at path differences $d = m\lambda$, i.e. integer multiples of the wavelength λ. As depicted in figure 2.8, this corresponds to angles α for which

$$\sin(\alpha) = \frac{m \cdot \lambda}{g}. \tag{2.23}$$

For $m = 0$, the 0^{th} order of diffraction (DO), photons of all wavelengths pass the grating without being deflected. For all higher orders, the deflection angle α highly depends on the wavelength, leading to the dispersive effect of the grating. As a side effect regarding the soft X-ray and EUV regime, problems can arise because one cannot distinguish between

the diffraction signal from wavelength λ_1 at $m = +2$ and the signal from $\lambda_2 = 2\lambda_1$ at $m = +1$. This effect can be avoided within the free spectral range $FSR = \lambda/m$. The resolving power of linear grating is hereby directly proportional to the used DO and the number of illuminated lines N [Born and Wolf, 1999]:

$$\frac{\lambda}{\Delta\lambda} = m \cdot N. \tag{2.24}$$

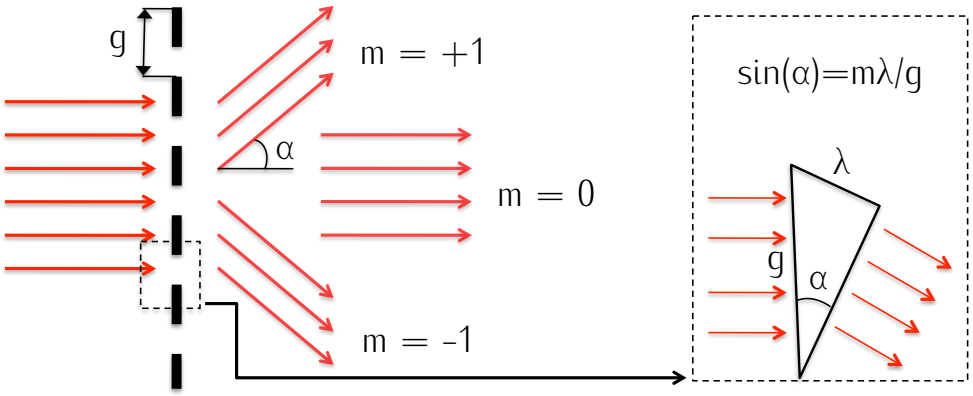

Figure 2.8: Schematic diagram of the diffraction by a linear grating. The deflection angles α for a given wavelength λ depend on the grating constant g and the observed order of diffraction m.

Typical gratings for short wavelength spectroscopy applications show structure sizes lower than 100 nm and consist of several hundreds of metal-coated line pairs, depending on the demands for resolution and efficiency. *Wilhein et al.* showed a slit-grating spectrograph setup for the soft X-ray regime with a resolution of $\lambda/\Delta\lambda > 300$ based on a 40 nm Au-coated Si substrate [Wilhein et al., 1999].

2.4 Fresnel Zone Plates

Refractive lenses cannot be used for soft X-rays and EUV wavelengths. However, *Fresnel* zone plates can be used as substitute. *Fresnel* zone plates are a special form of ring-shaped diffraction gratings with variable periodicity. Figure 2.9 shows a sketch of a zone plate with $N = 50$ alternating zones. The distance between adjacent rings gets smaller with increasing radius, resulting in larger local diffraction angles. One can define the radii in a way that all deflected rays in the first order of diffraction meet at a single point on the optical axis. This point is referred to as the focal point and has a certain distance to the *Fresnel* zone plate, the focal length. Basic investigations of the properties of zone plates were done in 1875 by *Soret* [Soret, 1875]. Zone plates had been used as lenses in X-ray telescopes, before the idea to apply them as optical elements for X-ray microscopy was proposed by *Baez* [Baez, 1952a, Baez, 1952b]. For this kind of application, most of the zone plates are supported by silicon nitride (Si_3N_4) foils of 50 to 100 nm thickness which is stable enough to be used as substrate and at the same time transparent enough for X-ray photons.

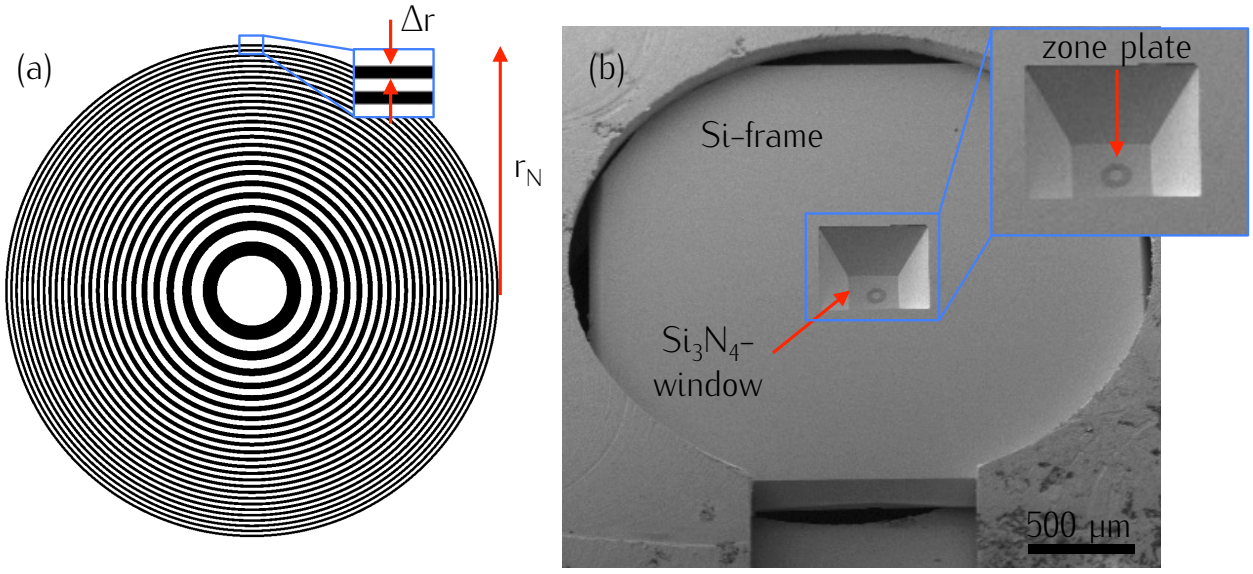

Figure 2.9: (a) *Fresnel* zone plate design with 50 zones, alternating from total absorption to complete transmission of incident light. The zones are determined by their radii r_1 for the first to r_N for the outermost zone. The width of the outermost zone is marked as Δr. (b) Zone plate on a 100 nm thick silicon nitride membrane, supported by a 300 µm silicon frame.

2.4.1 Optical Properties of Fresnel Zone Plates

The optical properties of a zone plate, like focal length, depth of focus or numerical aperture are exclusively defined by the geometric position and width of the zones. To produce a focal spot in the first order of diffraction, it is necessary to deflect the light in a way that the diffraction angle increases from the center of the zone plate to its outside. According to the grating equation $\sin(\alpha) = m\lambda g^{-1}$, this means that the diffracting structures have to get smaller as the radii of the zones increase. As diffraction always shows several orders, one has to consider them for *Fresnel* zone plates too. Higher orders of diffraction produce further focal spots with different focal lengths, as depicted in figure 2.10. For a first description of the optical parameters, only the first order of diffraction is used as it is the brightest and thus the most important one for X-ray microscopy.

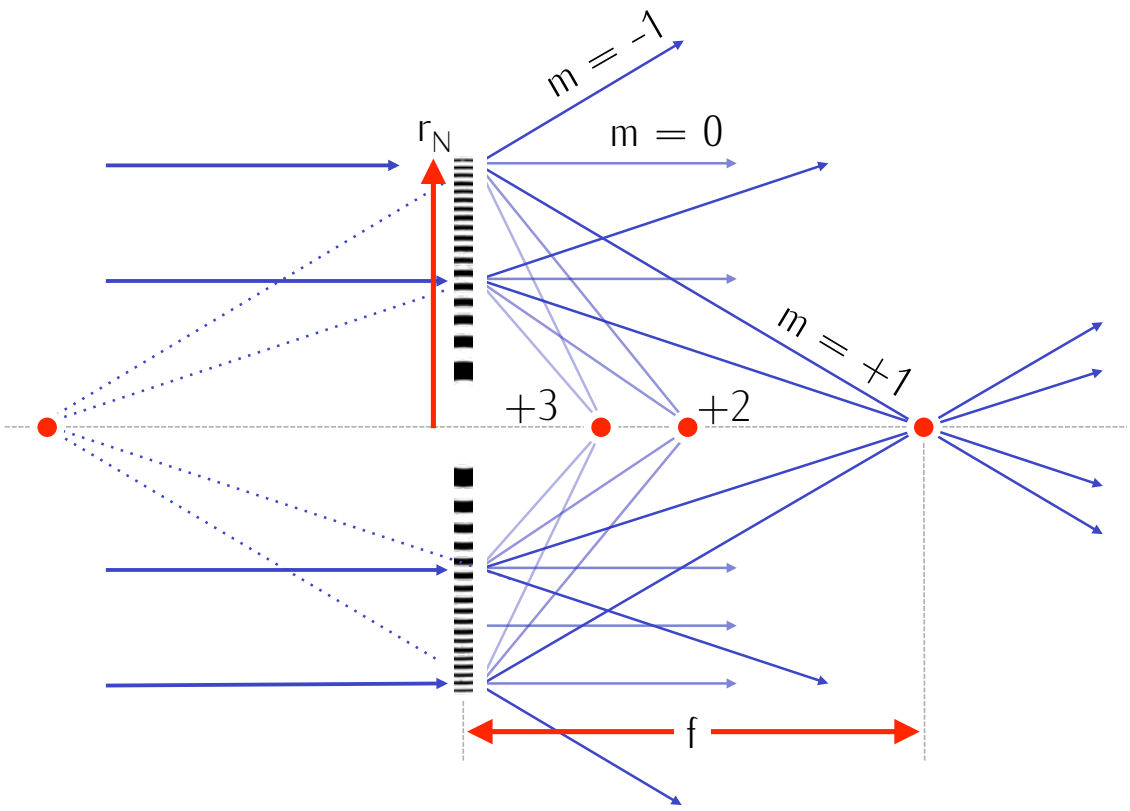

Figure 2.10: A *Fresnel* zone plate, illuminated with parallel light. The positive orders of diffraction $m = 1,2,\ldots$ show real focal points on the optical axis whereas the negative orders diffract the light in a divergent way, producing virtual focal spots.

Considering the formation of a diffractive focal spot as an interference effect, the path difference between two rays, originating from two adjacent zones has to differ by $\lambda/2$.[4] Here, n denotes the zone index from 1 for the first to N for the outermost zone. Taking a simple approach via the *Pythagorean* theorem with the focal length f as the first and the radius of a zone r_n as the second side of the triangle, one can calculate the hypotenuse to [Attwood, 2007]

$$f^2 + r_n^2 = \left(f + \frac{n\lambda}{2}\right)^2. \tag{2.25}$$

By this, the radii of each zone with index n can be calculated to

$$r_n = \sqrt{n\lambda f + \frac{n^2\lambda^2}{4}}. \tag{2.26}$$

For most cases in soft X-ray microscopy the term $n^2\lambda^2/4$, which represents the influence of spherical aberration, can be neglected for zone plates with small numerical apertures or focal lengths $f \gg n \cdot \lambda/2$ [Attwood, 2007]. As the wavelength λ and the focal length f are fixed values, the radii of the zones increase with $\sqrt{n}$. With equation 2.26, the zone plate designs for specific purposes can be calculated. The width of the calculated zones is hereby given by the difference of two neighboring zone boundaries. The limit for most known fabrication processes lies in the minimum achievable structure size. As the minimum structure size of the zone plate Δr determines the maximum achievable resolution in microscopy, it is a crucial parameter. It can be calculated by subtracting the two largest radii $\Delta r = r_N - r_{N-1}$. For large values of $r_N \gg \Delta r$ and after inserting values for radii from equation 2.26, one finds

$$\Delta r \simeq \frac{\lambda f}{D}, \tag{2.27}$$

where

$$D = 2r_N \simeq 4N\Delta r \tag{2.28}$$

is the diameter of the zone plate. Combining equations 2.27 and 2.28, the focal length f can be calculated to

$$f \simeq \frac{D\Delta r}{\lambda} \simeq \frac{4N(\Delta r)^2}{\lambda}. \tag{2.29}$$

Besides the dependence on the total number of zones N and the outermost zone width Δr, the focal length of a zone plate scales with the inverse of the wavelength, indicating strong chromatic aberration. Hence, for most applications *Fresnel* zone plates have to be used with monochromatic light. To avoid image distortions by chromatic aberration, the

[4] The path difference between two rays, originating from two adjacent transparent zones has to differ by λ to obtain constructive interference.

relative spectral bandwidth $\Delta\lambda/\lambda$ has to be smaller than the reciprocal value of the number of zones N:

$$\frac{\Delta\lambda}{\lambda} \leq \frac{1}{N}. \tag{2.30}$$

Regarding imaging applications, the numerical aperture NA of a lens determines parameters like depth of focus or the achievable resolution. It can be calculated similar to refractive lenses as the sine of the half focusing angle:

$$NA = \sin\theta = \frac{r_N}{f} = \frac{D}{2f}. \tag{2.31}$$

With equation 2.27, one can point out that the numerical aperture of a zone plate lens only depends on the used wavelength and the outermost zone width:

$$NA \simeq \frac{\lambda}{2\Delta r}. \tag{2.32}$$

For the depth of focus DOF, this leads to

$$DOF = \pm\frac{1}{2}\frac{\lambda}{(NA)^2} = \pm\frac{2(\Delta r)^2}{\lambda}. \tag{2.33}$$

Hence, for a zone plate with outermost zone width of $\Delta r = 60\,nm$ and a diameter of $D = 100\,\mu m$, used at $\lambda = 2.33\,nm$ wavelength, the DOF is $3\,\mu m$ and the numerical aperture is $NA = 0.019$. The focal length of this zone plate is $f = 2.58\,mm$.

Optical resolution can be defined by the *Rayleigh* criterion. It describes the minimum discernible separation of two mutually incoherent point sources [Attwood, 2007]. For diffraction limited imaging conditions, each of these point sources leads to a pattern called an *Airy* disk. The size of this disk and thus the minimum size of an imaged object depends on the used wavelength and the numerical aperture of the lens. The *Rayleigh* criterion uses the distance of two *Airy* patterns, at which the peak of the first pattern matches with the null of the second one, for defining resolution. For two imaged point objects, monochromatic light and incoherent illumination, this corresponds to an intensity dip of 26.5% or a point distance of

$$R_{Rayl.} = 0.61\frac{\lambda}{NA}. \tag{2.34}$$

Inserting equation 2.32 shows a direct relationship of the achievable resolution and the width of the outermost zone. For a zone plate with $\Delta r = 60\,nm$, one finds:

$$R_{Rayl.} = 1.22 \cdot \Delta r = 73.2\,nm. \tag{2.35}$$

So, the optical resolution directly scales with the width of the outer structures of the zone plate. To judge the resolution in an image experimentally, there are two common

methods. Imaging a sample containing a range of spatial frequencies like a *Siemens* star, or alternatively, a knife-edge test. For this, an image of a sharp edge is acquired and the intensity profile is plotted. Upon comparison, one can show that the *Rayleigh* limit of resolution can be measured by taking the 10% to 90% intensity variation of the imaged edge profile [Attwood, 2007].

2.4.2 Diffraction Efficiency

The diffraction efficiency η_m of a *Fresnel* zone plate is defined as the fraction of incoming light, described by the photon flux Φ_i, which is transported into a certain order of diffraction Φ_m:

$$\eta_m = \frac{\Phi_m}{\Phi_i}. \tag{2.36}$$

It is the fundamental characteristic of a zone plate that defines the exposure time for acquiring an image in an X-ray microscope. A basic theoretic model describing diffraction efficiencies for X-ray gratings was proposed by *Schnopper et al.* [Schnopper et al., 1977]. It can be applied for zone plate structures and describes the limit for diffraction efficiencies in relation to the order of diffraction ($m \neq 0$), the gap-to-period ratio a/g, the thickness of the diffracting structure z, the used wavelength and the material properties defined by the complex index of refraction $n = 1 - \delta + i\beta$:

$$\eta_m = \frac{\sin^2\left(\frac{a}{g} \cdot m \cdot \pi\right)}{m^2\pi^2} \cdot \left[1 + e^{-4\pi z\beta\lambda^{-1}} - 2 \cdot e^{-2\pi z\beta\lambda^{-1}} \cdot \cos\left(\frac{2\pi z\delta}{\lambda}\right)\right]. \tag{2.37}$$

Here, the first term forms the single-slit diffraction pattern whereas the second term describes the interference of the wave traveling through the openings with the phase-shifted and attenuated wave coming through the grating material [Schnopper et al., 1977].

Figure 2.11 shows calculated diffraction efficiencies η related to the gap-to-line ratio a/l for the first three orders of diffraction. In addition to cases in which the zone structures are totally absorbing, cases are shown in which phase-shifting effects are dominant. Calculations for zone plate structures with fully absorbing bars are labeled with »$m = 1$ absor«. For the first order of diffraction the maximum diffraction efficiency of $\eta \approx 10\%$ is obtained with gap-to-line ratios of 1:1 (or gap-to-period ratios of 0.5). The efficiency for the first order of diffraction is the most important for X-ray microscopy because it forms the brightest image in the detection plane. For the described case of zone plates with zones alternating from

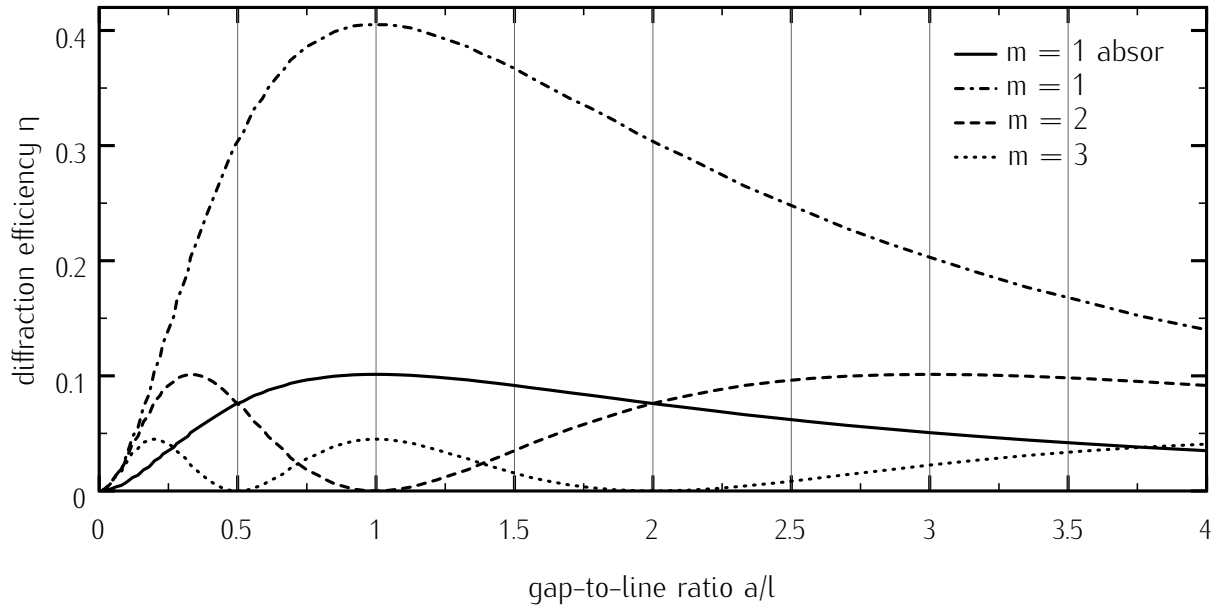

Figure 2.11: Simulated diffraction efficiencies for the first three orders of diffraction (m = 1...3) in dependency of the gap-to-line ratio ($\frac{a}{l}$, $\frac{a}{g} = \frac{a}{a+l}$) of the structures for no absorption ($\beta = 0$) and a phase shift of $z\delta = \lambda/2$. Curve »m = 1 absor« shows the efficiency of a grating with fully absorbing bars.

totally opaque to completely transparent, 50% of the incident light is absorbed, as half of the zone plate area is covered by opaque zones[5]. Half of the transmitted photons, i.e. 25% of the incident light, typically form the 0^{th} order of diffraction (m = 0). Ideally 10% of the photons are deflected to the positive first order (m = +1) and create a real focal spot. For symmetry reasons, an additional fraction of 10% leaves the lens divergently for the first negative order of diffraction (m = -1). These negative orders of diffraction form virtual focal spots, leading to the fact that zone plates always work as collecting and diverging lenses at the same time (see figure 2.10). The remaining photons are distributed to the higher orders of diffraction, again both positive and negative ones.

If phase shifting zones are assumed instead of totally opaque zones an increase of diffraction efficiency can be achieved. The maximum value is reached if the zones shift the phase of the incoming light by a value of $\lambda/2$. For the interference effect in the first order focal spot, this means that two neighboring transparent zones show a path difference of integer multiplies of λ and thus constructive interference. This means that the electric field can be doubled, leading to a factor of four for the observed intensities. Phase zone plates can enhance

[5] In first approximation, the area of each zone is constant across the complete zone plate. So every zone contributes equally to the resulting diffraction signal.

the diffraction efficiency compared to pure amplitude zone plates. Curves for $m = 1, 2, 3$ in figure 2.11 show diffraction efficiencies for such phase shifting zones and the first three positive orders of diffraction. With an ideal phase shift of two neighboring zones of $\lambda/2$ for destructive interference, the theoretical maximum of $\eta_1 = 40\%$ for $m = 1$ can be achieved for the symmetric 1:1 ratio of gaps to lines. Additionally, the even orders ($m = \pm 2, 4, \ldots$) are suppressed for this symmetric case [Attwood, 2007]. For a phase zone plate, there is an ideal combination of material and zone thickness for every desired wavelength. Realistic values for standard zone plates used in X-ray microscopy differ strongly from the ideal values mainly due to surface roughness, non-uniform gap-to-line ratios over the total zone plate area and insufficient accuracy in zone thickness. Experimentally measured values typically deviate by factors of 0.3 to 0.8 from the ideal efficiency values [Bertilson et al., 2007].

2.4.3 Zone Plate Microscopy

After first investigations of *Albert Baez* and *Paul Kirkpatrick* in Stanford around 1950 [Kirkpatrick and Baez, 1948] and the proposal to use soft X-rays for microscopic imaging in the water window by *Hans Wolter* [Wolter, 1952], the group of *Günter Schmahl* in Göttingen constructed the first zone plate-based transmission X-ray microscope [Niemann et al., 1974, Niemann et al., 1976]. A historical review of the field of X-ray microscopy was published by *Janos Kirz* and *Chris Jacobsen* [Kirz and Jacobsen, 2009].

X-ray microscopy can be performed at most synchrotron radiation facilities, for example at *ELETTRA* in Trieste and *BESSY II* in Berlin. Due to the limited access to beamtime at these facilities, laboratory light source-based microscopes have been developed. They utilize the X-ray emission of hot dense plasma as X-ray sources. Here, the photon flux is lower compared to synchrotron-based microscopes, leading to longer exposure times. Several laboratories operate such microscopes for soft X-ray wavelengths [Schaefer et al., 2009a, Benk et al., 2008], even for cryo-applications and tomographic imaging [Hertz et al., 2012, Bertilson et al., 2009, Takman et al., 2007].

Two main types of zone plate-based X-ray microscopes are used in routine operation: Full-field transmission X-ray microscopes (TXM), where a complete image is acquired at one time, and scanning transmission X-ray microscopes (STXM), for which a sample is raster-scanned through the focused X-ray spot. Both types are suitable for laboratory- and synchrotron-based light sources (see Figure 2.12).

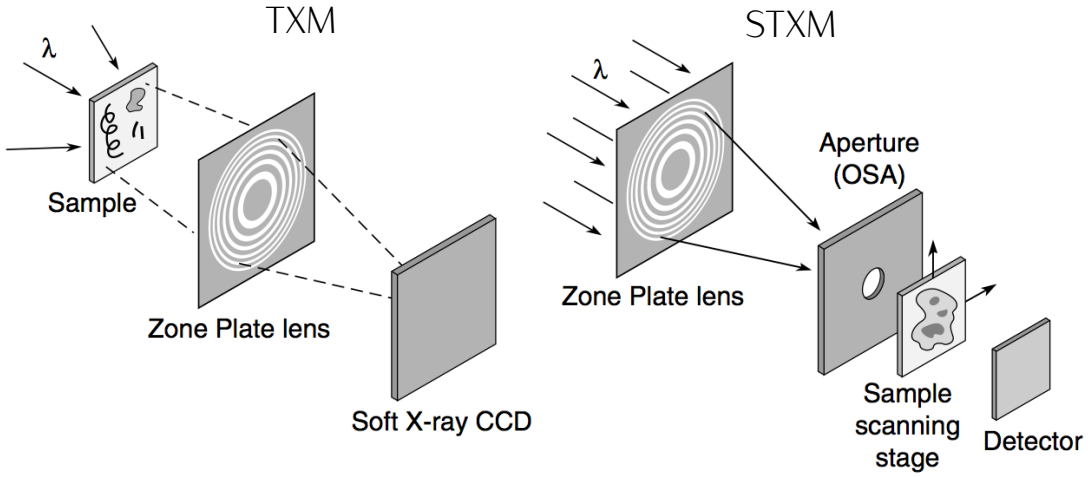

Figure 2.12: Schematic drawings of the two main types of X-ray microscopes: the transmission X-ray microscope (TXM) magnifies a full field image of the specimen to a spatially resolving detector. In a scanning transmission X-ray microscope (STXM) the zone plate creates a small focal spot. In the objective layer, a specimen is raster-scanned through this focal spot and the transmitted number of photons is measured by a photo diode. No spatially resolving detector is required here. Image from [Attwood, 2007].

In a transmission X-ray microscope, a fraction of the specimen (diameter typically smaller than 100 µm) is illuminated by a condenser optic that collects as many photons from the light source as possible [Niemann et al., 1974]. The most common types of condensers currently applied in X-ray microscopes are zone plate condensers [Kaulich et al., 2005], capillary condensers [Guttmann et al., 2009] and multi-layer mirror condensers [Hertz et al., 2012]. At undulator-based beamlines, the spatial coherence properties of the light source cause interference effects that distort the image by the formation of speckles. Additionally, if a zone plate is used as condenser, the image of the source (which is used to illuminate the field of view on the sample) is a diffraction limited spot and thus too small to illuminate a field of e.g. 20 µm in diameter.

Strategies to overcome these problems are the use of vibrating or rotating optical elements that destroy the spatial coherence by averaging [Niemann et al., 2001], or the application of so called »segmented grating condensers« [Vogt et al., 2006]. This concept, shown in figure 2.13, is a derivative of a zone plate condenser, with zone widths approximately equal to the zones of a regular zone plate. The difference is, that the zone plate is segmented into sub-areas. These sub-areas show constant grating spacings and consist of straight (and not curved) grating bars. In contrast to a regular zone plate where all zones contribute to a small, diffraction limited spot, all sub-areas act as regular gratings. Regarding one order of

diffraction, the overlay of the diffracted light forms a homogeneously illuminated area with the size of approximately one segment (»flat-top illumination«). So to say, the focal spot of this approximated zone plate is shaped like a rectangle, allowing large field of views also at undulator-based beamlines.

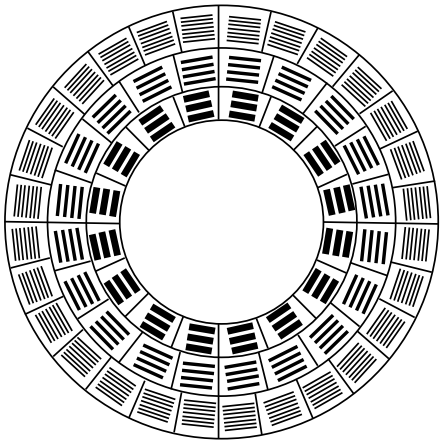

Figure 2.13: Design of a segmented grating condenser to obtain flat-top illumination of a square field at undulator beamlines.

In most cases, the center of the condenser optics is covered by an absorbing layer of metal (see figure 2.14). This so-called »central stop« is used to block the 0^{th} order of diffraction so it cannot pass the optical imaging path and overlay the resulting image as an offset on the detector.

The sample (thickness up to 1 µm) is placed near a pinhole, which acts as a suppressor for stray light and higher orders of diffraction, originating at the condenser. The pinhole also defines the maximum field of view. If polychromatic light is used, the pinhole selects one specific wavelength, as the focal length of the condenser is wavelength-dependent. The pinhole is thus referred to as an »order selecting aperture« (OSA).

In the optical setup, the zone plate lens with typical focal lengths of $f = 0.3 \ldots 5\,\mathrm{mm}$ is placed behind the object. Structures in the objective plane are imaged to the detector (CMOS[6] or CCD[7] detector). If the number of zones exceeds $N = 100$, the properties of zone plate-based imaging can be described by *Newton's* equation for thin refractive lenses [Haase et al., 1997]:

$$f^2 = z \cdot z'. \tag{2.38}$$

[6] Complementary metal-oxide semiconductor
[7] Charge-coupled device

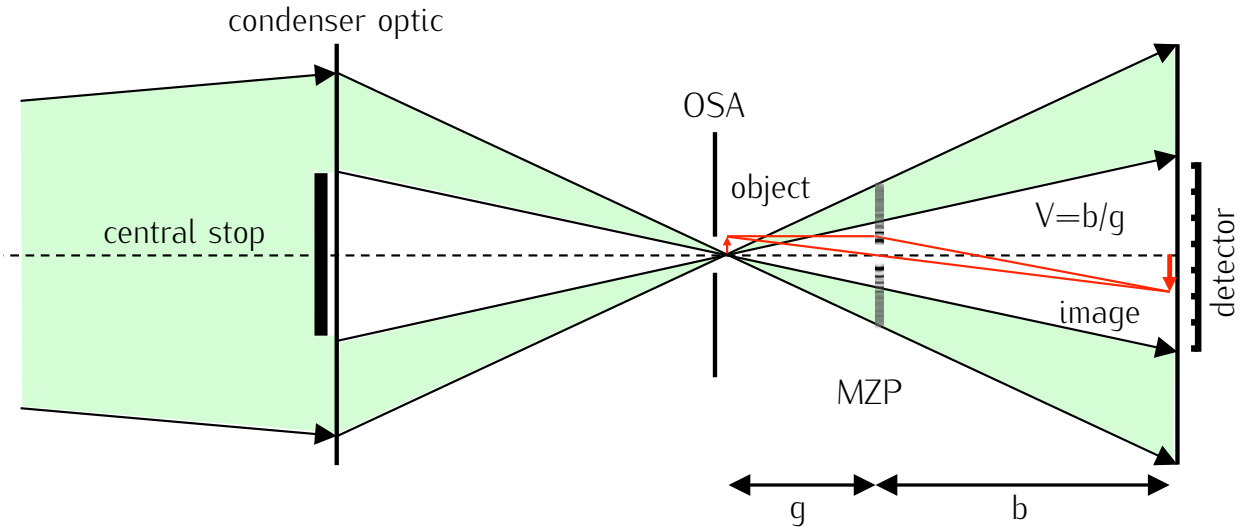

Figure 2.14: Optical setup of a transmission X-ray microscope with condenser, central stop, order selecting aperture (OSA), object, micro zone plate (MZP) and detector. The distance between object and zone plate is marked as g (»object distance«) whereas the distance between the zone plate and the detector is marked as b (image »distance«). The ratio of these values determine the image magnification V.

With the focal length of the lens f, $z = g - f$ and $z' = b - f$, this can be transformed to the thin lens formula for image formation:

$$\frac{1}{f} = \frac{1}{g} + \frac{1}{b}. \tag{2.39}$$

The magnification of the image is hereby given by the ratio of image distance b and object distance g:

$$V = \frac{b}{g}. \tag{2.40}$$

Typically, magnifications of 100-fold to 5,000-fold are used in standard transmission X-ray microscopy.

2.5 State of Fabrication Technology

In the 1960s, almost a century after first investigations of *Fresnel* zone plates by *Soret* [Soret, 1875], *Schmahl* and *Niemann* started to use them as lenses for soft X-ray microscopy [Schmahl and Rudolph, 1969]. Since then, the processes to fabricate the zone plate lenses have always been the limiting factors in imaging resolution.

Holographic fabrication: optical interference patterns

A *Fresnel* zone plate is supposed to focus incoming light into one spot. From holography is known, that the hologram of a single spot is given by a zone plate pattern [Born and Wolf, 1999]. Conversely, if the hologram is reconstructed, the incoming light is focused back to this single spot. This connection was used as first attempt to fabricate zone plates for X-ray microscopy. An interference pattern produced by an Ar^+-laser exposes a photosensitive resist on a suitable X-ray-transparent substrate. Subsequent preparation steps have to be applied to transfer the exposed resist to gold zones [Schmahl et al., 1982].

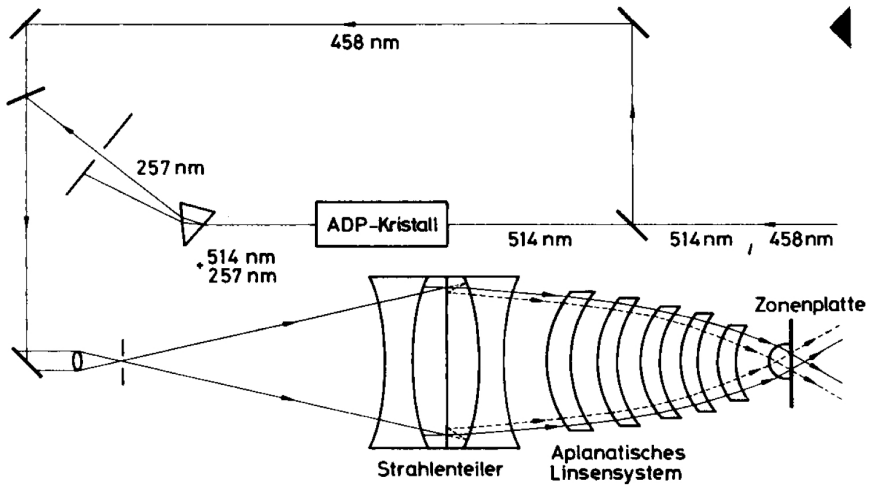

Figure 2.15: Optical setup for the formation of a zone plate-shaped interference pattern, which can be used to expose a photosensitive resist. The interference pattern is formed by two converging beams of 257 nm wavelength at the layer marked with »Zonenplatte«. The 458 nm mode of the Ar^+-laser is used to adjust the setup. The complex compound of lenses corrects for optical aberrations during X-ray microscopy. The optical layout and the properties of all aplanatic lenses have to be re-calculated for every desired zone plate. Image from [Schmahl et al., 1982].

In principle, an interference pattern with the shape of a zone plate can obtained by two converging wavefronts at visible or UV wavelengths. In practice, optical aberrations occur during the formation of the interference pattern. These aberrations reinforce in the X-ray regime due to the shorter wavelengths. Figure 2.15 shows an optical setup that corrects for these aberrations. For every desired zone plate, two aspheric wavefronts have to be calculated and transferred into a set of aplanatic[8] lenses. Zone plates with outermost zone

[8] Lenses that correct for spherical aberration.

widths of approximately 50 nm have been fabricated with this technique. Limits were found within the wavelengths of the used laser. Additionally, it is impractical to completely change the optical setup for every change of zone plate geometry [Schmahl et al., 1982].

Electron Beam Lithography (EBL)

Until now, the most commonly used technique for the fabrication of zone plates is electron beam lithography. A finely focused electron beam (acceleration voltage $U = 5...100\,\mathrm{keV}$) is used to change the chemical structure of a layer of resist, which leads to a change of dissolubility of the layer material in a suitable solvent. To transfer the resist structures into the desired zone plate material, the layer can act as a mold in which e.g. metal can be deposited. Removing this mold leaves only the zone plate structure on the substrate. This technique is capable of delivering smallest outermost zone widths below 15 nm along with highest aspect ratios > 5. To attain such high resolution, the simplified process described above was optimized at all fabrication steps during the last 30 years. This lead to more complex substrate compounds and a higher number of process steps. Limitations for EBL mainly derive from the »proximity-effect« during e-beam exposure. This scattering effect occurs in the resist layer and deflects electrons also to regions not directly exposed to the electron beam. Different strategies to minimize this effect have been developed by mainly three laboratories (see figure 2.16). *Chao et al.* at CXRO[9] in Berkeley show 10 nm imaging resolution by a double-exposure EBL-process in HSQ[10]-resist [Chao et al., 2012, Chao et al., 2009]. Another method was demonstrated by *Reinspach et al.* at BIOX[11] in Stockholm. It is capable of delivering nickel zone plates with 13 nm outermost zone widths by developing ZEP 7000 resist under cryo conditions at -50 °C [Reinspach et al., 2009]. An approach of *Vila-Comamala et al.* from PSI[12] Villigen incorporates the fabrication of a zone plate at half resolution in silicon and the deposition of the actual zone material at both sidewalls of the Si structure by atomic layer deposition (ALD). By that means, zone plates with $\Delta r = 12.5\,\mathrm{nm}$ have been fabricated [Vila-Comamala et al., 2009].

Sliced Zone Plates

A completely different approach is followed for so-called »sliced zone plates«: A cylindrical substrate, e.g. a several micrometer thick gold wire is alternately coated with two materials strongly differing in their X-ray-related properties (see figure 2.17). The local periodicity of the multi-layer coating is chosen according to the radii of an equivalent zone plate as described in equation 2.26. After the multi-layer deposition steps are finished, the outcome

[9] The Center for X-Ray Optics, Lawrence Berkeley National Laboratory
[10] Hydrogen silsesquioxane
[11] Biomedical and X-Ray Physics at KTH AlbaNova
[12] Paul Scherrer Institute

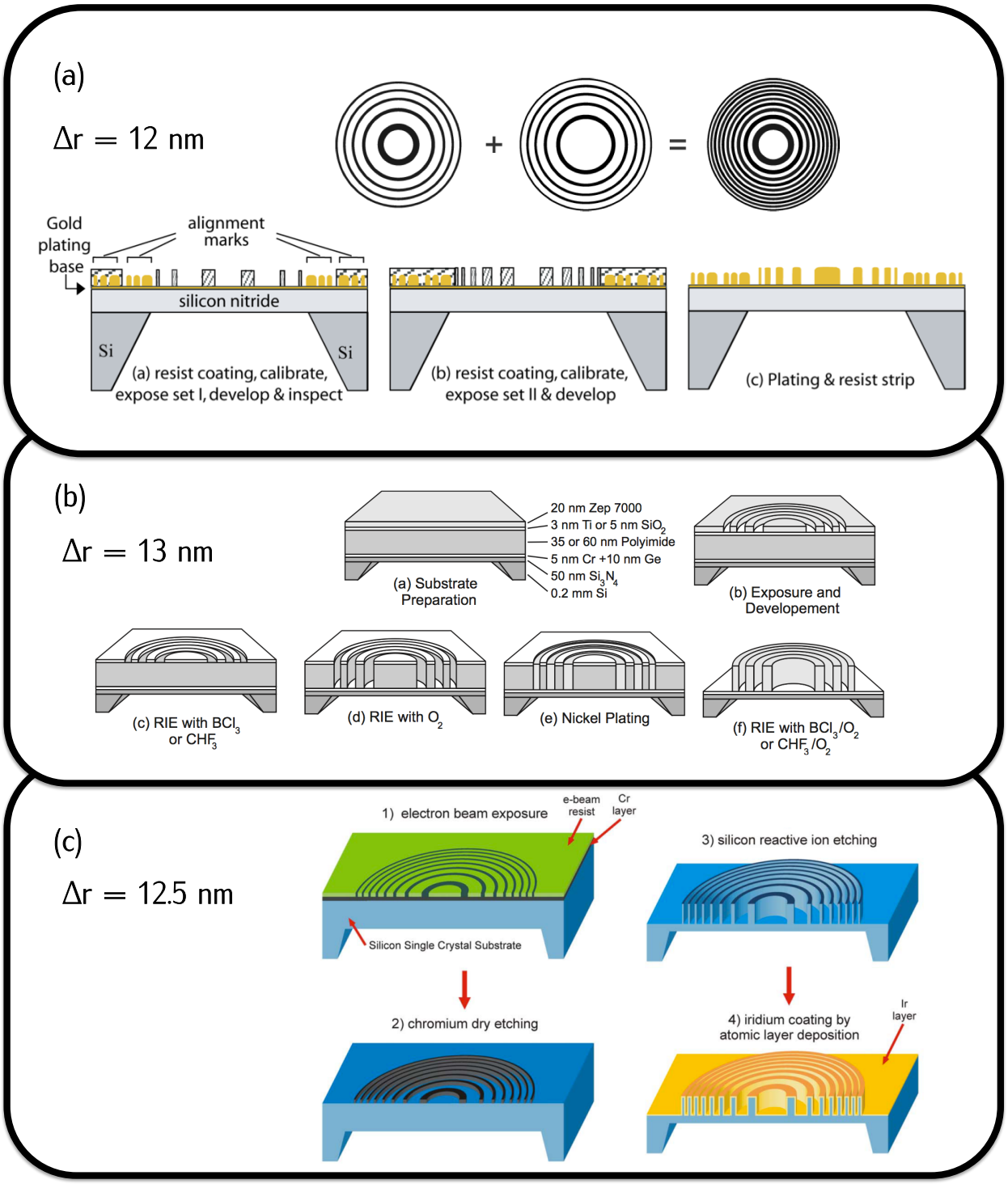

Figure 2.16: Three major EBL-based fabrication processes capable of delivering structure sizes below 15 nm: (a) Double-exposure [Chao et al., 2009]; (b) Cold development of e-beam resist [Reinspach et al., 2009]; (c) Zone-doubled fabrication approach [Vila-Comamala et al., 2009].

is an extremely thick zone plate that can be sliced to the desired ideal thickness. By that means, very high aspect ratios and small outermost structure sizes can be achieved in theory. Starting in the 1980s, first steps towards this method suffered from technological problems in the fields of vapor deposition and high precision cutting methods [Rudolph et al., 1982].

Using atomic layer deposition (ALD) as a deposition method for the zones and focused ion beam milling as slicing method, *Mayer et al.* recently showed zone plates with $\Delta r = 35\,nm$ [Mayer et al., 2011].

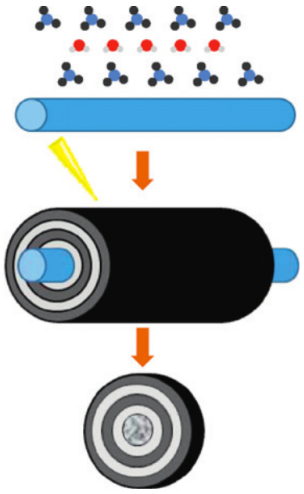

Figure 2.17: Fabrication of sliced zone plates. A substrate wire is alternately coated by atomic layer deposition with two materials of different X-ray optical properties according to the zone plate construction rule. Afterwards the substrate is sliced into a zone plate of desired thickness by focused ion beam machining [Mayer et al., 2011].

Ion Beam Lithography (IBL)

Ion beam lithography uses accelerated ions that are focused on a substrate to directly change the topography of the surface [Stevie et al., 2005]. In principle, the ion beam deflection works similar as for EBL systems but with several orders of magnitude larger momentum of the used particles. The momentum that can be transferred from an incident ion to an atom of the exposed substrate is sufficiently high to eject several atoms out of its surface. This is utilized for ion beam lithography. The surface topography is changed without the detour of structure transfer from an exposed resist over structured resist to the actual zone plate. The idea to use focused ion beam (FIB) instruments to fabricate *Fresnel* zone plates was firstly described by *Ilinski et al.* [Ilinski et al., 2001]. They have been able to fabricate a $\Delta r = 170\,nm$ zone plate on TaSiN-coated silicon wafer. As their FIB system was only able to address a 4096 x 4096 pixel field, the out coming zone plate had a diameter of 60 µm and 142 zones. It was not tested in an X-ray imaging setup, which is crucial for the proof of functioning for a zone plate.

The idea was revived by *Surpi et al.* in 2007. They showed a zone plate with $\Delta r = 100\,nm$ and 38 zones, which would have been enough to act as a diffractive element, but too little to act as a lens. Additionally, the zone plates were been fabricated on bulk substrates, which is the second reason why they could not be tested in an imaging setup [Surpi et al., 2007]. Recently, ion beam-based fabrication of *Fresnel* zone plates was performed by *Keskinbora et al.*, showing a $\Delta r = 100\,nm$ zone plate for scanning hard X-ray microscopy [Keskinbora et al., 2013a]. They also showed a novel approach for the single-pass fabrication of the outer zones of a lens with $\Delta r = 50\,nm$ [Keskinbora et al., 2013b]. Full field imaging in the soft X-ray and EUV regime has not been shown until now.

3 Materials and Experimental Methods

This chapter provides an overview of the used technical equipment. Thin film preparation techniques are described, namely magnetron sputtering and thermal/e-beam evaporation. These deposition methods have been used to create suitable zone plate substrates based on silicon nitride membranes.[13] Furthermore, a general description of focused ion beam (FIB) systems is given before the two FIB microscopes used for zone plate patterning are explained in detail. As last part, an ethanol-based laser-induced plasma source is described. The plasma acts as laboratory-scale light source for the EUV microscope.

3.1 Thin Film Deposition

The thickness of a zone plate with maximum diffraction efficiency mainly depends on the used material and the desired wavelength (see 2.4.2). Typical thicknesses for metal-based zones plates are in the range of 50 to 300 nm. Accurate focused ion beam structuring strongly depends on a smooth and flat surface to start with. So, the demands to the deposition techniques are high. In contrast to EBL-based zone plate fabrication, where the desired zone material is filled into a structured mold, the zone material for IBL-based fabrication has to be deposited on the membrane substrate before ion beam exposure.

The most common methods for thin film deposition are special types of either »physical vapor deposition« (PVD) or »chemical vapor deposition« (CVD). Both have in common that solid matter is transferred into a vapor state in vacuum and condensation of the vapor leads to a thin solid layer. The process is referred to as CVD, if the vapor is the product of chemical reactions. Typical processes in this category are plasma-enhanced CVD (PECVD) or atomic-layer CVD (ALCVD). If the vapor is produced by physical processes like heating (thermal energy) or ion bombardment (momentum transfer), the processes are classified as PVD. The most common types are based on the evaporation of a solid or molten target or on sputtering processes, where atoms/ions of a solid target are vaporized by fast particles [Freund and Suresh, 2009]. As methods of choice for the zone plates described in this thesis, magnetron sputtering and electron beam evaporation were used since they are available in

[13] Silicon nitride membranes are commercially available from Silson Ltd, Blisworth, Northampton, England.

most electron microscopy laboratories, work for a broad range of zone materials and are capable of producing flat and smooth surfaces.

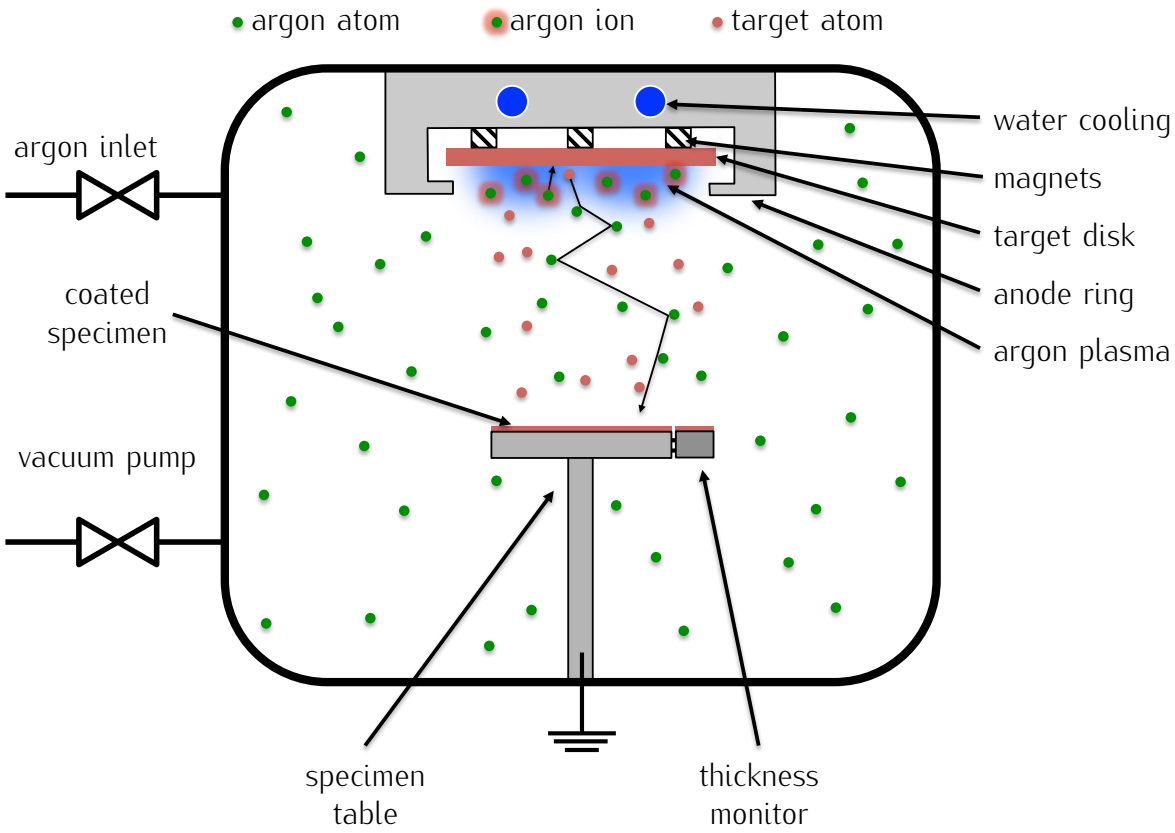

Figure 3.1: Principle of magnetron sputtering as found in the sputter coater *Bal-Tec MED-020*. A ring-shaped plasma is ignited beneath a disk-shaped target. Argon is used as working gas. A plasma is created by applying high-voltage between anode ring and target. Argon is ionized and accelerated towards the target disk from which atoms are ejected by transfer of momentum. The target atoms reach the specimen table after several collisions and condense on the sample. Thickness monitoring can be done via an oscillating quartz sensor.

For magnetron sputtering, an argon plasma is created by applying high voltage between the target disk (or rod, dependent on the geometry of the coating device) and the substrate. As depicted in figure 3.1, Ar^+ ions are accelerated towards the target and eject atoms out of the target surface. After numerous collisions with the present residual argon atoms in the vacuum chamber, the target atoms have lost kinetic energy and condense on the substrate surface. The incidence angles are broadly spread, leading to a uniform coating thickness,

even if the substrate is not flat. The design of the magnetron stabilizes the plasma near the target and traps free electrons that would otherwise also reach the substrate and would cause heating.

At chamber pressures of 2 to $5 \cdot 10^{-2}$ mbar, the mean free path of an sputtered atom is approximately 5 mm, leading to tens of collisions at standard working distances[14] around 50 mm. After these collisions, the kinetic energy of the particles has been reduced to ≈ 1 eV (from starting energies of 10 to 40 eV), which is in the range of thermal evaporation. At lower pressures, fewer collisions occur because of the higher mean free path lengths, leading to higher kinetic energies and more directed sputtering [Bal-Tec AG, 2000, Bunshah, 1994]. For the experiments described within this thesis, sputter coaters of the type *Bal-Tec MED 010* and *MED 020* were used. Both systems are equipped with a quartz crystal monitor to measure the sputter rate and the thickness of the deposited layer. Knowing the density of the sputtered materials, the sputter rate can be calculated by measuring the change in oscillation frequency of the quartz crystal.

As second method for thin film deposition, thermal and electron beam-induced evaporation has been used. Here, the target material is (totally or locally) heated up to temperatures higher than its evaporation temperature in vacuum. Heat can be induced by either resistance heating of the material itself or by electron beam irradiation [Ohring, 1991]. Dependent on the used material, sublimation or evaporation lead to metal vapor which condensates on the substrate. The respective phase transitions are addressed by suitable pressure and temperature combinations. Typical values for metals are $T = 500 - 3500\,°C$ at pressures of $P = 10^{-4} - 10^{-7}$ mbar. For the experiments described in this thesis, an *UNAXIS BAK 640* coating system has been used for the deposition of indium tin oxide (ITO).

3.2 Focused Ion Beam Systems

The principles of a focused ion beam (FIB) microscope is similar to these of scanning electron microscopy (SEM). A focused beam of particles is raster-scanned over a sample. Pixel wise, a gray value is assigned according to the number of electrons ejected from the samples surface (secondary electrons and backscattered electrons). By this, an image of the surface can be acquired. Here, the achievable resolution mainly depends on the size of the particle beam. For FIB microscopes, in which a beam of ions is focused onto the sample, the higher

[14] Distance between target and substrate.

mass of the particles compared to electrons can additionally be used to induce a sputtering process to change the topography of a samples surface.

FIB instruments are widely used for a broad range of tasks in science as well as in industry. They offer the possibility of material removal and deposition with nanometer precision in combination with high-resolution imaging. The development of FIB systems was initially driven by semiconductor industry, where failure analysis, process monitoring and also defect removal have become standard procedures carried out by FIB systems [Yao, 2007].

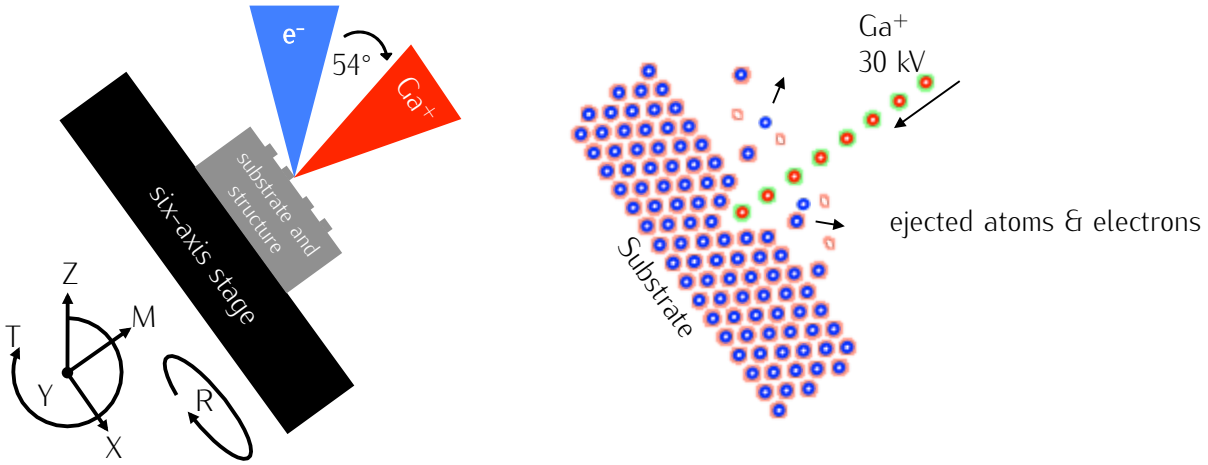

Figure 3.2: Schematic drawing of a typical FIB system and illustration of the ion-solid interactions. The sample is placed on a six-axis stage, which can be tilted perpendicular to the incident ions. The focal spot produced by the electron column is congruent with the ion column's spot. When gallium ions hit the surface, atoms of the substrate are ejected from the surface. This effect can be utilized to change the topography of a sample. As in scanning electron microscopy, secondary electrons are ejected at the same time. So, ion-induced imaging can also be performed, but with the limitation that every image acquisition removes a layer of the surface.

In biology and material science, FIB systems/microscopes have become crucial tools in the field of transmission electron microscopy (TEM) to cut thin sections (»lamellae«) out of larger samples. So called »CrossBeam« or »DualBeam« FIB instruments combine the imagining capabilities of scanning electron microscopes with an ion column for FIB-based nano structuring and enable applications like block face imaging to attain tomographic sets of bulk samples (see figure 3.2) [Inkson et al., 2001, Matthijs De Winter et al., 2009].

A standard FIB microscope uses gallium[15] ions (Ga^+). They are evaporated from a »liquid metal ion source« (LMIS). A continuous stream of particles is formed and accelerated to typically 30 keV by electric fields, corresponding to ion velocities of $3 \cdot 10^5\,\mathrm{m\,s^{-1}}$. Electrostatic lenses focus the gallium ion beam to a spot on the sample surface. The electron beam from the electron column is also focused to this point to enable real time SEM observation of the milled area. The typical field in which the focal spot of the ion beam can be moved has an edge length of smaller than 500 µm [Yao, 2007].

3.2.1 Ion-Matter Interaction

When a Ga^+ ion accelerated by a voltage of 30 kV hits the surface of a substrate, several interaction processes occur. The most important are sputtering, emission of secondary electrons, displacement of target atoms, ion backscattering and excitement of phonons and plasmons. Having a momentum of $3.4 \cdot 10^{-20}\,\mathrm{kg\,m/s}$, ion-induced processes can differ from the ones observed in electron-matter-interaction. A common effect observed for electrons as well as ions is the emission of secondary electrons (SE). The incident particle transfers a sufficient amount of kinetic energy to overcome the binding energy of a bound electron, which can leave the surface. These SEs are detected by a scintillator crystal and a photomultiplier tube placed inside the vacuum chamber or within the electron column itself. Comparing ions to electrons as shown in table 3.1, ions have a larger SE-yield. Typically, one ion generates 1 to 2 secondary electrons that can be detected whereas one electron only generates 0.5 – 0.75 SEs on an average[16].

Theoretically, the transfer of energy from an ion to the atoms of the target can be classified into nuclear and electronic losses. Nuclear energy loss, which is the most important interaction for FIB milling, occurs due to collisions of the incident ion with the target atoms due to their charges. These elastic two-body interactions can be described by *Rutherford*-scattering. Nuclear losses are responsible for the ion-matter interactions in an FIB system that force substrate atoms to leave the surface (»sputtering«). Electronic losses on the other hand are inelastic processes and result from the interaction of the ions with lattice electrons of the sample. The electrons are excited to higher atomic states or they are removed from their nuclei and cause ionization. These unbound electrons can leave the surface and can be

[15] Gallium is used mainly due to its low melting point (+29.8 °C) and low volatility. To maintain its liquid state during operation, no additional heating is required. Low vapor pressure allows to use Ga in its pure form [Yao, 2007].

[16] For electrons that interact with a solid, primary electrons can be directly scattered back to the detector, leading to another 0.3 – 0.75 electrons on average that can be used for imaging.

Table 3.1: Comparison of particle-matter interaction parameters for electrons and ions. Values extracted from [Yao, 2007].

	Ga^+ Ion	**Electron**	**Ratio**
Elementary Charge	+1	-1	
Mass	$1.2 \cdot 10^{-25}$ kg	$9.1 \cdot 10^{-31}$ kg	130000
Velocity at 30 kV	$2.8 \cdot 10^{5}$ m s^{-1}	$1 \cdot 10^{8}$ m s^{-1}	0.0028
Momentum at 30 kV	$3.4 \cdot 10^{-20}$ kg m s^{-1}	$9.1 \cdot 10^{-23}$ kg m s^{-1}	370
Penetration Depth in Fe at 30 kV	20 nm	1800 nm	0.11
Average Signal per 100 Particles at 20 kV			
Secondary Electrons	100–200	50–75	1.3–4.0
Backscattered Electrons	0	30–50	0
Substrate Atoms	500	0	∞
Secondary Ions	30	0	∞
X-ray Photons	0	0.7	0

used for imaging. At higher energies than used in FIB processes, this energy loss mechanism dominates the total energy loss of the ion and thus the interaction [Orloff et al., 2003].

To locally change the topography of a sample, a sputtering process can be induced. This form of nuclear energy loss occurs if an ion hits lattice atoms of the sample. As result, a cascade of collisions is started by transferring momentum to the atoms of the sample. Atoms or ions can be ejected if the direction of momentum is rotated at least 90° from the incident angle and if the material-dependent surface binding energy of atoms at the surface is exceeded [Giannuzzi et al., 2005]. Every collision of the ion with an atom of the sample decreases the kinetic energy of the ion. Ultimately, the ion is stopped and implanted into the target material, as it cannot overcome the surface binding energy any more. Figure 3.3 depicts the interaction paths of an ion and the resulting processes.

The sputter yield Y, i.e. the number of ejected target atoms per incident ion is an important parameter for FIB-based processes. Especially for ion beam lithography, where a two-dimensional pattern shall be transferred to a suitable structure by area-selective exposure to fast ions. The sputter yield defines the basic dose necessary for a certain change in topography and thus the overall structuring time. *Sigmund* developed a model of »linear collision cascades«, which quantitatively describes the sputter yield as the number of ejected atoms per incident ion [Sigmund, 1981]. Due to the short range of the interactions, only

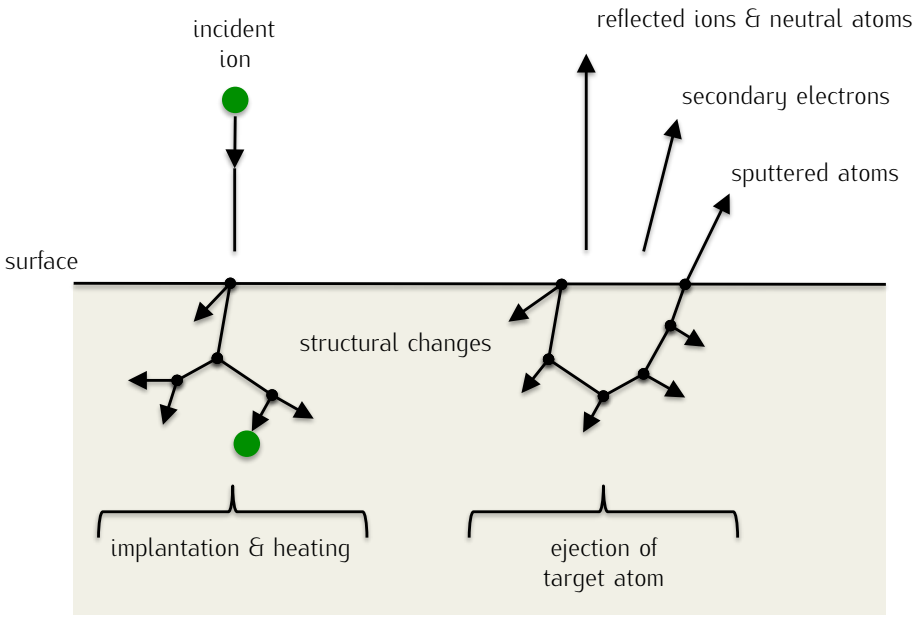

Figure 3.3: Schematic drawing of ion-solid interactions. The incident ion starts a cascade of collisions that is terminated by the ejection of one or more target atoms, by heating up the target or a combination of both. Furthermore, secondary electrons or the incident ion can be ejected. Scheme adapted from [Chapman, 1980].

nearest neighbors have to be taken into account. Additionally, the trajectories between the collisions are approximated as straight lines. This binary collision model involves the energy loss of the incident ion as a parameter, mainly dependent on its energy E_0, and the mass ratio of the involved particles M_I and M_T. One can classify the collision cascade into three regimes. (a) The »single knock-on regime« describes the interaction at low energies of $E_0 \approx 1\,\text{eV} - 1\,\text{keV}$ or if $M_I \ll M_T$, i.e. the incident ion is much lighter than an average target atom in terms of atomic weight. In this regime, the energy transfer is not sufficiently high to eject atoms from the surface and to start a collision cascade. (b) The intermediate, linear cascade regime describes the interactions observed in FIB milling for most cases very well. For energies $E_0 \approx 1\,\text{eV} - 1\,\text{MeV}$ and mass ratios of $M_I/M_T \approx 1$, a collision cascade involving approximately 1000 atoms is induced and sputtering occurs. The remaining energy that is not part of the collision cascade is transferred to the electrons of the target material and heats it up to higher temperatures. (c) The third regime includes cases for which $M_I \gg M_2$ or E_0 is large and is rarely reached in FIB-induced sputtering [Kaulich, 1996, Giannuzzi et al., 2005, Chapman, 1980].

The *Sigmund* model uses conservation of momentum and energy in elastic collisions as starting point for a quantitative approximation of the sputter yield. The model is derived

from transport theory and assumes that the target is smooth and amorphous [Sigmund, 1969, Orloff et al., 2003]. For ions impinging on the surface perpendicularly the sputter yield Y at a primary ion energy of E_0 is given by:

$$Y(E_0) = \frac{4.2 \cdot 10^{14}\, \alpha\, S_n}{U_s} \tag{3.1}$$

For the type of ions used in FIB systems, the dimensionless factor α can be approximated to $\alpha = 0.15 + 0.13 \cdot M_T/M_I$. U_s is the surface potential and S_n is the nuclear stopping cross-section, a value defined by the ratios of particle masses and atomic numbers [Orloff et al., 2003].

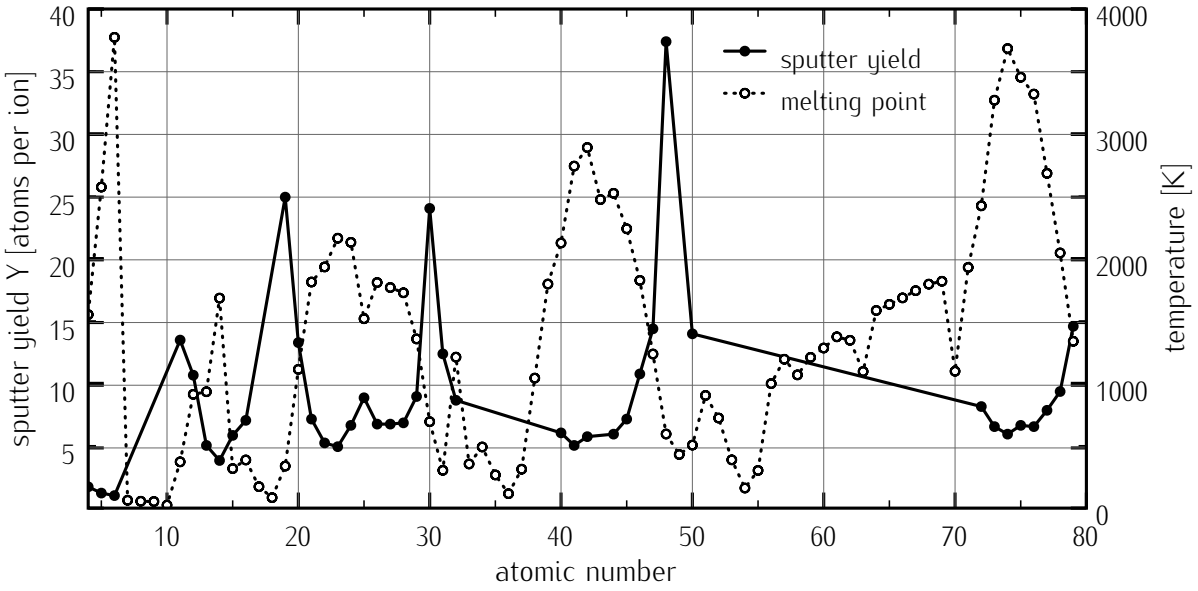

Figure 3.4: Sputter yield values calculated with linear collision cascade model and melting temperatures for elements with atomic numbers from 1 to 79. Values extracted from [Orloff et al., 2003, Giannuzzi et al., 2005].

Figure 3.4 shows calculated sputter yield values for 30 keV gallium ions for substrate elements in a range from $Z = 4$ to 97. Additionally, the melting temperatures of the elements are plotted to show their inverse correlation behavior. Note that the model does not describe the redeposition of atoms near the sputtering site. This effect occurs when milling e.g. small and deep trenches. Here, sputtered atoms condensate on the sidewalls and have to be sputtered several times until they are finally removed from the sample. A more detailed description is given below. The dependence of the sputter yield on atomic crystal structures

is also not covered by the model. The traveling range of ions in matter depends on the orientation of the crystal planes and thus on the depth in which energy is transported by the ion. This leads to a change in sputter yield and is referred to as »ion channeling«.

Redeposition is an effect that has to be taken into account for milling small features. It has been found that the majority of sputtered target atoms is in gas phase and thus is able to leave the milling site. As these atoms are not in thermal equilibrium, a fraction of these atoms condenses near or on the sputtering site. Such redeposited atoms have to be sputtered again, which lowers the theoretical sputter yield [Tseng, 2007]. Especially when milling narrow and deep trenches, where sputtered atoms at the bottom of the trench have to leave the milling site through a »channel«, the probability of condensation on the sidewalls of the trench increases. This leads to the characteristic V-shaped structure whereas the intended shape of a trench would have a rectangular cross section. The kinetic energy of the sputtered atoms, the sticking coefficient, as well as the sputter yield of the material, and the geometry of the milled features are parameters that influence the shape and strength of this effect [Giannuzzi et al., 2005].

3.2.2 Zeiss 1540XB FIB System

The *Zeiss 1540XB* FIB system is a focused ion beam microscope equipped with a field emission electron emitter and a gallium source. The electron column of type *Gemini* is the primary column and thus pointing 90° to the laboratory floor. It is used for scanning electron microscopy (SEM) and has magnetic lenses that focus the electron beam to diameters of 1 nm at 20 keV electron energy. Magnifications can be set from values of 20-fold up to 900k-fold at beam currents of 4 pA to 20 nA. Acceleration voltage can be adjusted from 100 V to 30 kV. The microscope is equipped with an annular-type *in-lens* detector and an *Everhart-Thornley* detector for secondary electron detection. The *Canion* gallium column is manufactured by *Orsay Physics* and points 54°, measured from the path of the electron beam. The coincident point of both beams is located $\approx$ 5 mm below the last lens element of the electron column. To assure normal incidence of the gallium ions, the specimen stage has to be tilted by 54° [Carl Zeiss Microscopy GmbH, 2003].

Under ideal imaging conditions, the ion beam can be focused to a spot of 7 nm diameter at 30 kV acceleration voltage. Focusing is here achieved by electrostatic lenses, as the power of magnetic lenses would not be sufficiently high to deflect the ions [Volkert et al., 2007]. The ion beam current can be adjusted from minimum values of 1 pA up to maximum val-

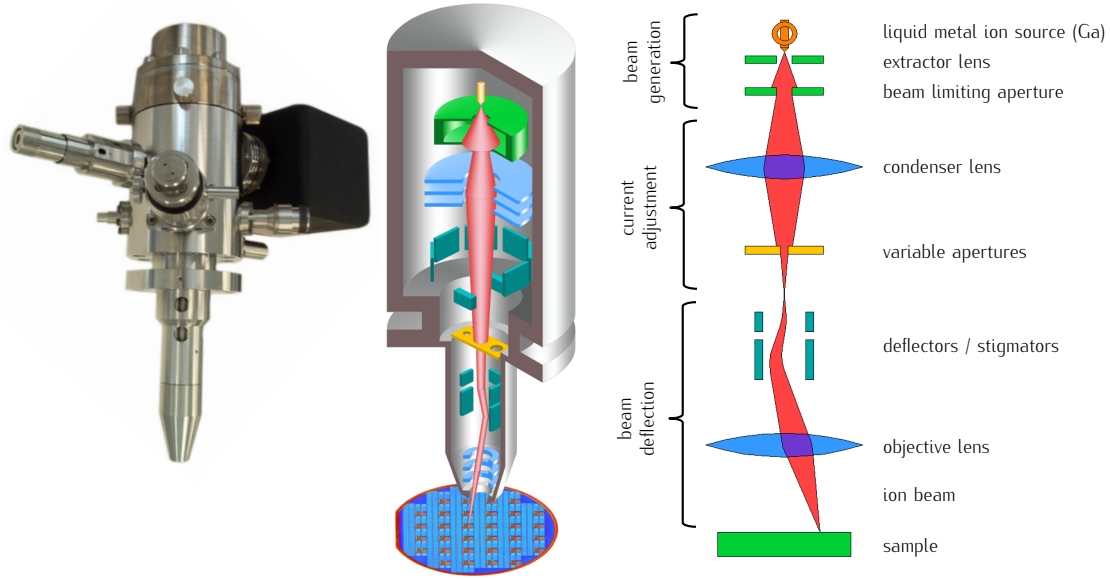

Figure 3.5: Photo, illustration and schematic beam path of the *Canion* gallium ion column. Images adapted from [Carl Zeiss Microscopy, 2008].

ues of 50 nA. Imaging magnifications can be set from 600-fold to 500k-fold. As illustrated in figure 3.2, the specimens are placed on a motorized six-axis stage in vacuum [Carl Zeiss Microscopy GmbH, 2003].

Figure 3.5 shows a photograph and sketches of the *Canion* ion column. The ion beam is extracted from a liquid metal ion source (LMIS), which consists of a tungsten needle that is connected to a gallium reservoir[17] and an extractor lens[18]. The tungsten needle is constantly wetted by a thin layer of gallium. A so called *Taylor*-cone is formed by the interaction of the applied electric field and the surface tension of the liquid, leading to a thin »incipient jet« and field-evaporation of ions.

The emitted ion current is regulated by a suppressor lens capable of delivering up to -2 kV. Typical emission currents are in the range of 1 to 3 µA. Changing the voltages of suppressor and extractor can cause a spatial displacement of the *Taylor*-cone and thus to a beam position displacement on the specimen surface. This has to be avoided during zone plate fabrication as it distorts the milled pattern [Yao, 2007]. By the described means, the ion beam is formed and accelerated to 30 keV. It passes the condenser system before motorized

[17] The gallium reservoir is designed to deliver stable emission for at least 750 hours at 2 µA extraction current.
[18] By the extractor lens high voltage of -5 to -8 kV is applied relative to the tungsten needle, leading to an electric field of magnitude $10^{10}\,\mathrm{Vm}^{-1}$ [Volkert et al., 2007].

apertures[19] define the beam current and the beam size. Typical ion beam currents are in the range of 1 to 5 pA for the fabrication of structures smaller than 100 nm and 500 pA to 10 nA for milling large cross-sections (10 µm and above).

Further down the column, the stigmator system corrects for non-ideal roundness of the beam before the electrostatic deflection system moves the beam over a desired field of view and the objective lens focuses the beam on the surface of the specimen. The accuracy with which the scanning of the beam occurs depends on the number of voltage steps the scan generator delivers to the deflection system. Typical non-lithographic FIB systems are capable of addressing a 10 bit field, i.e. 1024 pixels each in X and in Y direction. This is enough for TEM lamellae preparation or cross section milling. For milling circular structures as it is necessary for zone plates this is not sufficient as the limited number of pixels leads to aliasing effects. For this reason a lithography attachment of type *Raith Elphy Plus* is installed. After basic properties of the beam have been adjusted, the lithography attachment takes control of the deflection system and acts as an external scan generator. It has DACs[20] with 16 bit resolution and offers a software suite to design and mill circular structures. By this, a field of 65536 x 65536 pixels can be addressed, which is sufficient for most lithographic applications.

3.2.3 Raith ionLiNE IBL System

The second type of FIB system that was used for the work described herein is the *Raith ionLiNE* microscope. It is an FIB system that was, in contrast to all other commercially available systems, developed as a dedicated tool for lithography. The *ionLiNE* system is not equipped with SEM functionality and thus not capable of cutting TEM lamellae, which is one of the key features of classical FIB systems. In contrast to these classical systems, the ion column is mounted vertically, i.e. is the primary column. As an outcome of the European Nano-FIB program, the system is equipped with an extremely stable LMIS, optimized for high resolution at low beam currents, and a stage controlled by a laser-based *Michelson*-interferometer [Nano-FIB, 2002]. By using an emitter geometry that holds more liquid gallium at the tip, it shows higher stability and less sensitivity to contamination and back-sputtering compared to conventional sources. Due to this and other design differences, there is no need for heating the emitter to maintain constant emission [Gierak et al., 2005]. This provides more stability, which is important for long-term FIB milling tasks as it is e.g.

[19] Aperture diameters from 10 to 400 µm.
[20] Digital to analog converter.

necessary for the fabrication of zone plates. Additionally, the source geometry allows higher values for the on-axis angular beam intensity, a parameter that influences the beam current. The source can therefore be operated at higher extraction voltages of $\approx 15\,\mathrm{kV}$, compared to values of $<8\,\mathrm{kV}$ for conventional gallium emitters and higher ion beam currents at the same probe diameter. The electrostatic optical elements in the column are optimized for highest patterning resolution and minimum beam tails, as for most lithographic applications small probe diameters are more important than high ion beam currents for massive ablation of matter [Gierak et al., 2009]. As the ion column is mounted vertically, the stage has not to be tilted to values of $\approx 50°$ as it is common for microscopes with two columns. Generally, the motorized sample stages can be constructed more stable in such a non-tilted arrangement. As an example, *Gierak et al.* have shown that the column is capable of drilling sub-5 nm holes in silicon carbide membranes [Gierak et al., 2007].

3.3 Laser-Induced Plasma Sources

As beam time at synchrotron radiation facilities is scarce, alternative light sources have emerged. One way to excite X-ray and EUV emission is using a high-power laser that is focused on a solid, liquid or gaseous target. In this thesis, a liquid ethanol jet is used as target material to excite electronic transitions of carbon and oxygen in the SXR and EUV spectrum (see figure 3.6 for a scheme of the light source.). A pulsed laser is focused on the jet to ignite a plasma emitting in $4\,\pi\,\mathrm{sr}$.

The design of the laboratory source is based on work of *Vogt et al.* at Remagen, Göttingen and Berlin university [Vogt, 1999, Vogt, 2002]. A *Coherent Infinity* laser system is used as plasma heating device. It is based on neodymium as laser-active material and delivers pulse energies up to 400 mJ at 100 Hz repetition rate in the infrared spectral band ($\lambda = 1064\,\mathrm{nm}$). This corresponds to a maximum average power of 40 W. A technical overview of the laser system is depicted in figure 3.7. A neodymium-doped yttrium aluminium garnet crystal is pumped by a laser diode in cw-mode[21]. An acousto-optic modulator within the resonator cavity leads to pulsed infrared laser light as output of the oscillator. Pulse energies of 30 µJ at $\lambda = 1064\,\mathrm{nm}$ are reached at 8 to 10 ns pulse duration. The infrared laser pulses pass an amplifier arrangement based on two flash lamp-pumped Nd:YAG rods and an SBS[22] cell acting as phase conjugate mirror. This arrangement shortens the pulse to lengths of $\tau \approx 3\,\mathrm{ns}$ at IR pulse energies of 50 to 400 mJ. To obtain $\lambda = 532\,\mathrm{nm}$, second harmonic generation with

[21] cw: continuous wave
[22] SBS: »Stimulated Brillouin Scattering«

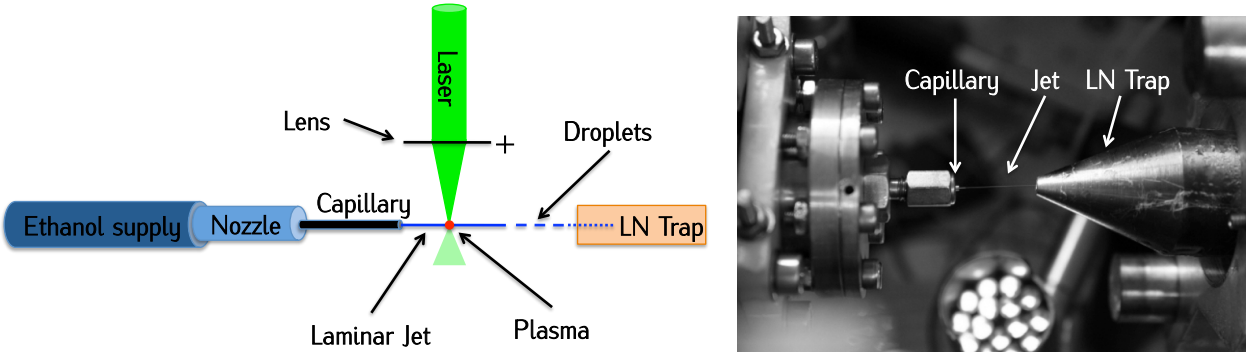

Figure 3.6: Scheme of ethanol jet-based plasma source and photograph of the glass nozzle, mounted in a special clamping holder, and the cone which leads to the liquid nitrogen trap. Ethanol is filtered and fed into a tapered capillary with 20 µm end diameter. By pressures of $P > 5$ bar, a laminar jet is formed that decays to droplets within some mm of flight path in vacuum. A frequency-doubled Nd:YAG laser is focused onto the laminar region of the jet and a plasma is formed. X-ray emission has to be spectrally separated from the visible part of the emission spectrum.

efficiencies larger than 50% is achieved by passing a BBO[23] crystal. Dichroic mirrors are used to separate the infrared from the green laser light before only the green light is directed to the plasma chamber [Coherent Inc., 1998].

The green laser beam is then focused by a f = 50 mm lens onto the ethanol jet inside a vacuum chamber, pumped by a 60 m^3h^{-1} backing pump and a 880 ls^{-1} turbo-molecular pump. The diameter of the focal spot produced by the lens is smaller than 20 µm and therefore produces intensities of approximately 10^{14} W cm^{-2} [Vogt et al., 2004]. The ethanol is ejected from a glass capillary of 20 µm diameter which is pressurized to 5 to 50 bar applied by a nitrogen gas bottle. A 0.5 µm filter is installed to prevent blocking of the capillary by dust particles. The ethanol is collected by a separately pumped trap which is cooled by liquid nitrogen to freeze out the majority of ethanol.

The diameter of the plasma was measured to 27 µm for soft X-ray emission [Vogt et al., 2004]. Emission live monitoring and optimization is performed by a Ti-foil-protected photodiode. The motorized jet and lens mounts are adjusted to ideal overlap of laser focus and jet by the diode signal. As the plasma cracks the molecular bonds of ethanol, »debris« is emitted, mainly consisting of carbon. Thus, all surrounding elements are coated with carbon during plasma operation. Additionally, free oxygen radicals oxidize mechanical components and optical elements. To avoid their degradation by debris, sensitive equipment like multilayer

[23] BBO: barium borate

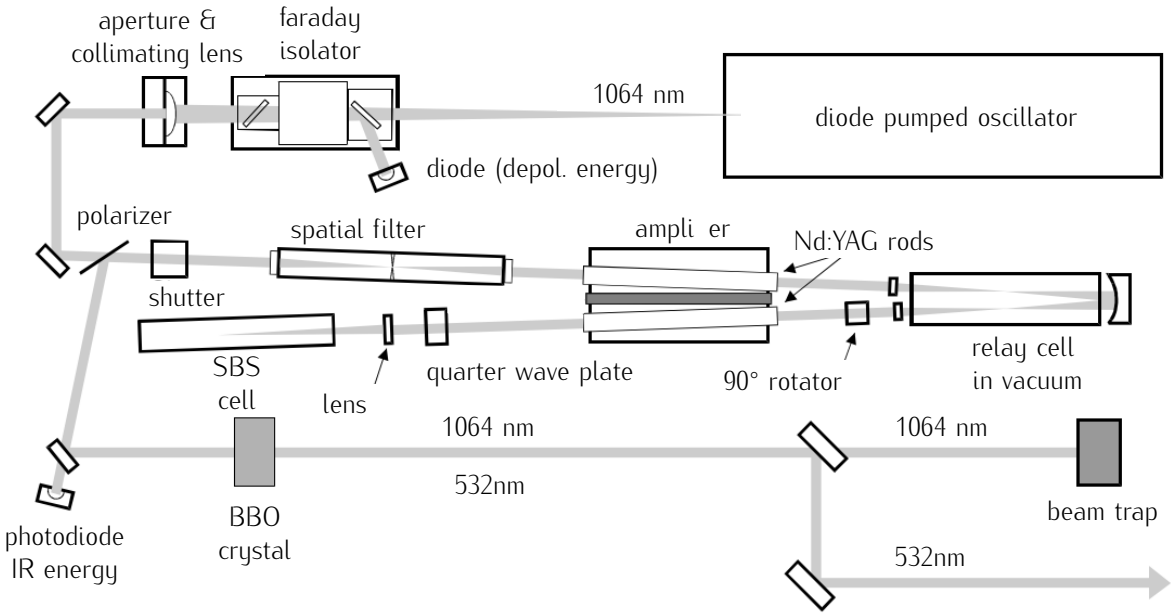

Figure 3.7: Technical overview of the *Coherent Infinity* laser system. A laser-diode pumped oscillator emits infrared pulses at $\lambda = 1064\,\text{nm}$ wavelength. A *Faraday*-isolator is mounted to prevent back-reflected light to damage the oscillator. Amplification of the oscillator pulses is performed by two flash lamp-pumped Nd:YAG rods. A reflection by 180° is done by stimulated *Brillouin* scattering (SBS) in a cell filled with CFC 113 (Trichlorotrifluoroethane), acting as phase conjugate mirror that shortens the pulses to approximately 3 ns. After passing the YAG crystals a second time, a spatial filter removes high-frequency noise from the beam before second harmonic generation is excited in a BBO crystal [Coherent Inc., 1998, Vogt, 1999].

mirrors and zone plates are mounted in a second vacuum chamber, separated by X-ray transparent filter foils. The filter foils also act as vacuum seal as the pressure in the plasma chamber drops to values of 10^{-4} to 10^{-3} mbar during plasma operation. By that, high vacuum and clean conditions are preserved in the second vacuum chamber.

4 Fabrication of Linear Diffraction Gratings

The suitability of ion-beam lithography as a tool for the fabrication of diffractive elements for X-ray and EUV applications was investigated by the author in previous experiments, described in [Lenz, 2009] and [Lenz et al., 2009]. Basic patterning strategies were developed and first successful X-ray optical experiments were performed using IBL-fabricated structures. In these experiments, diffraction gratings were milled on metal-coated silicon wafers,

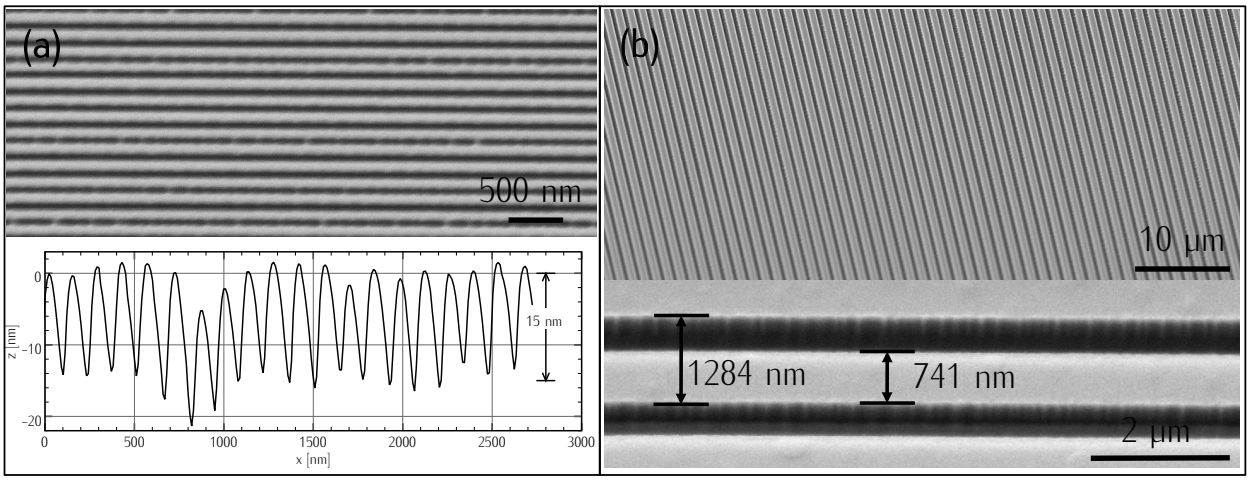

Figure 4.1: (a): SEM-images showing an IBL-fabricated reflection grating (g = 140 nm, 153 periods) and the corresponding atomic force microscopy profile. Fabrication parameters: 10 pA ion beam current. 60 s dwell time per 20 µm line. (b): SEM-images showing an IBL-fabricated reflection grating (g = 1284 nm, 256 periods), milled in a 15 nm Mo-coated Si-substrate. Fabrication parameters: 500 pA ion beam current. 60 s dwell time per 20 µm line.

as well as on silicon nitride membranes. All gratings were fabricated without the use of a 16 bit pattern generator and without dedicated lithographic software, so the grating patterns were limited to designs smaller than 1024 × 1024 pixels and no drift correction could be used during milling. Reflection gratings with grating constants of g = 140 nm and g = 1.3 µm were milled into Cr- and Mo-coated Si-samples, respectively (see figure 4.1). Freestanding silicon nitride gratings (Au-coated, g = 363 nm) were fabricated and successfully applied as central elements in a slit-grating-spectrograph to investigate the spectral emission of an

ethanol laser plasma. Figure 2.7 on page 19 shows one of the transmission gratings that were used for the experiments. Especially for optical elements with freestanding diffractive structures, the ion beam-based process showed advantages compared to EBL-based approaches as the structures are directly milled to the membrane without the need for pattern transfer steps. As result of these experiments, the fabrication of *Fresnel* zone plates by IBL was identified as next target.

5 Results

This chapter covers the fabrication of *Fresnel* zone plates by ion beam lithography and their application as lenses in full field X-ray and EUV microscopes. Microscopic imaging is a suitable way to judge the quality of lenses in terms of resolution and efficiency. The fabricated zone plates were therefore applied as objective lenses in two microscopy setups, for the two FIB systems used. The *Zeiss XB1540 Crossbeam* system is a standard FIB machine with an external lithography attachment. As a non-lithographic microscope with an additional SEM column, it fulfills a broad range of tasks in the electron microscopy laboratory. The *Raith ionLiNE* FIB system on the other hand is a dedicated IBL writer, optimized for lithographical tasks.

As access to synchrotron facilities is limited, an EUV microscope was constructed as testing environment for the zone plates that were fabricated with the *Zeiss XB1540 Crossbeam* system. Higher imaging resolutions due to smaller zone structures were expected from the zone plates fabricated with the *Raith ionLiNE* FIB instrument. Therefor a mobile optical framework for X-ray optical experiments was used at a synchrotron light source. The framework is equipped with piezo-driven stages and allows fast construction of different experimental setups like the described X-ray microscope.

5.1 Zone Plate Fabrication Zeiss XB1540

The first set of zone plates was patterned with a *Zeiss XB1540 Crossbeam* FIB system and a *Raith Elphy Plus* pattern generator. The external pattern generator was used because it expands the number of addressable pixels within the write field by a factor of 4000 compared to the internal scan generator of the microscope. The ion column of the microscope was set to 30 kV acceleration voltage for all the experiments. It is optimized to this value for standard milling tasks. If the ion column could be operated at higher acceleration voltages, it would increase sputter yields due to higher momentum of the particles. Lower voltages can be applied and are used for large-area polishing tasks as the penetration length of the ions decreases and ion-induced structure damage in e.g. crystalline samples is reduced to smaller volumes. To choose a suitable zone plate design in terms of achievable outermost

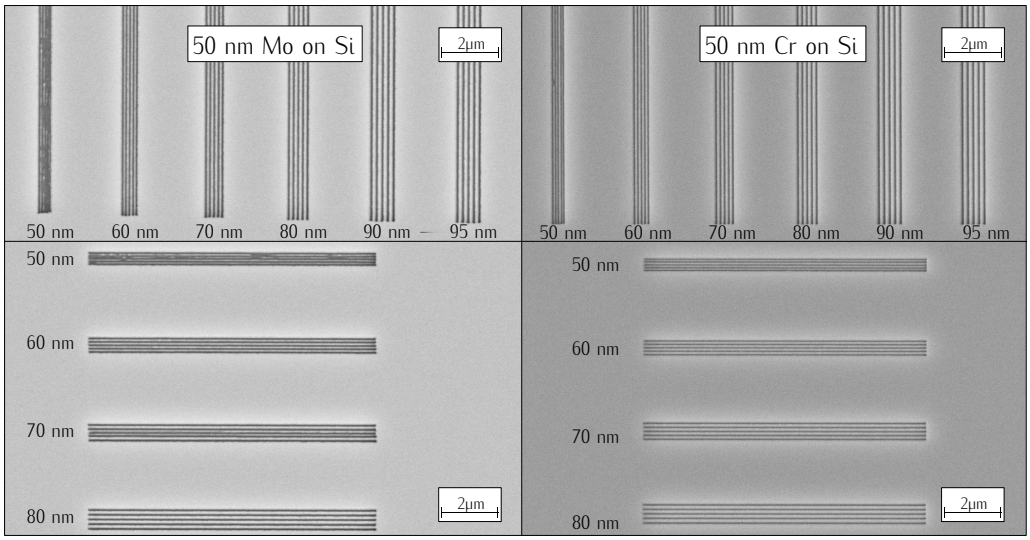

Figure 5.1: SEM micrograph of 50 nm Cr- and 60 nm Mo-coated silicon wafers used for the resolution test pattern. Structure sizes of 95 nm to 50 nm in horizontal and vertical orientation were milled to judge the achievable resolution in patterning thin metal films. Area dwell time: 15 ms. Probe current: 10 pA. [Lenz et al., 2011]

zone widths, the maximum patterning resolution for FIB milling of typical zone plate materials was investigated first. Periodic lines were milled in substrates, consisting of chromium and molybdenum-coated silicon wafers with an ion beam current of 10 pA. Coating thicknesses of 50 nm (Cr) and 60 nm (Mo) were used, as this marks the minimum layer thickness for acceptable diffraction efficiencies. The small beam current and the relatively thin metal layer allow the smallest patterning structures for the *Zeiss* FIB system during milling of periodic structures [Lenz et al., 2011].

Figure 5.1 shows grating structures with descending structure sizes (half-pitch) from 95 to 50 nm. Ion dose values of 37.5 mC/cm^2 were applied to remove the metal layers down to the silicon substrate. For both materials, 60 nm lines are clearly resolved whereas pattern degradation is observed at 50 nm. These structures tend to collapse, so that no defined diffraction is expected. No dependence on the milling direction is found. As these straight lines only indicate the potential of milling thin metal films, achievable values for zone plate structuring are expected to be above 60 nm, due to drift during milling, the curved structures and because functioning zone plates have to be mounted on thin X-ray-transparent membranes. Precise dose control has to be ensured during the process to prevent milling through the membrane, which leads its destruction if mechanical stress has been induced during the metal deposition process.

5.1.1 Material Choice

As described in section 2.4.2, the diffraction efficiency of a zone plate at a specific wavelength depends on the properties of the used material. The complex index of refraction in combination with the used layer thickness influences the fraction of incoming light that is deflected into the desired order of diffraction. For completely absorbing zones and totally transparent grooves, values of $\eta_1 = 10\,\%$ can be achieved for the ideal case in the first order of diffraction (»absorption zone plate«). If the zone material does not absorb and the phase shift of a light wave is optimized to π in reference to a neighboring zone, $\eta_1 = 40\,\%$ can be reached. Under real conditions, the values are lower because the substrate is not completely transparent and because of irregularities of the zone plate pattern and the zone profile. Deviations of the ideal layer thickness of the zone material also lead to efficiencies below the optimum. For the last decades, gold has been one of the most widely used zone plate materials. It

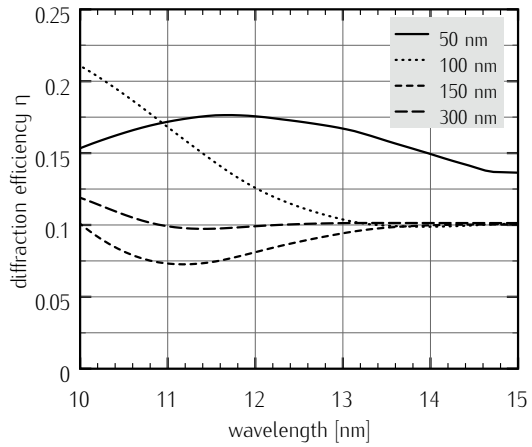

Figure 5.2: Simulated diffraction efficiencies for AuPd layers of different thicknesses for wavelengths between $\lambda = 10$ and 15 nm. For $\lambda = 13$ nm, the transition of a phase zone plate ($\eta > 0.1$) to an absorption zone plate ($\eta \approx 0.1$) can be observed for layer thicknesses above 100 nm. Database values from [Henke et al., 1993].

is available in most laboratories and shows excellent diffraction properties for soft and hard X-rays. For the zone plates fabricated by the *Zeiss XB1540* FIB system, a mixture of gold and palladium (AuPd, 80 % / 20 %) was chosen as zone material. Blending of palladium into gold leads to smoother surfaces of the deposited layers compared to pure gold. The tendency to form isolated islands during the deposition process is reduced. An advantage of the sputtering processes is, that the composition of the sputtered layer is identical to the composition of the target [Bunshah, 1994]. So, the 80/20 ratio of gold and palladium is preserved.

Figure 5.2 shows calculated first order diffraction efficiencies for AuPd layers from 50 to 300 nm thickness. For $\lambda = 13$ nm, coating thicknesses larger than 100 nm lead to $\eta = 10\,\%$

efficiency as the layers are completely opaque. At the same time, the demands to the nanofabrication process increase with the ratio of layer thickness to structure size (»aspect ratio«). Below 100 nm, phase zone plate characteristics are observed, leading to higher efficiencies. For the experiments described herein, both cases were addressed, i.e. zone plates with zone heights lower than 100 nm were fabricated along with heights of approximately 300 nm.

Figure 5.3 shows cross sections of AuPd layers, deposited with different coating parameters by magnetron sputtering with the described sputter coater. The goal was to find parameters for which the layers are as flat as possible as this is important for further structuring by IBL. It is known that the sputter yield of 30 kV gallium ions is dependent on the angle of incidence [Orloff et al., 2003]. This holds true for the orientation of the whole sample to the incident beam, but also for local deviations from the 90° incident angle, as it is the case for uneven spots due to sputter coating. As a result, these spots intensify during ion beam bombardment and lead to the formation of ripple-like structures. Additionally, different crystallographic orientations show different sputter yields, which implies that amorphous and even sample surfaces are the ideal starting point for IBL based zone plate fabrication, as uniform shape and depth of the structures are highly important for proper diffraction [Giannuzzi et al., 2005].

The growth and the microstructure of thin metal films mainly depend on the energy of the sputtered atom, the temperature as well as the surface conditions of the substrate. It can be classified to four cases. In figure 5.3e a schematic representation after [Thornton, 1974] is given: Adatoms[24] that condense at low temperatures show limited mobility. The film growth is determined by tapered crystallites originating from a limited number of nuclei. Longitudinal porosity is observed, as there is free space in between the crystallites. In figure 5.3e, this zone can be identified as ZONE I. For pure metals and single-phase alloys, a transition zone can be observed as the substrate temperature rises (ZONE T) and the mobility of the adatoms increases. Here, diffusion processes of the adatoms dominate as the energy of the adatoms can be high compared to the binding energy of an atom on the substrate. The zone is defined by weak grain boundaries and tightly packed fibrous grains. ZONE II is reached if the weak boundaries have been replaced by a fully dense columnar morphology. An approximation for the transition temperature T_1 between ZONE I and II for a metal with melting temperature T_m is $T_1 = 0.3 \ldots 0.5 \cdot T_m$. At higher substrate temperatures of $T_2 > 0.7 \cdot T_m$, ZONE III can be observed, which is determined by equiaxed grain morphology and a microstructure near to bulk metals [Bunshah, 1994].

[24] The target atoms that condense on the substrate are referred to as adatoms.

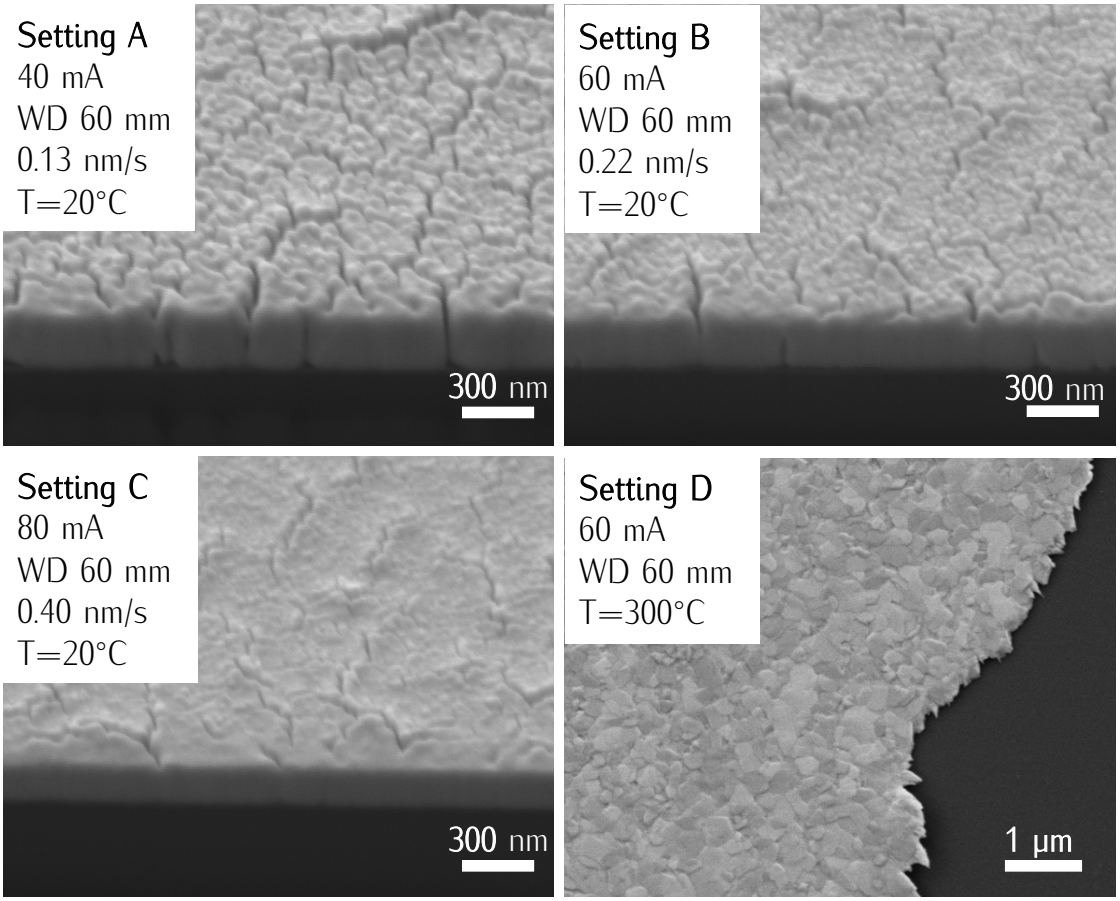

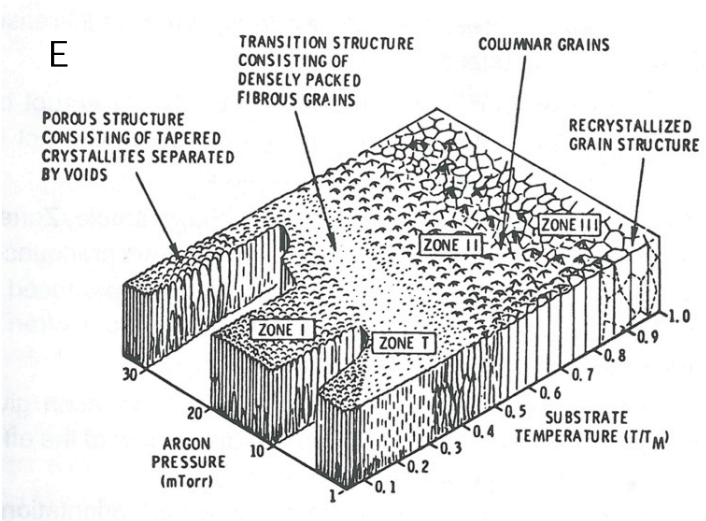

Figure 5.3: SEM images of cross sectioned AuPd layers on silicon wafers (A to D) and the zone model of condensed metal (E), developed by *Thornton* [Bunshah, 1994, Thornton, 1974]. Layers were deposited by magnetron sputter coating at $5{\cdot}10^{-2}$ mbar with different sputter currents (40 to 80 mA) and a working distance (WD) of 60 mm. Setting A shows the formation of tapered crystallites with high degree of porosity (ZONE I). Settings B and C with deposition rates between 0.22 and 0.40 nm/s show decreasing porosity and best surface characteristics (ZONE I with tendency to ZONE II). B and C were used for zone plate substrate fabrication. Setting D shows the formation of strong grain boundaries with large crystallites due to heating (ZONE III).

The coatings in figure 5.3 were deposited by sputtering with argon plasma at a pressure of $5{\cdot}10^{-2}$ mbar in a *Baltec MED-020* sputter coater (described in section 3.1). The series show SEM images of FIB cross-sections of layers, sputtered at a working distance of 60 mm with sputter currents of 40 to 80 mA, corresponding to deposition rates of 0.13 to 0.40 nm/s. The substrate was kept at room temperature for settings A, B and C. Setting A shows high degree of porosity with open pores up to 20 nm (ZONE I). Settings B and C show lower porosity and smoother surfaces and were therefore chosen as best candidates for zone plate layers (ZONE I–II). In comparison to setting A, less layer cracks and island formation is observed. Setting D, for which the substrate was heated to T = 300°C, shows ZONE III behavior according to the structural zone model of *Thornton* as described in [Bunshah, 1994]. At higher temperatures, recrystallized grain structure occurs with grain sizes of several hundred nanometers. This is especially problematic for zone plate fabrication by IBL because of the ion channeling effect.

5.1.2 Drift Correction Strategy

Drift correction is a crucial part of IBL-based fabrication of zone plates. In EBL-based processes, where exposure times are in the range of minutes, pattern distortion due to drift of the electron beam relative to the sample is not considered problematic for most applications. For IBL-based processes, this is different. Typical exposure times are much longer here, which requires to keep the system stable during exposure. Changes of the ion beam position on the sample due to instabilities of the ion source during milling of periodic structures will lead to local deviations from the ideal grating constant and thus to decreasing diffraction efficiency and resolution. This is different from other FIB applications. For example in TEM lamellae preparation, where fabrication times are one to several hours, drift of the ion beam position relative to the sample also occurs. However, it is not considered as a problem because it would only result in a thickness deviation of the pre-cut lamella. If this drift does not exceed critical values, it can easily be compensated during the further steps.

Compared to TEM specimen preparation, ion beam lithography shows two major differences: (a) Beam deflection for standard FIB microscopes is typically restricted to an array of up to 2000 × 2000 pixels. To exactly write circular shapes, special lithographic attachments are necessary to address a 16 bit write field (65535 × 65535 pixels). As described, a *Raith Elphy Plus* pattern generator is used for this purpose. (b) For the fabrication of zone plates, the zone placement accuracy is of extreme importance. Typical IBL zone plate exposure

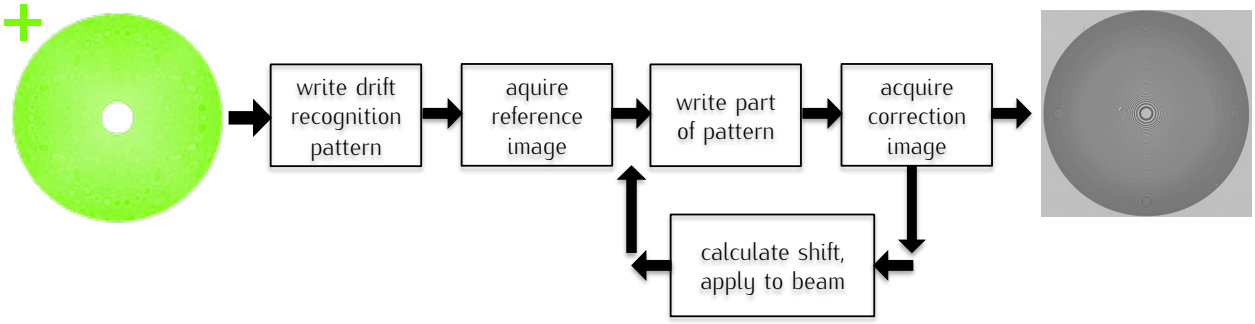

Figure 5.4: Schematic overview of the zone plate fabrication process from design to functioning lens.

times are in the range of hours during which drift effects should not exceed one third of the outermost zone width of the zone plate to ensure proper diffraction. Therefore, long-term stability of the FIB system is crucial.

One source of instabilities is the drift of the motorized stage. Due to temperature differences of the sample holder and the motorized stage, settling times have to be taken into account. The stage in the *XB1540* system is not controlled by a feedback loop of encoders, so these drifts cannot be measured by the microscope itself. This is also true for drift originating from slipping motor bearings. The second principal source of drift is the gallium ion emitter. The ion emission from the liquid metal source is regulated to 2.0 µA by a suppressor lens which can be excited from 0 to 2000 V. Fast changes of this voltage lead to beam shifts and focus changes on the sample plane, and therefore to pattern degradation. Fast suppressor adaptions are necessary if the emission characteristics of the ion source change during operation. This can be caused by e.g. adsorption of ambient elements in the vacuum system [Orloff et al., 2003] or if no constant flow of gallium is present at the tip of the ion source. Typically, the time span from switching on the source to stable ion emission is in the range of 30 min to 2 h, depending on the condition of the source and its lifetime ($<$ 2000 µAh). Regular heating cycles are important to get rid of the contamination on the liquid metal ion source, to maintain stable emission and extend the lifetime of the source.

Experiments showed that the ion source as well as the motorized stage have to be considered as sources of drift, which makes the strategy to use only SEM imaging for drift correction unfeasible [Lenz, 2009]. This was circumvented by suitable drift correction strategies based on the acquisition of ion-induced secondary-electron images of marks on the sample surface. These images were compared to a reference via a cross-correlation algorithm, provided by the used lithographic software suite [Overbuschmann et al., 2012].

Figure 5.4 shows the drift correction strategy that was developed for the fabrication of zone plates by IBL. As first step, zone radii are calculated and transferred to *GDS II* format by a

script, written in *Matlab*. This zone plate design is the basis of the process. A suitable drift correction mark is milled into the substrate as a reference. Usually, the zone plate is placed on a metal-coated silicon nitride membrane (100 nm thickness). The drift mark is milled by the ion beam as first pattern on the substrate. For the fabrication of this mark, the metal layer is selectively removed down to the silicon nitride but without inducing damage to the membrane by milling to deep. If there is residual stress in the membrane or the metal layer, this immediately leads to the destruction of the membrane. During the next step, this drift recognition pattern is imaged by ion-induced secondary-electron imaging and stored as the reference image. By this, the origin of the drift-correction coordinate system is defined. Note that every image acquisition leads to the removal of a thin metal layer and therefore degradation of the drift mark.

Subsequently, a fraction of the zone plate pattern is milled into the sample before a second image of the drift mark is acquired. In the meantime, the position of the ion beam relative to the surface of the substrate has changed due to drift of the beam and/or the stage. The two acquired images (reference image and drift correction image) are now compared by cross-correlation to attain a shift value, which is inverted and applied to the beam to recover the original beam-to-sample position. If a laser interferometer-controlled stage would be installed in the microscope, the shift values could be corrected by a movement of the stage. However, the motorized stage of the *XB1540* microscope is not accurate enough for this kind of correction. So, the beam shift values are applied to the ion beam via the electrostatic deflection system, before the next fraction of the zone plate pattern is milled. These steps are repeated until the zone plate pattern is completed.

Fractioning of the zone plate into smaller bits that can be exposed during two drift correction steps can be done by two writing strategies: (a) To scan the desired pattern for a fraction of the total exposure time and to perform a drift correction after every fraction. This is repeated until the desired pattern depth is reached. (b) To mill zones subsequently to each other and to perform drift correction after every zone. Whether (a) or (b) is used has to be decided for every combination of FIB system, zone plate dimensions and material.

5.1.3 Measurement of Drift Speed

The strength of drift and thus the influence on the patterning strategy strongly depends on the drift speed. To measure the drift of the microscope in relation to the settling time of the system after sample loading, the following procedure was applied (see figure 5.5): A

ring pattern of 5 µm diameter with a dot in the center was milled into the sample (duration approx. 11 min). Subsequently, to simulate ion beam- and charge-induced effects, a square pattern was raster-scanned for 63 min, before a second ring structure was fabricated. By this, the drift in x and y direction (s_x, s_y) during one hour could be measured by the deviation of the ring structure's centers from their ideal position relative to each other (see 5.5a). The drift speed during the exposure time could be calculated as the total exposure time $t_{tot} = 84.75$ min was known.

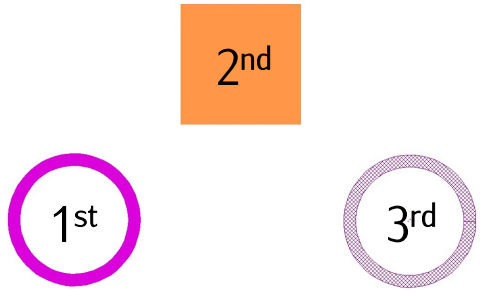

(a) Design of the pattern to measure drift in the FIB microscope.

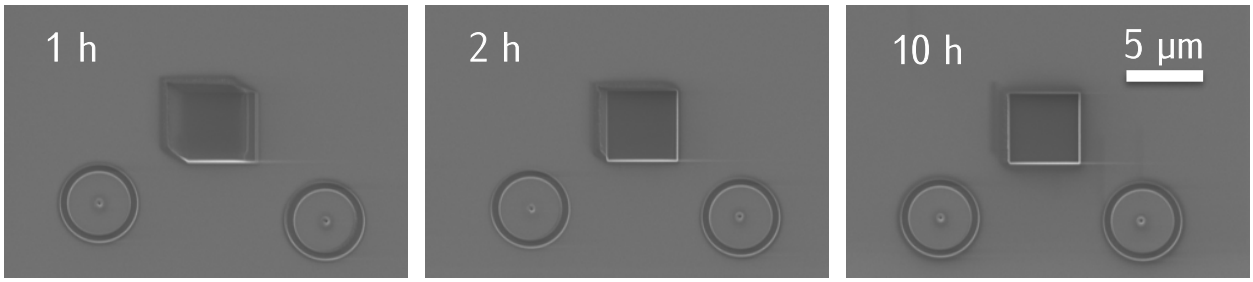

(b) Ion-induced secondary electron images of the drift measurement pattern after 1 h, 2 h and 10 h of settling time.

Figure 5.5: Measurement of absolute drift speed. The left ring of the pattern had been milled into the surface before the square was scanned for 1 h. During that period of time, drift occurred, which displaced the position of the second ring. The deviation from the ideal to the real position could be measured in images acquired afterwards.

The measurement was performed after 1, 2 and 10 h of settling time between loading the sample to the microscope and starting the exposure. For 1 h settling time, one can calculate the mean drift speed during exposure in x- and y-direction by:

$$\begin{pmatrix} v_x \\ v_y \end{pmatrix} = \frac{\vec{s}_{drift}}{t_{tot}} = \frac{1}{84.75\,\text{min}} \begin{pmatrix} 2230\,\text{nm} \\ 1270\,\text{nm} \end{pmatrix} = \begin{pmatrix} 26.31 \\ 14.98 \end{pmatrix} \frac{\text{nm}}{\text{min}} \tag{5.1}$$

Table 5.1 shows the results for 1, 2 and 10 h settling time. As expected, the drift speeds decreased with longer settling times, with a small residual drift for 10 h. Starting with a mean value of 20.6 nm/min one hour after loading the sample, 8.4 nm/min was reached after 2 hours. Best practice for lowest drift speeds is to load the zone plate sample in the evening, let the microscope settle over night and start the exposure in the next morning. By that, drift speeds of 3.1 nm/min can be reached. This directly lead to the first limit of outermost zone width for the *Zeiss* microscope. For a zone plate with an outermost zone width of approximately 100 nm, a drift budget of 0.3·100 nm can be consumed to preserve proper diffraction of the pattern. This is reached after 10 min time intervals between two drift correction steps. For typical patterning times of several hours, more than 100 drift correction steps are necessary to keep the zone plate patterning process sufficiently accurate.

Table 5.1: Measured drift of the Zeiss XB1540 FIB microscope after settling times of 1, 2 and 10 h.

Settling Time	s_x [µm]	s_y [µm]	v_x $[\frac{nm}{min}]$	v_y $[\frac{nm}{min}]$	v_{mean} $[\frac{nm}{min}]$
1 h	2.23	1.27	26.31	14.98	20.6
2 h	0.88	0.538	10.38	6.35	8.4
10 h	0.31	0.22	3.66	2.59	3.1

5.1.4 Drift Marks

Working with drift recognition marks in IBL is different compared to EBL-based processes. Every image scan of the mark degrades the pattern and makes it more difficult for the algorithm to compare it to the reference image. Additionally, different mark geometries degrade differently when imaged, due to dynamic matter removal and redeposition effects. The ideal mark withstands more than 100 image scans during zone plate exposure and delivers stable and distinctive cross-correlation signals with clearly distinguishable peak values.

The first step of the evaluation process was to compare different mark patterns by their auto-correlation function. Calculating the auto-correlation function of a signal or an image provides information about the similarity of the signal or image with itself. By this, the

influence of e.g. side maxima in the resulting signal could be investigated without the influence of effects like noise in the images. These side maxima negatively affect the robustness of the drift correction algorithm during the actual drift correction process.

The one-dimensional cross-correlation of two signals f(x) and g(x) is given by

$$f(x) \otimes g(x) \equiv \int_{-\infty}^{+\infty} f^*(\tau) \cdot g(x+\tau)\,d\tau. \tag{5.2}$$

which becomes the auto-correlation if two identical input signals are assumed:

$$f(x) \otimes f(x) \equiv \int_{-\infty}^{+\infty} f^*(\tau) \cdot f(x+\tau)\,d\tau. \tag{5.3}$$

For numerical calculation of the auto- and cross-correlation functions of one or two images, the input signals (f(x), g(x)) can be transformed to *Fourier*-space (F(ω), G(ω)), where the operations can be carried out as multiplications:

$$f(x) \otimes g(x) \quad \circ\!\!-\!\!\bullet \quad F^*(\omega) \cdot G(\omega). \tag{5.4}$$

Figure 5.6 illustrates extracts of the investigated drift correction patterns and the corresponding results of the auto-correlation algorithm[25]. All patterns were chosen to be approximately 5 µm in diameter as they had to be placed within the same write field in which the zone plate pattern was placed. A too small pattern would degrade faster under influence of the ion beam so a 5 µm pattern with 15 µm drift image size is a good trade-off between size (15 % of the edge length of the write field), area (2.25 % of the total write field area) and stability. As the specimen stage in the microscope is not equipped with laser-interferometer controlled feedback, the pattern had to be placed within the $100 \times 100\,\mu m^2$ write field of the gallium ion beam as the stage could not be moved in any way during the exposure of a zone plate. Stitching errors of several micrometers would arise and make zone plate fabrication impossible. This also means that the drift correction mark had to be placed on the silicon nitride membrane and not on the much more stable silicon frame.

Investigated patterns were (a) a classical cross-mark, widely used in EBL-based processes, (b) a chessboard pattern, (c) a ring pattern, (d) two cross marks, 45° tilted with respect to each other, (e) a combination of ring and cross-mark pattern, (f) a pattern consisting of randomly arranged lines, (g) three triangles and (h) a pattern consisting of five horizontal lines. The patterns were supposed to show low side maxima in the auto-correlation signals

[25] Auto-correlation functions were numerically calculated by a script written in *Matlab*.

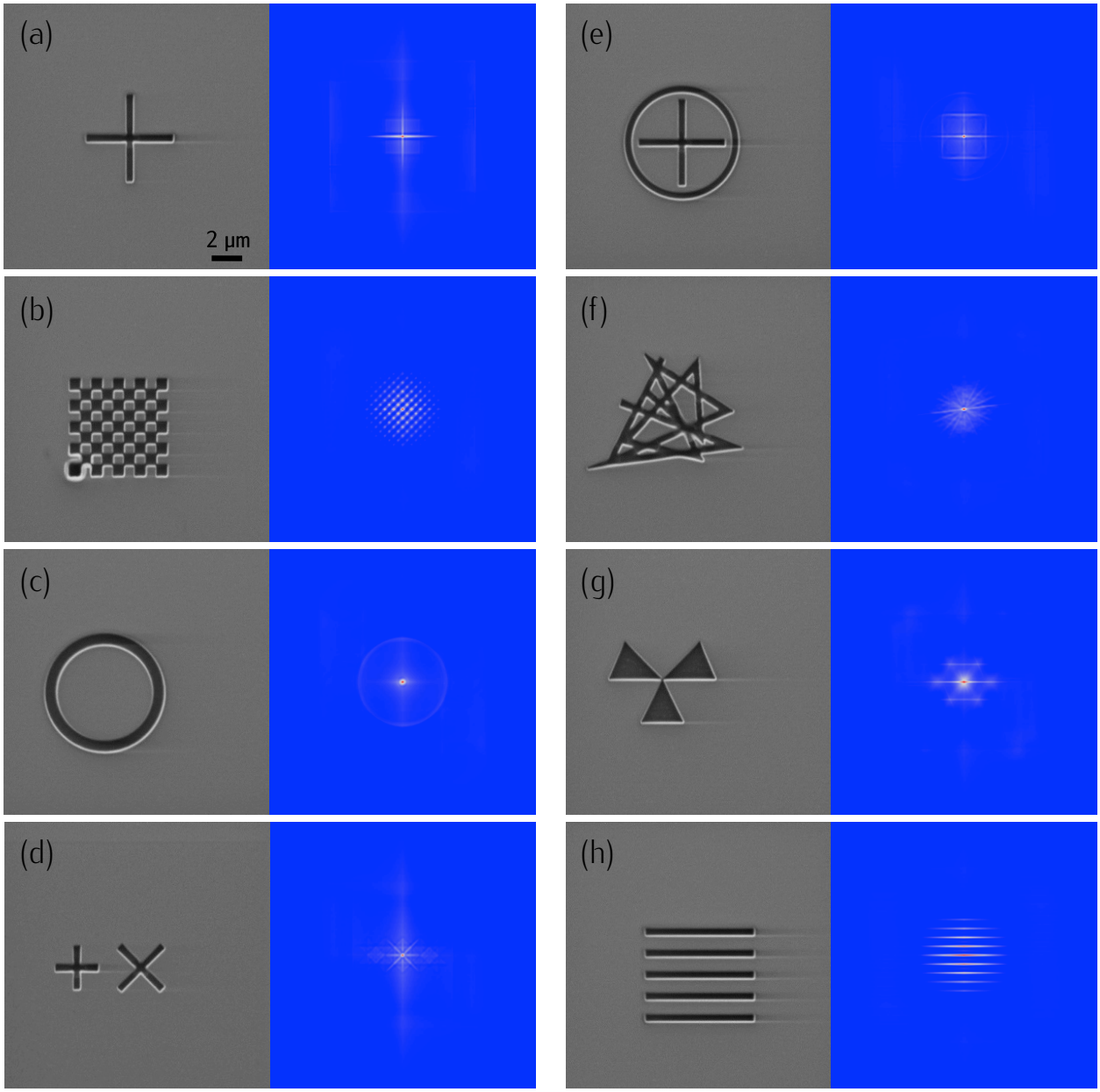

Figure 5.6: SEM images of potential drift marks for IBL drift correction with their corresponding two-dimensional auto-correlation patterns. (a) cross-mark, (b) chessboard, (c) ring, (d) 45° tilted cross marks, (e) combination of ring and cross-mark, (f) randomly arranged lines, (g) triangles and (h) five horizontal lines.

and to be distinct in x- and y-direction, as the beam shift values are defined and applied in these directions. Additionally the slope to the maxima of the correlation plots in x- and y-directions shall be as steep as possible for easy identification. The patterns shall have low writing times (in the range of minutes) and show high contrast in ion-induced SE imaging. All the patterns were milled into 50 nm molybdenum-coated silicon wafers with an ion beam current of 10 pA. 150 loops of the patterns were exposed with dwell times of 0.1 ms.

Table 5.2: Quantitative evaluation of the auto-correlation results.

Pattern	Mean Value [a.u.]	Mean of Side Maxima [a.u.]
Random Lines (f)	**1.2506**	**2.6478**
Ring (c)	**1.5338**	**2.6769**
45° Crosses (d)	1.7387	2.8872
Ring with Cross (e)	1.5076	3.1438
Triangles (g)	1.6228	3.3577
Cross (a)	1.6644	3.7287
Chessboard (b)	1.1719	4.0750
Horizontal Lines (h)	1.4512	5.4220

To quantitatively judge the influence of side maxima, the following procedure was applied to the correlation images and statistical data was extracted for the patterns (see table 5.2). As the ideal correlation image consists of one single peak with low noise surrounding in the rest of the image, the mean values for all the pixels were calculated. Low mean and standard deviation values were expected to be most suitable for drift correction. To judge the influence of side maxima in the correlation images, which originate from local similarities or local periodicities in the pattern, the correlation matrices were divided in 16×16 sub-matrices containing the side-maxima. These side-maxima were identified and averaged. The smaller this mean value was, the smaller the influence of the side maxima to the cross-correlation algorithm was graded.

Summarizing the calculated values, the chessboard pattern (b) and the random line pattern (f) show best results for the mean count values of the correlation images whereas the random line and the ring pattern show the best results regarding the mean values of the side maxima.

Qualitative investigation of the patterns revealed that e.g. the chessboard pattern (b) and the horizontal line pattern (h) show highly periodic correlation signals, whereas e.g. the triangle pattern (g) shows high symmetry. Both of them lead to strong side maxima as confirmed by the calculated side maxima criterion.

As the patterns were imaged by scanning the ion beam over them, the removal and displacement of atoms from the imaged region had to be taken into account. The small features of e.g. the chessboard pattern or the random lines pattern would have been removed relatively quickly, after a small number of image scans. This would lead to degradation of the cross-correlation signal and with high probability let the drift correction algorithm fail during milling of zone plates. Especially at small features and at edges an effect of increased sputter rate is observed. For these reasons, the ring pattern was chosen as ideal mark geometry for IBL-based long time exposures.

Long-term stability under ion beam influence is one of the most important properties of a suitable correction pattern. As described in section 5.1.3, more than 100 drift correction images had to be acquired for a typical zone plate. The ring structure showed big advantages here. Figures 5.7a and b show ion-induced SE images of a ring pattern with 5 µm diameter. A multi-pass milling strategy with 200 passes was chosen for the fabrication of the ring to ensure steep flanks and homogenous depth of the structure. The first image (figure 5.7a) was acquired directly after milling the ring structure, whereas the second image shows the 150th acquisition (figure 5.7b). Image contrast was well pronounced between metal and silicon, even after 150 scans. Pattern degradation can clearly be identified comparing the two images. The edges of the ring pattern were broadened but the center of gravity was constant due to symmetric behavior of degradation for these ring structures.

Figure 5.7c depicts extracted plots from the cross-correlation calculations for different grades of pattern degradation. The first plot (Ref-Ref) shows the correlation between the first image and itself, as benchmark for an ideal signal. After 10 image scans, the comparison of the image with the reference image (Ref-10th) shows a decreasing maximum peak, which is again lower after 150 scans (Ref-150th). Nevertheless, the peak is clearly distinguishable and the side maxima, originating from the slight rise of the cross-correlation result when the rings begin to overlay, are small.

Figure 5.8 shows peak values of the cross-correlation signal in dependence of the number of image scans and normalized to the peak value when comparing the reference image to itself. From this point on and extending to approximately 20 image scans, a slight decrease in signal can be observed. Between 20 and 100 image scans, the signal is stable before it

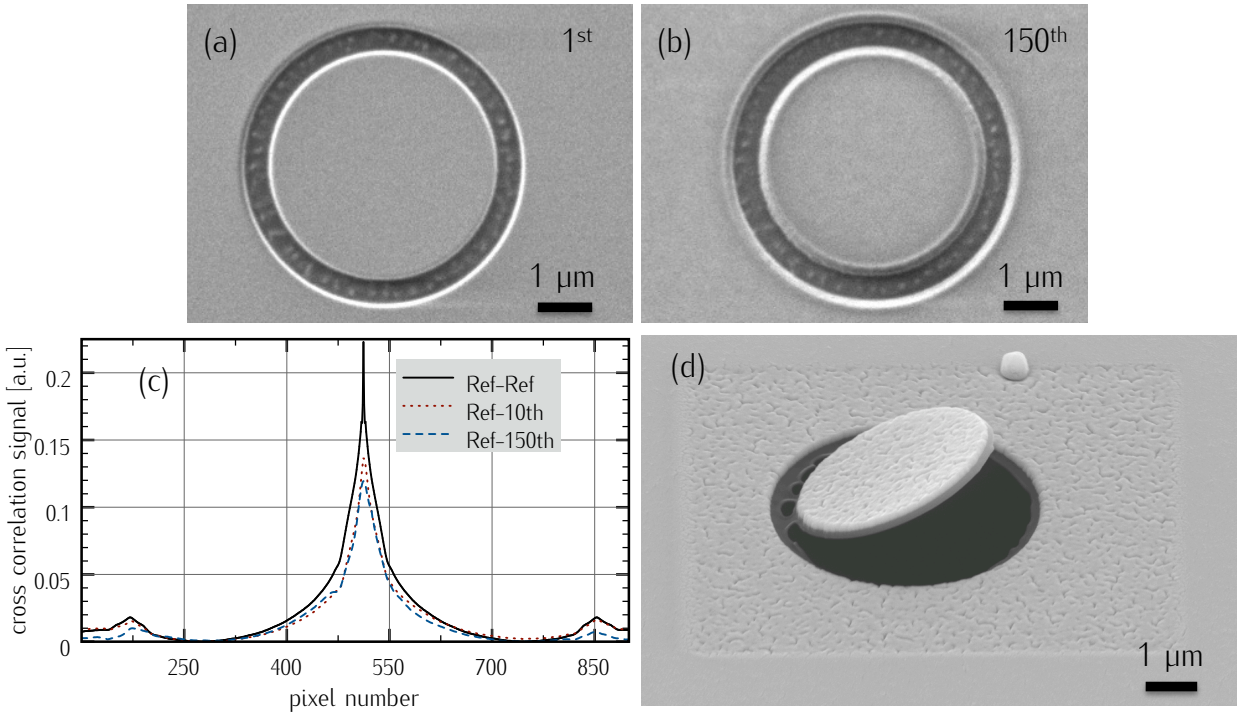

Figure 5.7: (a,b): Ion-induced SE images of a ring pattern used as drift correction mark. Pattern degradation due to ion beam exposure can clearly be identified comparing the 1st and the 150th drift correction image. Scan parameters were 1068 × 1068 pixels scan size at 10 pA probe current, point averaging at level 8 and line averaging at level 3, leading to 40 s acquisition time per image. (c): The cross-correlation signal originating from the comparison of the first correction image (Ref) to itself and the signal from the 10th and 150th image. (d) Effect of worn-out ring-shaped drift correction mark on a silicon nitride membrane (SEM image, tilted view).

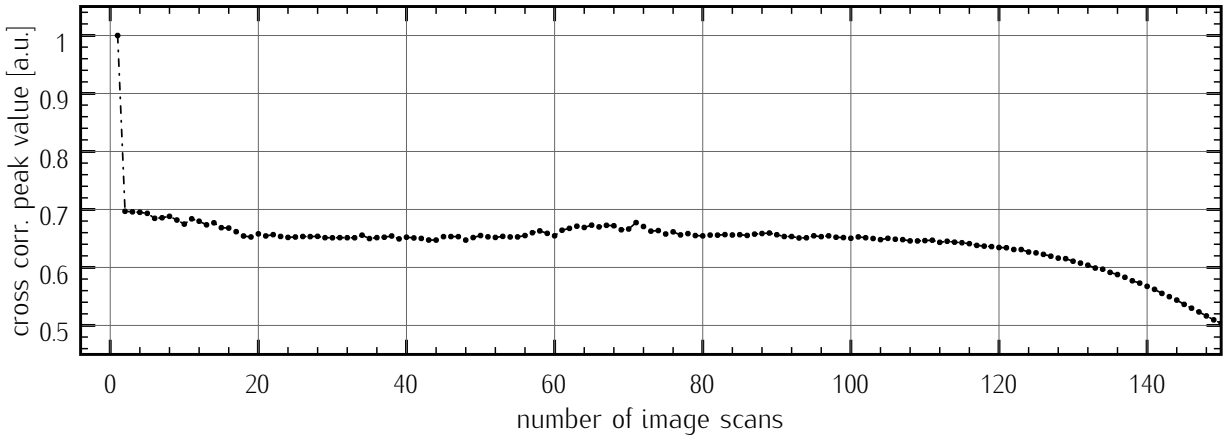

Figure 5.8: Peak values of the extracted cross-correlation signal in dependence of the number of image scans, normalized to the comparison of the first mark image with itself. Between 20 and 100 image scans, the signal is stable and can be used for drift correction.

drops as a result of the pattern degradation described earlier. As a consequence of these observations, the drift pattern was scanned several times after its fabrication and before the reference image was acquired and the actual zone plate patterning process was started. By this, instabilities in the drift correction steps at the beginning of the process did not influence the accuracy of the drift correction procedure. Reasons for these instabilities were for example surface contaminations or little uneven spots that are smoothed during the first image scans. Additionally, changes in image contrast and brightness during the first image scans were avoided.

As no small sub-structures are part of the ring pattern, cross-correlation signal degradation due to this could be neglected. However, structure destruction caused by too much imaging dose can be seen in figure 5.7d. If the integrity of the silicon nitride membrane has been weakened or broken, the central part of the ring was bent up- or downwards and no image correlation was possible any more. This is also true for milling the drift pattern as well as milling zone plates on Si_3N_4 membranes. If the membrane has locally been milled through, membrane rupturing was observed for most cases if residual stress in the membrane or the coating existed. So, precise dose control had to be applied during milling: Too low dose leads to low imaging contrast for drift marks and a residual non-diffracting but absorbing layer for zone plate milling. Too high dose on the other hand leads to failure of the drift correction procedure as the drift mark degrades too quickly. In this case, it does not withstand a sufficiently high number of image scans if the membrane is already locally milled through.

5.1.5 Drift Correction Accuracy

Vernier scales were used to measure the accuracy of the drift correction procedure based on ring patterns (see figure 5.9). They are commonly used to read analog measuring slides at a mm scale and consist of two sets of stripes with a known distance. These stripes are positioned near each other and allow to read scales more accurate than standard scales would. The underlying principle is that one can detect whether two lines are accurately positioned in opposite to each other, even at levels that are below the spacing of a scale. In our case, the principle was used to detect drift correction errors in the sub 100 nm regime. For this, the first part of the *Vernier* scale was milled into the surface, before a drift correction step was carried out by the lithography software suite. The second part of the pattern was milled directly after the drift correction step and the deviation from the ideal position could afterwards be read from the *Vernier* pattern if an image of the scale was

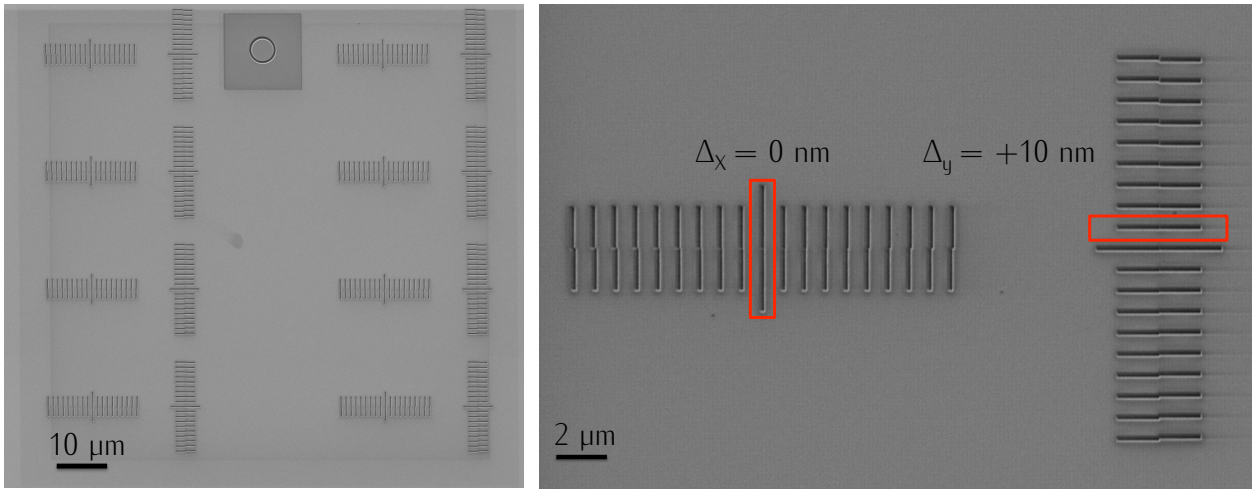

(a) Overview image of *Vernier* patterns with ring-shaped drift correction mark.

(b) Ion-induced SE image of one *Vernier* pattern and corresponding error values in x- and y-direction.

Figure 5.9: IBL-written *Vernier* scales to measure the drift correction errors.

acquired. Zero deviation is found, if the two central lines are aligned. The pattern used for this measurement consisted of lines with 1 µm distance. The distance between the lines in the second set increased from line to line by 10 nm. By this, deviations of ± 90 nm could be measured by imaging the *Vernier* scales. Placing two of the patterns in 90° angle to each other allowed measuring drift correction errors in x- and y-direction. Figure 5.9 shows an array of scales with the corresponding drift correction ring and a detailed image of one *Vernier* pattern. In each measurement, 8 drift correction steps were executed, leading to 8 *Vernier* scales, which were milled in a total time of 1 h 17 min (6 ms area dwell time on a 50 nm Mo-coated Si sample).

The drift correction errors were read from the scales, and mean and standard deviation values were calculated. The described ring-shaped drift marks were investigated at different image-scan parameters and compared to a standard cross-shaped mark. Point average (PA) and line average (LA) values describe the number of SE-signal integrations per pixel and line during image acquisition at a given image edge length in pixels. The experimental data is shown in table 5.3. The cross-shaped mark was scanned with standard scan parameters of 748 pixels edge length at 20 nm effective pixel size and values of PA = 4 and LA = 1. Mean errors of 23 and 24 nm with standard deviations of 16 and 24 nm were measured for x and y directions, respectively. For the first ring structure with less pixels (512 pixels edge length) at 30 nm effective pixel size and neither pixel nor line integrations (PA = 1, LA = 1), the mean values were smaller (≈ 50 %) than the cross-shaped benchmark values. Decreasing

the pixel size to 10 nm (1536 pixels edge length) with the same integration parameters lead to slightly smaller mean error values. Increasing signal integration time to PA = 15, LA = 5 only lowered the standard deviation values. Overall, the standard deviation values were relatively high compared to the corresponding mean values, as the drift correction algorithm operated close to the pixel size of the acquired images. Compared to the cross-shaped structure, the ring pattern at 512 pixels image edge length and lowest integration values was the best trade-off between fast drift image acquisition, low dose-induced pattern damage and sufficiently low drift correction errors.

Table 5.3: Mean drift correction errors $\bar{x}$, $\bar{y}$ and corresponding standard deviations σ_x,σ_y measured by *Vernier* scales for ring and cross patterns at different image acquisition parameters. PA: Point average. LA: Line average.

Pattern, Acquisition Parameters	$\bar{x}$ [nm]	$\bar{y}$ [nm]	σ_x [nm]	σ_y [nm]
Cross, 748 × 748, PA=4, LA=1	23	24	16	24
Ring, 512 × 512, PA=1, LA=1	14	12	20	9
Ring, 1536 × 1536, PA=1, LA=1	14	6	15	11
Ring, 1536 × 1536, PA=15, LA=5	6	14	9	9

Summarizing, the described drift correction process based on ring-shaped structured is capable of delivering stable drift correction for zone plates with outermost zone widths of 100 nm, if a zone placement accuracy of at least 1/3 of an outermost zone width is required [Michette, 1986]. This fits to the estimation of the possible structure size in section 5.1 for ion beam currents in the range of 10 pA to 100 pA. This range of currents is suitable for zone plate milling regarding beam diameter and required dwell time.

5.1.6 Zone Plate Milling

There are two writing strategies that can be used for structuring of zone plates:

(a) Milling the whole zone plate pattern for a small fraction of the total exposure time and performing a drift correction step subsequent to this. If this procedure is repeated for some hundred times, until all the metal is removed down to the silicon nitride substrate, this

leads to the desired structure. For this multi-pass approach, the total drift budget (typically $0.3 \cdot \Delta r_N$ for zone plates [Michette, 1986]) is spread equally over all zones. This degrades the ideal 1:1 gap-to-structure ratio of zone width to trench widths. Additionally, the total dose needed to reach the final depth is higher than in single-pass mode due to redeposition and re-sputtering effects. This is a fundamental difference to EBL-based processes, where mainly exposure dose, not exposure strategy affects the results.

(b) The second strategy is to use a single-pass approach and mill the individual zones subsequently to each other. Generally, this leads to shorter total exposure times and to the effect that drift correction errors affect each zone separately. The zone placement accuracy depends on the error made during the previous drift correction step. Typically, the single-pass strategy leads to sloped and non-uniformly deep structures due to the redeposition of sputtered atoms and the angle dependence of the sputter yield. For zone plates, rounded and asymmetric zone profiles are the consequence. For the zone plates described herein, the Ga^+ ion beam current was chosen such that the beam size was slightly less than the smallest desired zone width, which was approximately 100 nm beam diameter for 74 pA beam current. In combination with using four milling passes per zone, a reduction of the effect of sloped structures was achieved. At the same time, this minimized the exposure time.

Table 5.4: Design parameters for zone plates M52 and W2. Given values are the zone height z_{AuPd}, width of the outermost zone Δr, the radius of the zone plate r_N, the number of zones and the focal length f at $\lambda = 13$ nm.

Zone Plate	z_{AuPd}	Δr	r_N	# zones	f
M52	100 nm	121 nm	48 µm	200	900 µm
W2	300 nm	121 nm	48 µm	200	900 µm

Two sets of zone plates with differing zone heights were milled on the *Zeiss XB1540* FIB system. The zone plates were named M52 and W2 (see figures 5.10, 5.11 and 5.12). Both were fabricated in gold-palladium, used the same design and were placed on 100 nm thin silicon nitride membranes on a silicon frame with 3 mm diameter. For zone plate M52, a 100 nm layer of AuPd (80/20) was deposited onto the membrane at $5{\cdot}10^{-2}$ mbar pressure and 60 mA sputter current. For the outermost zones, it was expected to have a non-rectangular zone profile due to beam tails of the Ga^+ ion beam and therefore zone heights smaller than

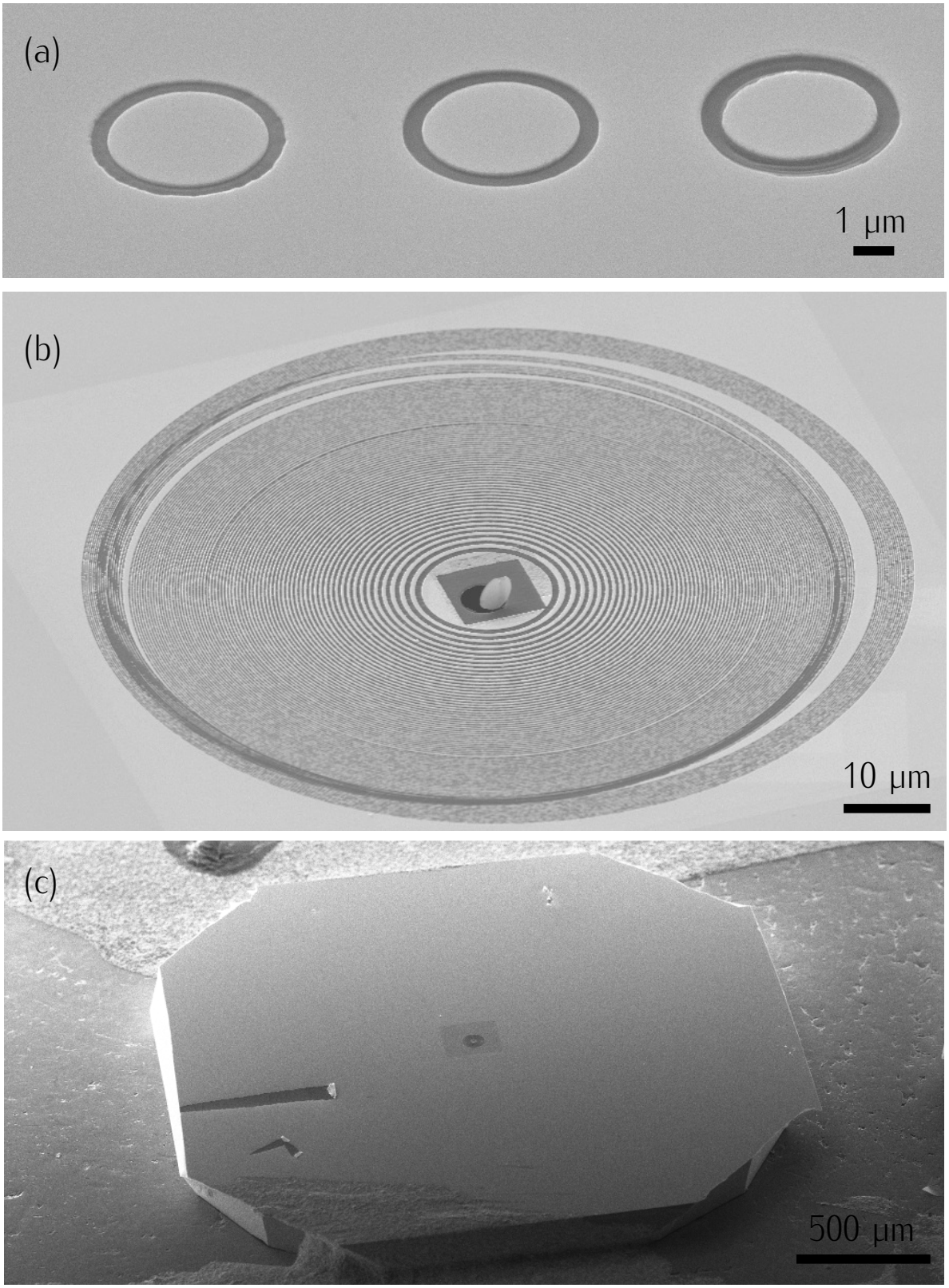

Figure 5.10: Scanning electron microscope images of preparatory steps for zone plate M52. (a): Drift ring dose increases from left to right by dose factors 1, 2, 3. Basic dose: 26 mC/cm^2. (b): Result of degrading cross-correlation signal and complete removal of the metal layer within the drift mark scan area. Milling direction: inside to outside. (c): Silicon substrate with Si_3N_4 membrane glued to a sample holder. Zone plate is placed on the membrane.

100 nm. As described before, this leads to the case of a phase zone plate and ideal diffraction efficiencies $> 10\,\%$. Figure 5.10a shows drift ring structures, milled with 26 mC/cm^2 basic dose, applied within 4 loops and dose factors from 1 to 3 (from left to right). Dose factor 2 was ideal as 1 showed rough edges and 3 was milled not only through the metal, but also trough the membrane. This would lead to a pattern rupture after a few drift correction steps. Figure 5.10b shows the effect of drift pattern degradation and not properly working drift correction. Ion bombardment during drift image acquisition completely removed the metal layer and the silicon nitride in the ring. The outermost zones were therefore misplaced and the zone plate is unusable. Hence, the dose applied during drift correction was decreased by larger pixel sizes within the drift correction images (from 1000 to 800 pixels edge length). Additionally, drift correction steps were only performed every 6 zones instead of every zone. By this, stable drift correction could be achieved.

For the second zone plate (W2), 300 nm AuPd was deposited onto a silicon nitride membrane. The transmission of this layer for $\lambda = 13$ nm is 10^{-6}. Due to this zone height, the lens is considered to be a pure amplitude zone plate. The radii of the individual zones were calculated using a script written in *Matlab*. After conversion to ring structures with the desired widths, the zone plate design was exported in *GDS II*[26] format. To comply with the accuracy data derived in the previous sections, the design parameters shown in table 5.4 were chosen for zone plate fabrication.

A write field of 100 µm edge length was a trade-off between fabrication time and zone plate size. As the zone plate diameter was 97 µm with 200 zones, a drift correction mark of 5 µm diameter could placed either in one of the corners of the write field or in the center of the zone plate, if some of the inner rings were sacrificed. The first option was followed for zone plate M52, the second for zone plate W2. The centered position of the drift mark was an advantage during the alignment of the zone plate in the EUV microscope because of pattern symmetry. A zone plate design with outermost zone width of $\Delta r = 121$ nm was calculated and used for the fabrication process. This outermost zone width enables theoretical resolutions of $R_{Rayl.} = 1.22 \cdot \Delta r = 148$ nm in the EUV microscopy setup. Ion beam adjustment was performed on the membrane as near as possible at the position of the write field.

After dose adjustment experiments, two sets of parameters were selected to fabricate the zone plates. M52 was written with 74 pA beam current and a dose of 25.7 mC/cm^2. Figure 5.11 shows the zone plate (a,b,c) and the effect of exceedingly high dose values (d,e). Increasing the dose by 25 % (from 26 mC/cm^2 to 32 mC/cm^2) did not result in milling through

[26] Graphic Data System II: a file type to describe lithographic structures. Originally developed to design two-dimensional integrated circuits in separated layers.

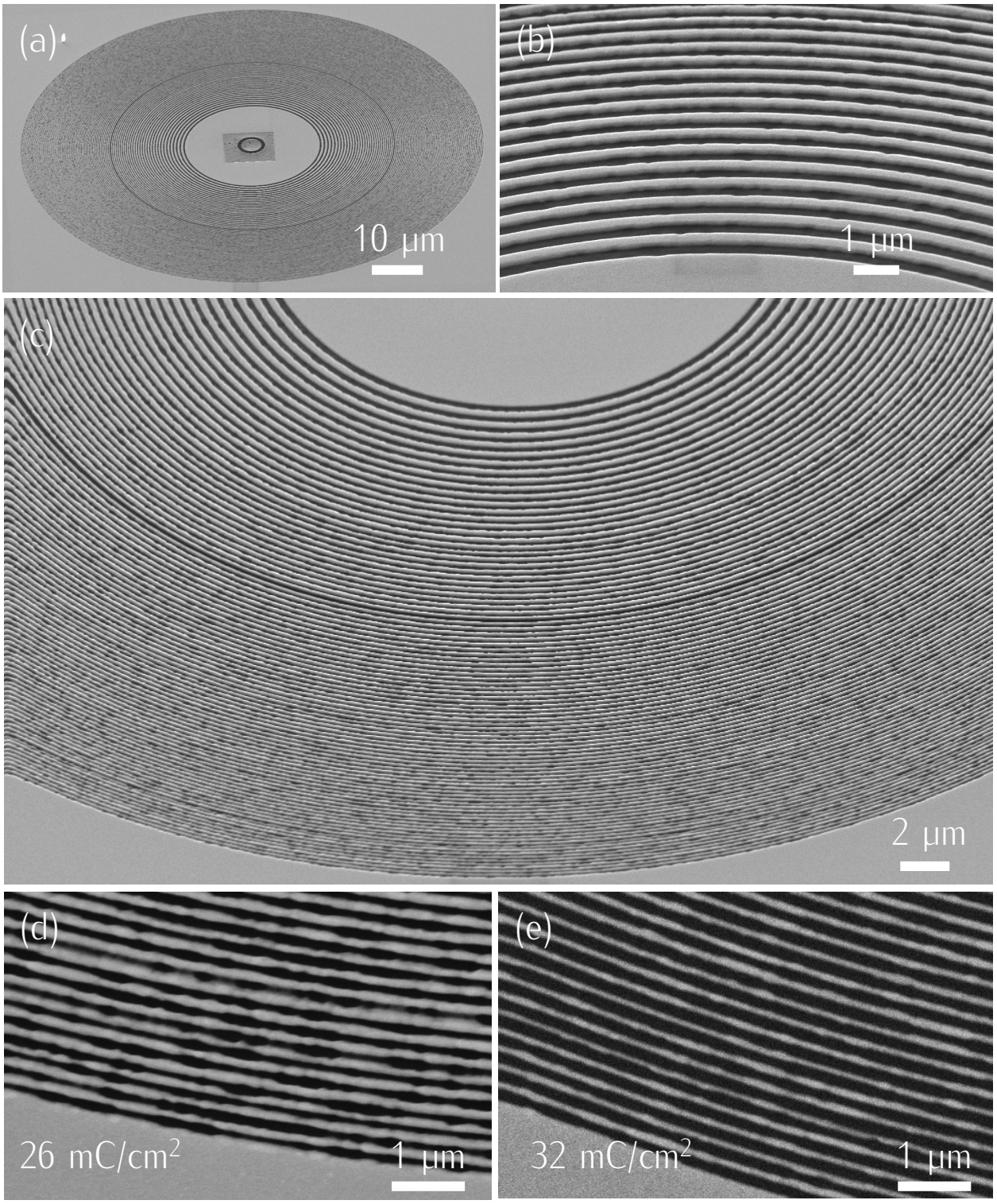

Figure 5.11: (a,b,c): Scanning electron microscope images of zone plate M52. 100 nm AuPd, t = 3 h 25 min, I = 74 pA, d = 26 mC/cm^2, measured structure height 113 nm. Drift correction was performed every six zones. The dark ring at r/2 of the zone plate is due to a short instability of the ion source. (d,e): outermost structures at 26 mC/cm^2 and 32 mC/cm^2.

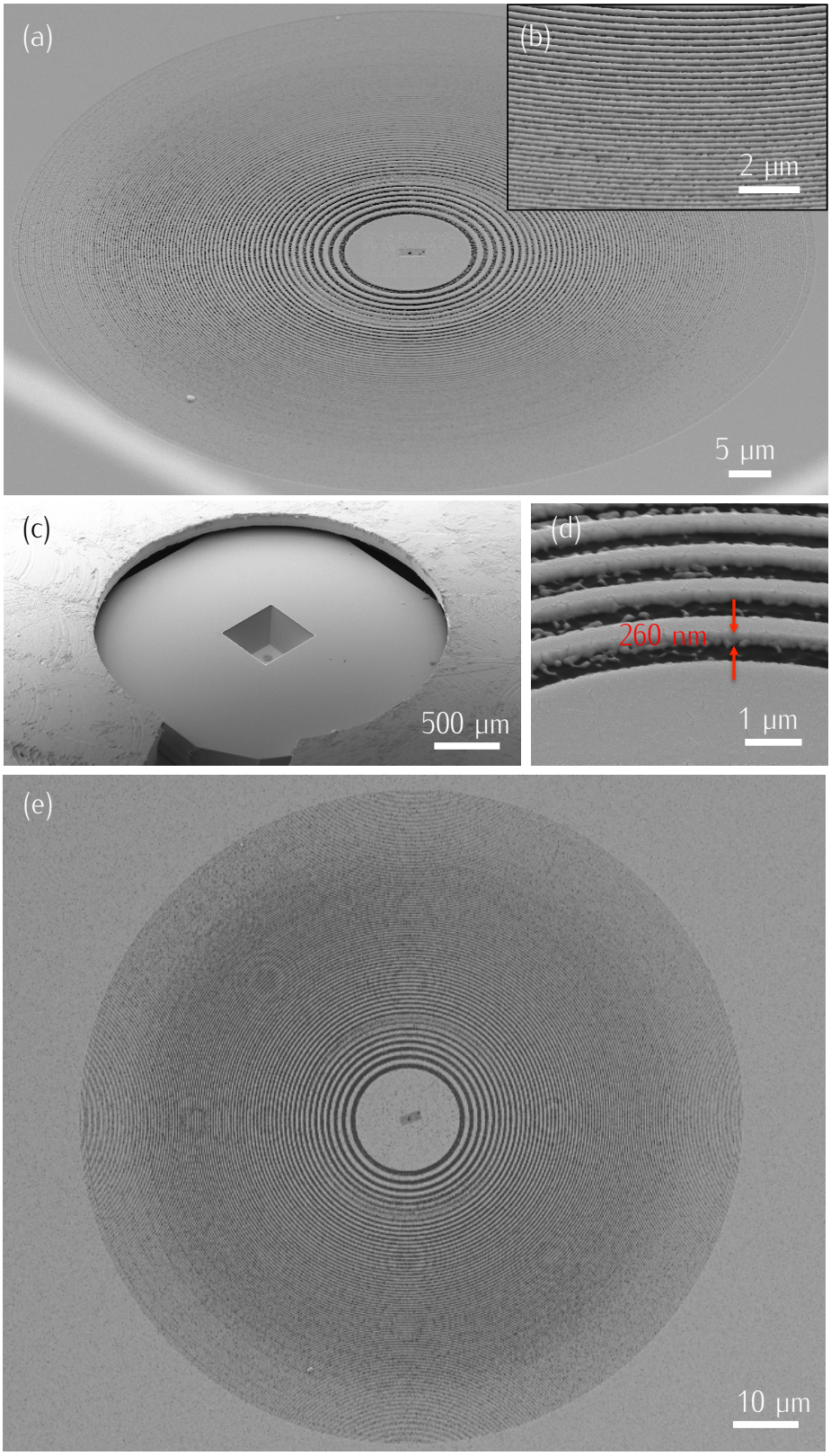

Figure 5.12: (a,b,c,d,e): Scanning electron microscope images of zone plate W2: 300 nm AuPd, t = 8 h 30 min, I = 53 pA, d = 62 mC/cm^2 to 80 mC/cm^2 for the outermost rings, measured structure height 260 nm. Drift correction was performed every eight zones. Ion beam adjustment was performed at the center of the zone plate. (c): Silicon frame and clamp arrangement in the FIB microscope. (d): Tilting the microscope stage to 36° allows measuring of heights.

the membrane, but to gap-to-line-ratios deviating from the ideal 1:1 value. The zone plate pattern was partitioned to sub-patterns containing 6 zones after which a drift correction step was performed. Every sub-pattern was milled within 4 loops. The total milling time was 3 h 25 min. The inner 20 zones were left out for placing the drift correction mark in the center of the write field.

Zone plate W2 (Figure 5.12) was fabricated with 4 milling passes, an ion beam current of 53 pA and a basic dose of 62 mC/cm^2. The dose was gradually increased to 80 mC/cm^2 towards the outer zones as higher dose was needed for milling the more narrow features to the same depth as the broad inner zones. This effect can be explained by the beam tails of the ion beam and increased redeposition effects. The total writing time was 8 h 30 min. As the silicon nitride membrane was coated with a thicker metal layer, the membrane itself was not visible in the SEM image during the beam adjustment procedure (compare figure 5.10c with figure 5.12c). For this reason, the silicon frame was mounted upside down for the coating and milling steps. This allowed easy navigation to the membrane window.

Structure heights were measured to be 113 nm for M52 and 260 nm for W2. For M52, this means that also a part of the silicon nitride had been removed. The mean drift values between two drift correction steps were 23 nm and 16 nm for M52 and W2, respectively.

5.1.7 EUV Microscopy

The gold-palladium zone plates fabricated with the *Zeiss XB1540* FIB system were tested in a full field imaging setup at 13 nm wavelength. For this purpose, a microscope was constructed on basis of an ethanol-jet laser-induced plasma source. A schematic overview of the optical layout is presented in figure 5.13. Basic properties of the light source are described in section 3.3. As only the 13 nm emission line of oxygen was used for imaging, all other spectral components had to be blocked. This was realized by a 200 nm thick Zr filter foil and a pair of multilayer mirrors with narrow spectral transmission profile. These mirrors were also used as condenser system to illuminate the objective plane.

The zone plates were used to magnify an image of the specimen to a CCD camera. All components were mounted on motorized stages to allow adjustment of the relative geometric positions of the optical components during the experiments in vacuum. The restricting two design parameters for the microscope were (a) the diameter of the plasma chamber and (b) the size of the microscope chamber: (a) The vacuum chamber that housed the

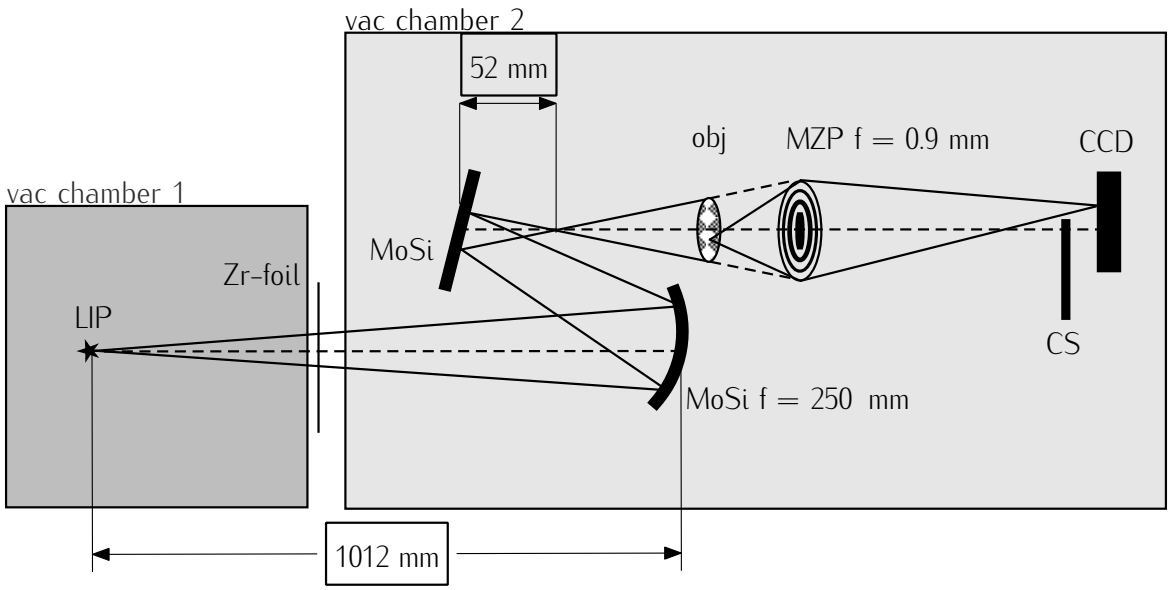

Figure 5.13: Schematic of the optical setup used for the EUV microscope. The laser-induced plasma source (LIP) emits a broad band of wavelengths, from which only the oxygen line at 12.99 nm ($1s^2 2p - 1s^2 4d$) passed the zirconium filter element (Zr) and the molybdenum-silicon multilayer mirrors (MoSi) [Kramida et al., 2013]. The first mirror was spherical with a focal length of f = 250 mm and acted as condenser. It illuminated the object (Obj), which was imaged by the zone plate (MZP) onto the detector (CCD). A central stop (CS) was placed in front of the detector to block the 0^{th} order of diffraction.

plasma source was a cylindrically shaped with 60 cm diameter and a standardized KF-40 flange as output port for the X-rays. Optical elements that are directly exposed to the plasma suffer from degradation by fast particle bombardment and deposition of debris. In ethanol-based sources, mainly carbon is deposited on all surfaces surrounding the plasma. The diameter of the chamber determined the distance to the first optical element in the microscope chamber, because a vacuum lock and a filter foil holder had to be mounted in the connecting vacuum tube. The distance from the plasma to the first mirror element was therefore limited to approximately 1 m. (b) The microscope chamber was rectangular, with three KF-40 ports on each side, 90.75 mm separated from each other. This limited the optical path of the microscope, because two multilayer mirrors were used as condenser. The optical path was therefore folded and two major optical axis occurred, parallel to each other (see figure 5.13).

5.1.8 Optical Layout

For testing the fabricated zone plates in terms of achievable resolution, it had to be ensured that the constructed microscope was capable of delivering at least the zone plate's resolution. For that purpose, the optical system was designed to allow magnifications V up to 900-fold. Assuming a zone plate with focal lengths of $f = 900\,\mu m$, the image distance b (distance of zone plate to detector) and the object distance g (distance of zone plate to object) can be calculated by the imaging equation:

$$\frac{1}{f} = \frac{1}{g} + \frac{1}{b}. \tag{5.5}$$

For the desired magnification of $V \approx 700–900$, this leads to object distances g approaching the focal length of the zone plate ($f = 0.9\,mm$) and values of image distances in the range of $b \approx 600 - 800\,mm$. A CCD detector of type *Princeton Instruments PI-SX 1300* was used for the experiments. It is equipped with an array of 1340×1300 pixels of $20\,\mu m$ edge length. Calculating the effective field of view for the given values of V leads to 30 to $40\,\mu m$ field diameter at effective pixel sizes of 20 to 30 nm for the given CCD chip. This meets the requirements for imaging resolution, as the zone plates were expected to show resolution limits higher than 100 nm. Typical values for the geometric properties of the microscope in two typical imaging setups are given in table 5.5.

Table 5.5: Geometry values for the optical layout of the imaging system at two typical imaging conditions.

Magnification	698-fold	859-fold
Distance plasma to spherical mirror	1012 mm	
Focal length of zone plate design MZP-020	900 µm	
Diameter of zone plate design MZP-020	96.8 µm	
Image distance	628 mm	773 mm
Effective detector size (field of view)	38 µm	31 µm
Effective pixel size	28 nm	23 nm

5.1.9 Laser-Induced Plasma Source

The laser-induced plasma source was driven by a *Coherent Infinity* laser system described in section 3.3. It delivered 3 ns pulses of $\lambda = 1064$ nm wavelength that were converted to 532 nm by second harmonic generation. Infrared pulse energies of up to 300 mJ were reached in practical use. The laser was focused onto the ethanol-jet and X-ray emission was observed. Besides several carbon emission lines, the oxygen line at 12.99 nm ($1s^2 2p - 1s^2 4d$) was most important for the described experiments. To optimize the emission characteristics of these lines, absolute photon numbers were measured by a calibrated grating and CCD chip. The design of the slit-grating spectrograph is described in [Wilhein et al., 1999]. The used calibration data for the camera and the grating were acquired at Beamline BW3 at the electron storage ring *DORIS III* at *DESY* [Schäfer, 2010]. For the measurements described herein, a freestanding grating with periodicity of $g = 100$ nm was mounted on a slit with $D = 50$ µm diameter. The grating was illuminated by the X-ray source and diffracted light to a CCD detector mounted downstream of the optical axis. A 150 nm Zr filter foil was used to protect the grating from the debris originating from the plasma. The complete spectrum could not be acquired on one single CCD frame, as the 0^{th} order of diffraction was too bright to image it at the same time with the much weaker spectral lines in the $+1^{st}$ order. The dynamic range of the detector was the major limit here. To compensate that, the CCD was mounted on a rail system to be able to pan it to the desired region of the spectrum and block the 0^{th} diffractive order.

The combination of grating constant and slit-width corresponds to 500 illuminated grating bars, leading to an achievable spectral resolution of $\lambda/\Delta\lambda = 500$. The second parameter that influences the total spectral resolution is the geometric resolution of the setup. It mainly

depends on the sizes of the slit D and the light source q, as well as the distance of detector to grating b and the distance of plasma to grating g. So to say, the projected size of the slit onto the detector is limiting the achievable resolution [Wilhein et al., 1999]. It can be written as

$$\Delta\lambda_g = g\left[\frac{D+q}{g} + \frac{D}{b}\right]. \tag{5.6}$$

For the used setup, the plasma size was $q = 20\,\mu m$ and the distances were adjusted to $g = 1140\,mm$ and $b = 807\,mm$. At the desired wavelength of approximately 13 nm, a geometric resolution of $\Delta\lambda_g = 12.8\,pm$ was expected from the setup. This corresponds to a relative spectral resolution of $\lambda/\Delta\lambda_g = 1019$, exceeding the resolution determined by the number of illuminated slits by a factor of 2. The pixels of the used CCD camera were sized $20\,\mu m \times 20\,\mu m$, corresponding to 2.5 pm per pixel for the given geometry in the acquired spectra. Summarizing the limitations, the setup was purely diffraction limited by the number of illuminated grating periods. A larger slit could have been used for an even higher spectral resolution and higher photon numbers. However, regarding the aim of the experiment, this was not required, as resolution was sufficiently high and exposure times were in the range of minutes.

There are two possibilities to assign wavelength values to the acquired spectra. The first is to measure the distance of the 0^{th} order peak to the desired spectral line in the first order and to calculate the corresponding wavelength based on the geometric parameters like diffraction angle and the distances of the components. This is relatively error-prone because only wavelength intervals of 2 to 5 nm can be imaged on one CCD frame. One has to stitch several images until the interesting region around 13 nm is reached. The more accurate method is to use the diffraction signal of the support stripes on the grating. A grating constant g_s can also be assigned to these structures, which run perpendicularly to the primary grating bars. Figure 2.7 in section 2.3.3 shows such a typical support structure that is used to stabilize the freestanding grating bars. This secondary grating constant is always larger compared to the primary structure, leading to smaller angles of diffraction. Figure 5.14 shows a spectrum acquired in the region of 12 to 16 nm. The image was inverted for better visibility and shows the $+1^{st}$ order of regular diffraction in horizontal direction and at the same time the 0^{th}, $+1^{st}$ and -1^{st} orders of diffraction originating from the support stripes. For every distance x measured from the 0^{th} to the 1^{st} order of the support stripes ($g = 1.5\,\mu m$), wavelength calibration with errors of less than 1 % can be performed:

$$\lambda \simeq g_s \cdot \frac{x}{b}. \tag{5.7}$$

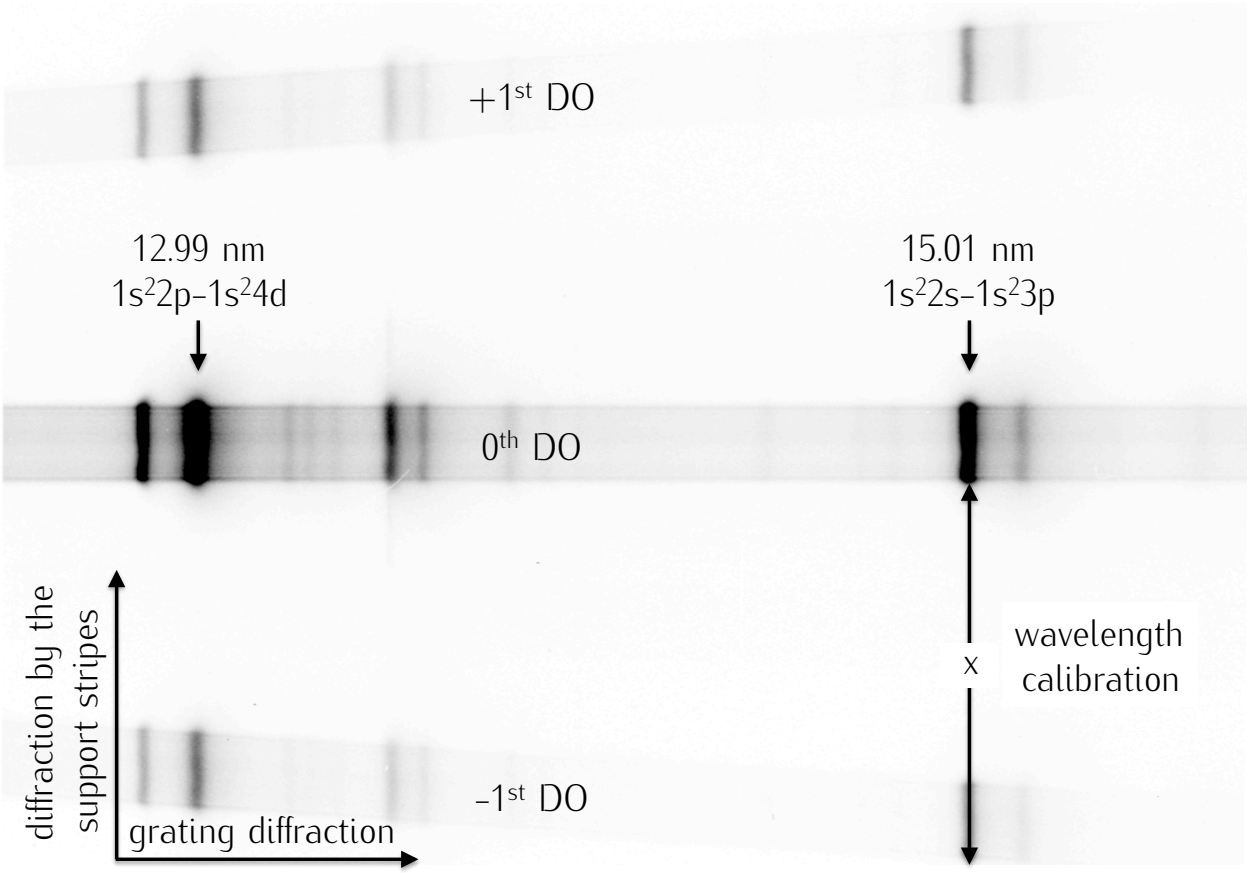

Figure 5.14: Part of the spectrum acquired by the slit-grating spectrograph in the region of $\lambda = 11$ to $\lambda = 16$ nm. The image was inverted for better visibility. The diffraction signal of the grating (marked by 0^{th} DO) can be seen in horizontal direction whereas the signal of the grating support stripes (0^{th}, $+1^{st}$ and -1^{st} DO) are visible in vertical direction. Wavelength calibration can be performed by measuring the distance x, if the grating constant of the support structure g_s is known.

Figure 5.15 shows the spectral sensitivity of the CCD chip and the diffraction efficiency of the used grating in dependence of the wavelength. From the data at $\lambda = 12.99\,\text{nm}$, a sensitivity of the CCD chip of 4.46 counts per incident photon and approximately 1 % diffraction efficiency of the grating was extracted by interpolation. To judge the quality of a light source, the brilliance is commonly used in X-ray optics. The brilliance is defined as the number of photons that are emitted from the source per time interval, interval of solid angle, emitting area and relative spectral bandwidth. It describes the photon flux with respect to the size of the light source and its angular and spectral emission characteristics. For non-continuous light sources, the expression is normalized to one single pulse and thus the following units are used:

$$[\mathrm{B}] = \frac{1}{\mathrm{sr} \cdot \mu\mathrm{m}^2 \cdot \mathrm{pm}}. \tag{5.8}$$

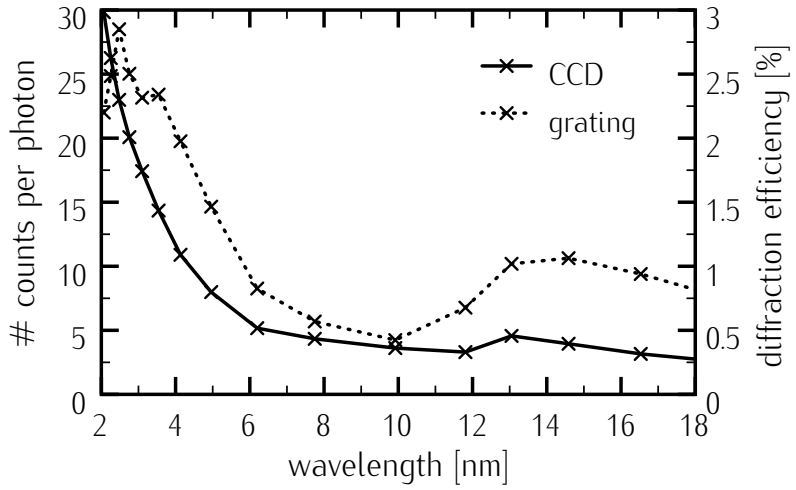

Figure 5.15: Calibration data of the used camera (*Princeton Instruments PI-SX 1300*) and the grating. Acquired by [Schäfer, 2010] at beamline BW3 at *DORIS III* electron storage ring.

To attain lowest possible image noise, the spectra were acquired with the CCD chip cooled to -40°C and with the electronic set to low analog gain. A readout rate of 100 kHz was used at exposure times of 600 s. The laser-plasma was driven by the laser with IR-pulse energy settings of 150, 200, 250 and 300 mJ at 100 Hz repetition rate. A 150 nm Zr filter foil was used for stray light suppression and for vacuum separation. Dark images were subtracted from the spectra before processing. Figure 5.16 shows the results of the experiment in the region

between $\lambda = 12$ and 16 nm. The two brightest lines at 12.99 nm and 15.01 nm are both oxygen lines with values of over 10^{13} photons/(sr µm^2 pm). Additionally, the spectral reflectivity of the used multilayer mirrors is plotted in the figure. Besides a carbon emission line at $\lambda \approx 13.5$ nm, which will be highly suppressed by the multilayer mirrors in the microscope setup, two oxygen lines at 12.84 nm (1s2p-1s3d) and 12.99 nm (1s^{2}2p-1s^{2}4d) are reflected by the mirrors and pass the condenser arrangement [Kramida et al., 2013]. The 12.99 nm line will be the major line in the microscope and used for microscopic imaging. Especially at the transition between 250 mJ and 300 mJ IR pulse energy is important for the two oxygen lines below 13 nm. Both lines are brighter at 300 mJ, but the 12.84 nm profits more from the higher pulse energy compared to the 12.99 nm line. So, 250 mJ infrared pulse energy seems to be most suitable for driving the microscope at 12.99 nm whereas 300 mJ is preferable at 12.84 nm wavelength. The FWHM value for the 12.99 nm peak is 50 pm. Within this spectral line, approximately 10^7 counts are measured in the spectrum, corresponding to a total number of emitted photons in 4π sr of $1.1 \cdot 10^{10}$ photons per pulse.

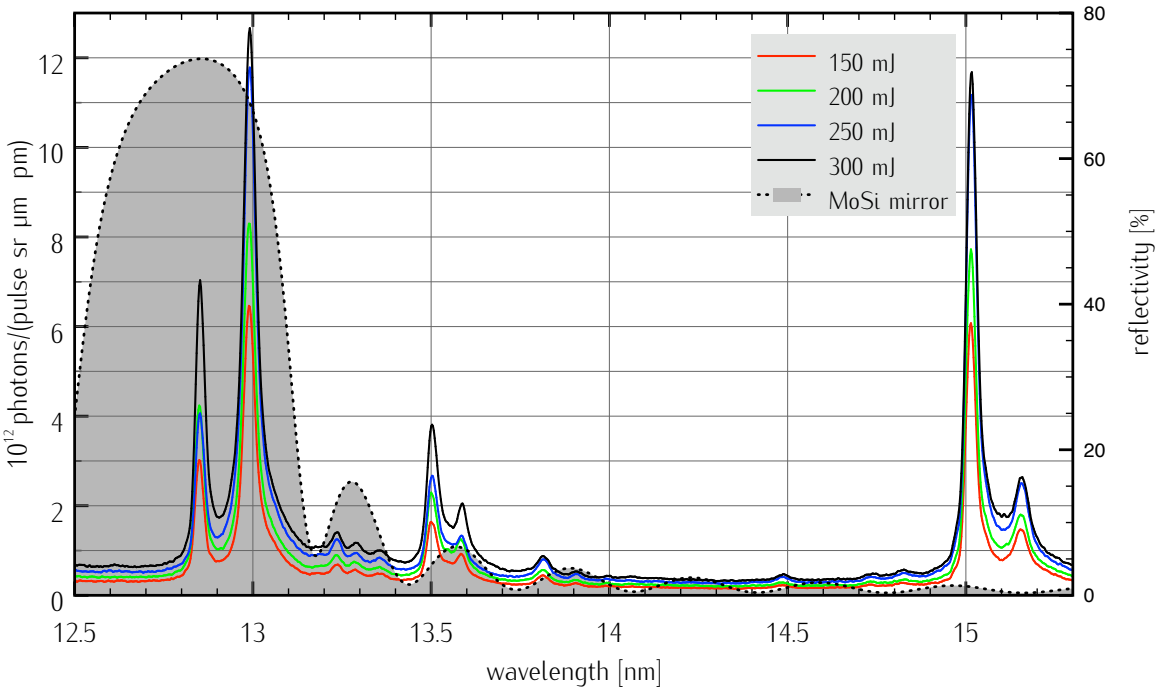

Figure 5.16: Measured brilliance curves of the laser-induced plasma source at different laser pulse energies and reflectivity of the used multilayer mirrors [Kohn, 1995]. Two oxygen lines fit into the reflectivity curve: 12.84 nm (1s2p-1s3d) and 12.99 nm (1s^{2}2p-1s^{2}4d).

5.1.10 Condenser System

As depicted in figure 5.13, the condenser system consisted of two molybdenum silicon (MoSi) multilayer mirrors. The multilayer structure is deposited onto 1 inch glass substrates[27], which were mounted on motorized rotatable mirror holders.

The first mirror was spherical, with 500 mm curvature radius, corresponding to a focal length of $f = 250$ mm. The theoretical reflectivity of one mirror is 0.7 at $\lambda = 13$ nm, leading to a total transmission of the condenser system of ≈ 0.5. The number of photons per pulse that were delivered to the condenser system by the laser-induced plasma source can be estimated by the geometric conditions. Photon numbers for the 12.99 nm oxygen line were measured and described in section 5.1.9. In 4π sr solid angle, $1.1 \cdot 10^{10}$ photons per pulse were measured within a bandwidth of 50 pm. Assuming a distance of the plasma to the first mirror of 1012 mm and 1 inch mirror substrates, a solid angle of $4.95 \cdot 10^{-4}$ sr can be calculated. With the transmission of the 200 nm Zr filter foil of 51 %, this leads to $2.2 \cdot 10^{5}$ photons per laser pulse that were collected by the condenser system.

The spherical mirror was placed approximately 1 m from the laser-plasma because of geometric limitations of the vacuum chambers. The mirror was tilted by 9.5° in order to deflect the beam by 19° onto the second mirror, whose planar shape reflected the optical axis of the system parallel to the first optical axis with a lateral distance of 90.75 mm (determined by the distance between the two flanges of the rectangular vacuum chamber). The object, the zone plate and the detector were placed on this second optical axis. Compared to a zone plate condenser with typical diameters smaller than 1 mm and diffraction efficiencies of lower than 10 %, the mirrors (1 inch diameter) are more efficient and collect a larger fraction of the light in terms of solid angle.

The spherical mirror was tilted to the optical axis. This changed the focusing properties significantly. The most important consequence is that astigmatism was introduced. This means that the focal length is different for the meridional and the sagittal plane of the mirror, leading to two focal lengths separated by a fixed distance on the optical axis. For the sagittal focal length f_s and the meridional focal length f_m, the values depend on the incident angle α [Wieland, 2004]:

$$f_s = \frac{R}{2} \cdot \frac{1}{\cos \alpha} \tag{5.9}$$

$$f_m = \frac{R}{2} \cdot \cos \alpha. \tag{5.10}$$

[27] AXO DRESDEN GmbH, 01237 Dresden, Germany

Table 5.6: Geometry values for the optical layout of the condenser system.

Distance from plasma to spherical mirror	1012 mm
Angle of incidence on mirrors	9.5°
Focal length of spherical mirror	250 mm
Mean imaging distance of condenser	332 mm
Effective focal length in meridional plane	246 mm
Imaging distance in meridional plane	326 mm
Effective focal length in sagittal plane	253 mm
Imaging distance in sagittal plane	338 mm
Difference of focal lengths	7 mm
Difference of imaging widths	12 mm
Numerical aperture of condenser	0.038

As shown in table 5.6, the two focal lengths of the used mirror system differed by $f_s - f_m = 6.9\,\text{mm}$. As the light source was not imaged from infinite distance, a calculation of the imaging widths, i.e. the real distances of the focal spots from the spherical mirror, leads to a difference of 12 mm. An alternative position of the spherical mirror would have been on the optical axis and not tilted, with the plasma located in-between the mirror and the object, as for example described by *Hertz et al.* for water window X-ray microscopy based on a nitrogen plasma source [Hertz et al., 2012]. In this concept, the multilayer mirror had to be placed near the plasma, where it is strongly exposed to particles from the plasma. For microscopy in the water window and with plasma targets that show only low debris emission (like liquid nitrogen), this is suitable in practice. Compared to those of EUV wavelengths, the reflection characteristics of multilayer mirrors for water window applications are less disturbed by thin films of carbon-containing debris that are deposited on their surfaces. So, this concept could not be used for the microscope concept described herein because the reflection properties at $\lambda = 13\,\text{nm}$ would have been strongly affected by the deposited carbon originating from the plasma products of ethanol.

Simulations of the optical setup performed by the raytracing software *Oslo LT*[28] confirm the calculations. Figure 5.17 shows the radii of the beam in sagittal and meridional plane as function of the distance to the second mirror with 1 mm step size. Minima are reached at the two focal spots with radius values of approximately 7 µm for the short axis, while the long axis of the same spot extends 174 µm in radius. Between the two spots, a crossover of

[28] Sinclair Optics Inc., Pittsford NY, USA

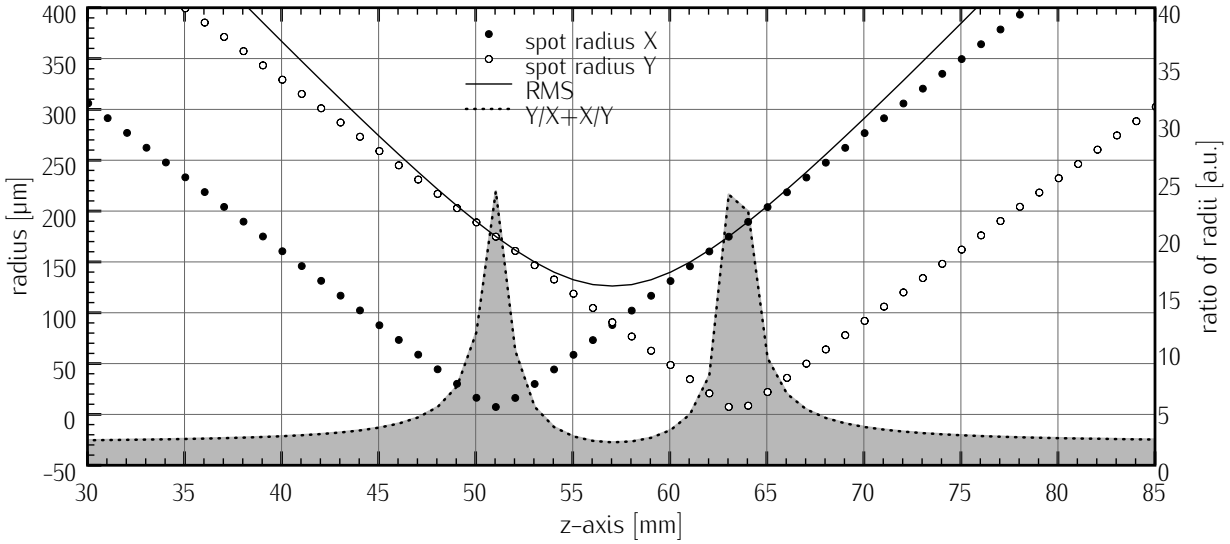

Figure 5.17: Simulated beam radius values after passing the condenser system, plotted against the distance from the second, plane multilayer mirror. Strong astigmatism is observed, as the focal lengths of the spherical mirror is dependent on the regarded plane (meridional and sagittal). Additionally, the ratio of the radii is plotted to emphasize the strongly differing values and the region after 70 mm distance where the beam diameters converge.

the curves is reached at radius values of 88 µm. This would be a suitable point for placing an evenly illuminated sample. The astigmatism, however, would lead to a very unevenly illuminated zone plate for this setup. Only a vertical stripe of the lens would be illuminated, leading to a reduced diffraction signal and thus to longer exposure times at microscopic imaging.

Additionally, the diameter of the focal spot (7 µm) was too small to illuminate a large enough field of view (typically larger than 30 µm). For zone plate condenser systems, the focal spot of the condenser optics is often used for specimen illumination, but for the described reasons, this is not useful for our system. The object was placed in the region where the beam radii converge to get an evenly illuminated object and zone plate. This was achieved by minimum distances of 75 mm between object and the second mirror. For the experiments described herein, a slightly larger distance of 85 mm was used to ensure complete illumination and to simplify the adjustment strategy.

Figure 5.18 illustrates the formation of an image in the microscope. The first positive order of diffraction magnifies an image of the object onto the CCD detector. As critical illumination could not be used in the setup, the object was placed behind the focal spot of the condenser

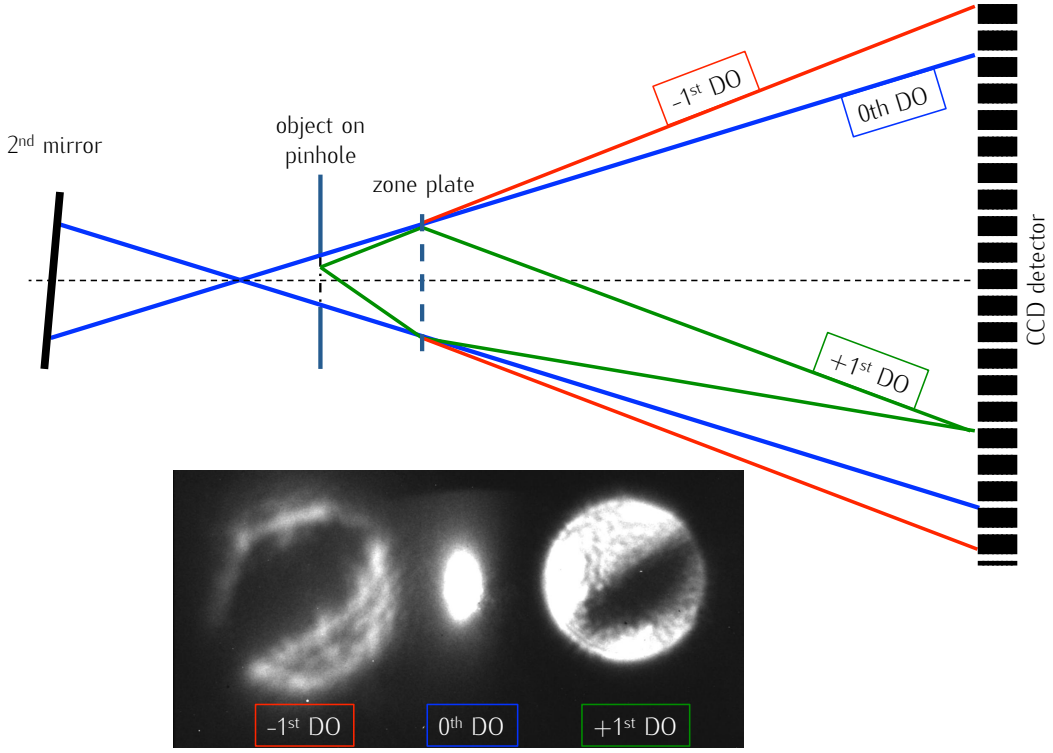

Figure 5.18: The magnified image of the object is formed by the $+1^{st}$ diffractive order. The 0^{th} and the -1^{st} order are also visible on the detector, if all components are placed on the optical axis and no critical illumination is used for the object. If the optical axis is left, the orders can be separated from each other.

system, so the object was illuminated by this point source. [29] As a result, light that reached the object in the e.g. upper right region mainly illuminated the upper right region of the zone plate afterwards. So, local variations of the diffraction efficiency could be visualized in the image through a deviation of image brightness. Together with the numerical apertures of the condenser and zone plate optics, this effect lead not only to the formation of an image by the $+1^{st}$ order of diffraction, but also by the -1^{st} DO. This image was slightly unsharp and central symmetric to the first image (see figure 5.18). If the zone plate or the object was moved from the optical axis, the -1^{st}, 0^{th} and $+1^{st}$ orders could be separated. The 0^{th} order acted as center of symmetry. By leaving the optical axis and separating the images, the 0^{th} and -1^{st} orders could be blocked by a central stop placed in front of the CCD chip. As a consequence, the zone plate was not fully illuminated any more, which made it necessary to optimize the conditions from image to image to obtain the best compromise in terms of background and image quality.

[29] Under critical illumination, the (larger) point source would be located within the object.

5.1.11 Resolution Limit

With the described microscope setup and the fabricated zone plates M52 and W2, images at $\lambda = 13\,\text{nm}$ were acquired to show the functioning of the zone plates and to judge the attainable resolution. Copper grids with or without supporting carbon film and silicon membranes were used as samples and sample holders for diatom skeletons. Diatoms are unicellular algae, which are commonly used in microscopy as their skeletons show regular structures that can be imaged with high contrast. For preparing the specimens, the skeletons were dispersed in water and dried on the grids.

For the used zone plate design with outermost zone structures of $\Delta r = 121\,\text{nm}$, the resolution limit by diffraction can be calculated to $R = 1.22 \cdot 121\,\text{nm} = 148\,\text{nm}$. The microscope was equipped with zone plate M52 for the first images shown in figure 5.19. The geometry of the setup was adjusted to a magnification of 414-fold, which corresponds to a distance between zone plate and CCD chip of $b = 374\,\text{mm}$. The focal length of the zone plate is $f = 900\,\mu\text{m}$ at $\lambda = 13\,\text{nm}$. Hence, the object distance, i.e. the distance between the zone plate and the object was 902 µm. The depth of focus, i.e. the interval in which the image resolution reaches its maximum value can be calculated to [Attwood, 2007]:

$$\text{DOF} = \pm\frac{1}{2}\frac{\lambda}{(\text{NA})^2} = \pm 2\frac{\Delta r^2}{\lambda} = \pm 2.25\,\mu\text{m}. \tag{5.11}$$

The CCD chip has an edge length of 26.8 mm, corresponding to 1340 pixels (20 µm pixel size) and was cooled to -50°C to minimize noise. For the images at 414-fold magnification, the effective sensor edge length was 64 µm at 48 nm effective pixel size. The object was mounted on a pinhole to minimize stray light. As the microscope could not be operated under critical illumination conditions and the numerical aperture of the condenser system was slightly smaller compared to that of the zone plate (0.038 vs. 0.053), complete illumination of the zone plate was ensured by pinholes with diameters >50 µm. Considering the divergence of the condenser and the mentioned pinhole, this ideally results in an illuminated disk with a diameter of 119 µm on the zone plate. Using pinholes of 60 and 100 µm diameter increases the disk diameter to 130 and 170 µm, respectively. As the vacuum gauges emitted visible light through their glowing filament, they were shut off during image acquisition to minimize background. Dark-field subtraction was performed for the images, whenever suitable.

Figure 5.19a shows an EUV image of a 2000 mesh[30] copper grid acquired at the specified imaging conditions. The upper right part of the image shows the central stop which blocks the 0th order of diffraction. Arrows mark bright spots at the opaque, and thus black, grid bars, originating from the -1st DO. As described before, this can be minimized by deviating from the ideal optical axis at the cost of only partial zone plate illumination. The resolution within the image was measured by the edge profile method, using the 10 to 90 % intensity rise. Averaging over five lines was performed using *ImageJ*, indicating a resolution of 339 nm. Reasons for this resolution value (that was lower as ideally expected) were found in the long exposure time of 45 min and vibrations of the microscope chambers and drift of the motorized stages. Additionally, focusing the image at these long exposure times was error prone due to low signal-to-noise ratios in the preview images that were acquired at shorter exposure times and binned CCD configuration. Another instability was found in the ethanol jet. Especially the capillary holder was prone to vibrations originating from the vacuum pumps. This changed the position of the plasma and thus of the light source. A more stable clamp for the capillary colder was designed and installed to optimize this. To ensure that the overall stability of the optical setup did not limit resolution, the backing pumps of the vacuum system were isolated from the vacuum chambers by intermediate pieces of rubber hoses and by vibration dampers. Additionally, weights of approximately 100 kg were added to the chambers to increase stability. Within the vacuum chambers, all optical components were tightly attached to the chamber walls.

Figure 5.19b shows an enlarged image of the 0th order of diffraction. In principle, the image is a transmission map of the zone plate and the substrate, magnified by the diverging light from the condenser. All areas that transmit light are visualized bright whereas all absorbing areas as well as areas that diffract light appear darker. The 0th DO is normally blocked by the central stop, but the image gives a qualitative view on the local diffraction efficiency of zone plate M52. The silicon nitride can be seen as grey box, slightly distorted as it is illuminated by the condenser in a region where the beam is still astigmatic. The drift ring in the center of the zone plate can be recognized as bright spot. From the center outwards, a first dark ring can be observed, which corresponds to the zones that have not been milled to leave space for the drift correction mark. The first bright ring can originate either from inner zones with relatively low diffraction efficiency, or from zones that are completely milled through the AuPd and also slightly through the silicon nitride. This would also lead to a higher signal in the 0th DO of these zones. The second option seems to be more likely, because it was observed during milling that the inner zones were always milled more deeply compared to the outer zones and because lower diffraction efficiency for the inner zones are not confirmed by the image shown in figure 5.21c. It depicts a regular image of a pinhole

[30]Mesh: unit to describe the number of grid periods per inch. 2000 mesh corresponds to 12.7 µm periodicity.

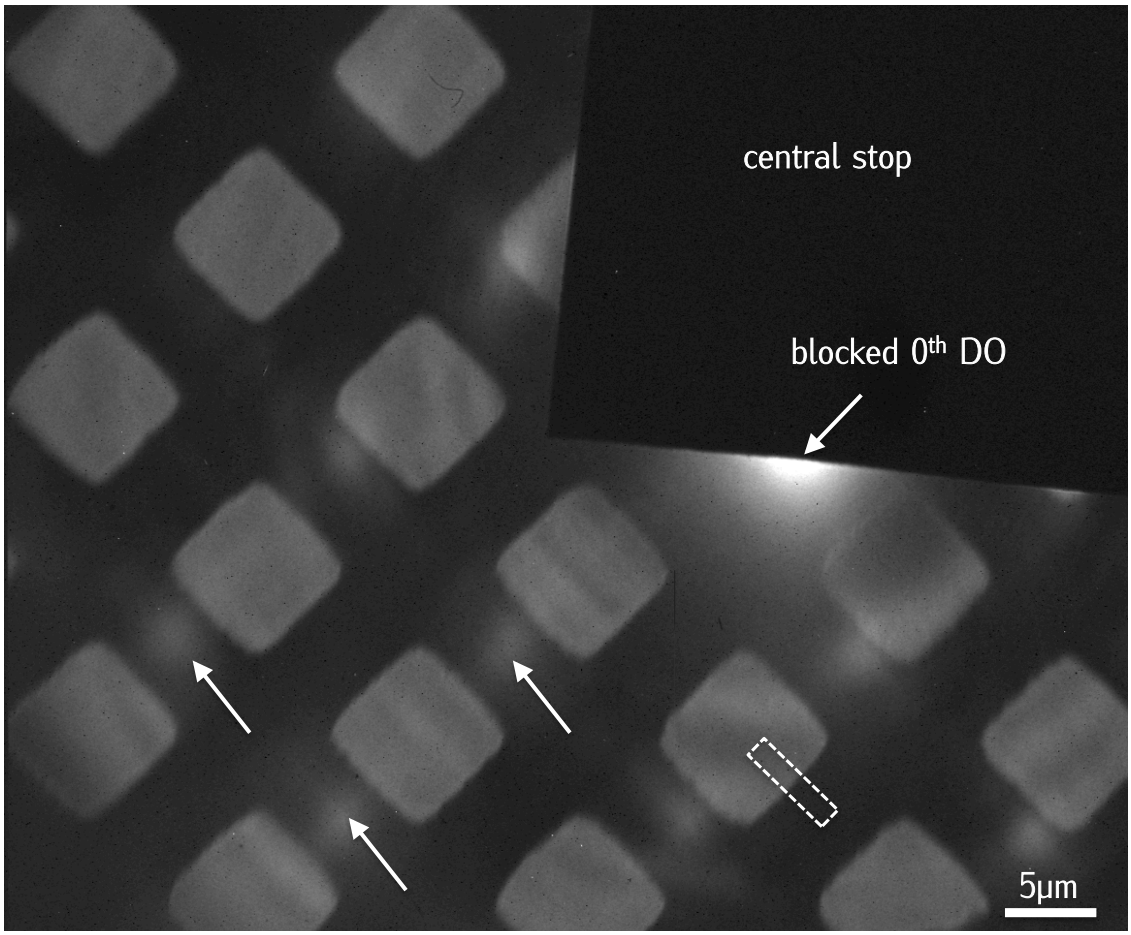

(a) Full field microscopic image of a 2000 mesh copper grid. A razor blade is used as central stop to block the 0^{th} order of diffraction. Arrows mark image artifacts originating from the image produced by the -1^{st} order of diffraction. Exposure time: 30 min. Magnification: 414x. IR-Laser pulse energy: 225 mJ.

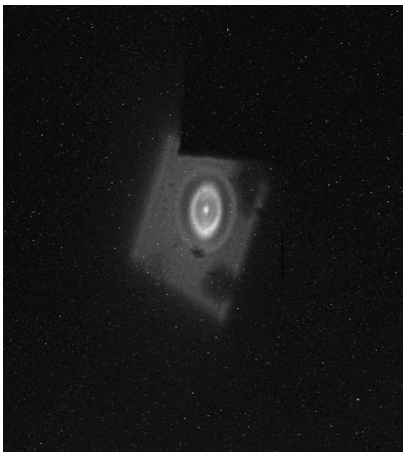

(b) 0^{th} order of diffraction (normally blocked by the central stop). Exposure time: 30 s. IR-Laser pulse energy: 250 mJ.

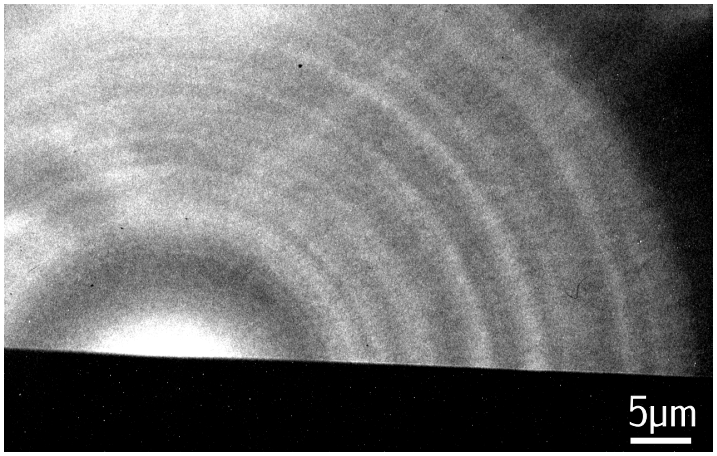

(c) Image background without object. Exposure time: 10 min. Magnification: 414x. IR-Laser pulse energy: 175 mJ.

Figure 5.19: Microscopic images acquired with zone plate M52 at $\lambda = 13$ nm.

with 110 µm diameter and no specimen mounted. As described before, the combination of condenser and zone plate allowed the visualization of local diffraction efficiencies relatively to the neighboring zones, as each region in the object plane was more likely to illuminate a certain region on the zone plate. The image shows the central stop in the bottom and an inner dark ring corresponding to the central zones that had not been milled. Adjacent to that, a series of brighter and darker rings are visible, showing slight deviations from the ideal zone position and thus deviations in diffraction efficiency.

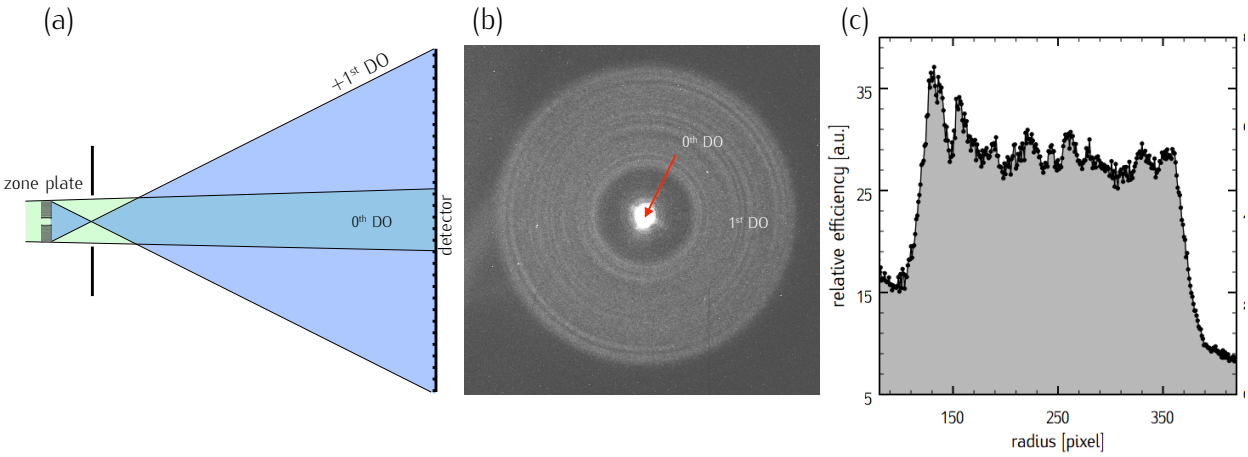

Figure 5.20: (a): Measurement principle of relative diffraction efficiency of zone plate M52. (b): The zone plate illuminated by the EUV beam and the first diffractive order is imaged on the CCD chip along with the 0^{th} order. (c): Radial averaging leads to a plot of the relative diffraction efficiency from the center of the zone plate outwards.

Figure 5.20a shows the principle of measuring local diffraction efficiency deviations that could lead to these ring artifact in the images. The zone plate was illuminated by the EUV light and the first diffractive order was imaged on the CCD chip which was placed in approximately 100 × f distance from the zone plate. By this, the 0^{th} and $+1^{st}$ diffractive orders were separated and could be imaged. The signal of the 0^{th} DO is much higher compared to that of diffracted light and has to be damped, if both orders have to be imaged at the same time. For the measurement, the zone plate was placed 137 mm from the detector and diffraction signals were acquired for 10 min (see figure 5.20b). To measure the incoming photon flux (compared to the first order flux), images without the zone plate were recorded using 15 s acquisition time. The diffraction pattern was scanned for its maximum value and radial averaging was applied to attain the relative diffraction efficiency. The plot in 5.20c shows the results and thus the deviations that lead to the imaging effects described earlier.

Only a slight decrease of the total diffraction efficiency towards the outer zones is observed, which indicates that the structure height and gap-to-period ratio is relatively constant over the entire zone plate. An estimation of absolute diffraction efficiency for zone plate M52 resulted in η_1=12.5 %, which lies within the expectations derived in section 5.1.1.

After refining the microscope setup in terms of stability and vibration, the images in figure 5.21 were acquired with zone plate M52. Images a, b and c show diatom skeletons on Si film, on Lacey carbon film (400 mesh copper grid) and on 2000 mesh copper grid. The setup now allowed exposure times of up to 45 min without signs of vibration and drift. To measure maximum resolution, the magnification was increased to 698-fold by increasing the distance from the object to the zone plate to 628 mm. By this, the effective pixel size was decreased to 28.7 nm.

Figure 5.21c shows diatoms on a 400 mesh Lacey carbon film. The image is exposed for 15 min and shows features sizes of 172 nm at a freestanding carbon bar. Feature sizes of 16 % above the resolution limit are observed, which indicates that the zone plate works in principle. Nevertheless, there is a loss in resolution that could have several reasons. The number of photons that arrive at the zone plate require exposure times of longer than 15 to 30 min to gather sufficient signal to noise ratio for imaging. During this time, instabilities, although minimized by constructive changes of the microscope setup, could reduce resolution. But also the zone placement accuracy could be a reason for resolution loss. However, the imaging resolution is near the ideal value, indicating the proper function of zone plate M52.

Zone plate W2 was tested under similar conditions in the EUV microscope. Compared to M52, the thicker AuPd layer acts as a complete absorber at $\lambda = 13$ nm which one the one hand limits the diffraction efficiency to $\eta = 10$ %, but on the other hand makes the zone plate more versatile to use at smaller wavelengths. Figure 5.22a shows an image of diatoms deposited on a 2000 mesh copper grid at 859-fold magnification and pixel binning of 2x2. Binning is a readout mode of the CCD chip at which the signal of more than one pixel is accumulated and jointly transferred to the readout amplifier. It lowers the read-out time and allows higher signal-to-noise values, as readout noise is added only once to the signal. More photons can be acquired at the cost of effective pixel size. In this case, the effective pixel size was enlarged from 23 nm edge length to 46 nm. This was sufficiently small to measure the attained resolution in the image as it was still under the *Nyquist* limit for the given setup.

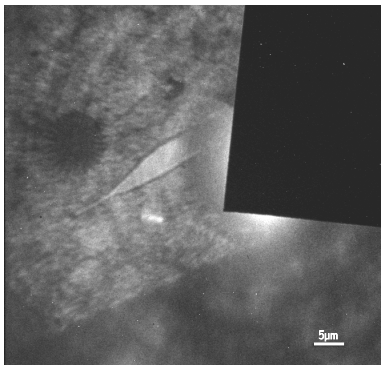

(a) Diatoms on 5 nm Si film. Exposure time: 5 min. Binning: 2x2. Magnification: 414x. IR-Laser pulse energy: 250 mJ.

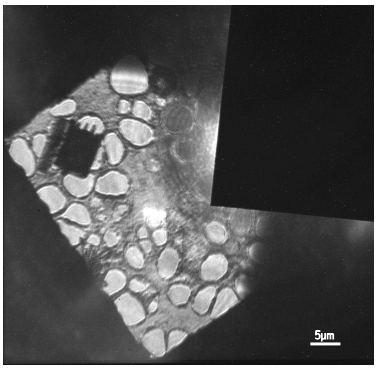

(b) Diatoms on 400 mesh Lacey carbon film. Exposure time: 45 min. Magnification: 414x. IR-Laser pulse energy: 250 mJ.

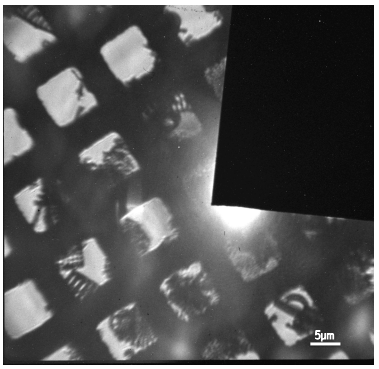

(c) Diatoms on 2000 mesh copper grid. Exposure time: 45 min. Magnification: 414x. IR-Laser pulse energy: 250 mJ.

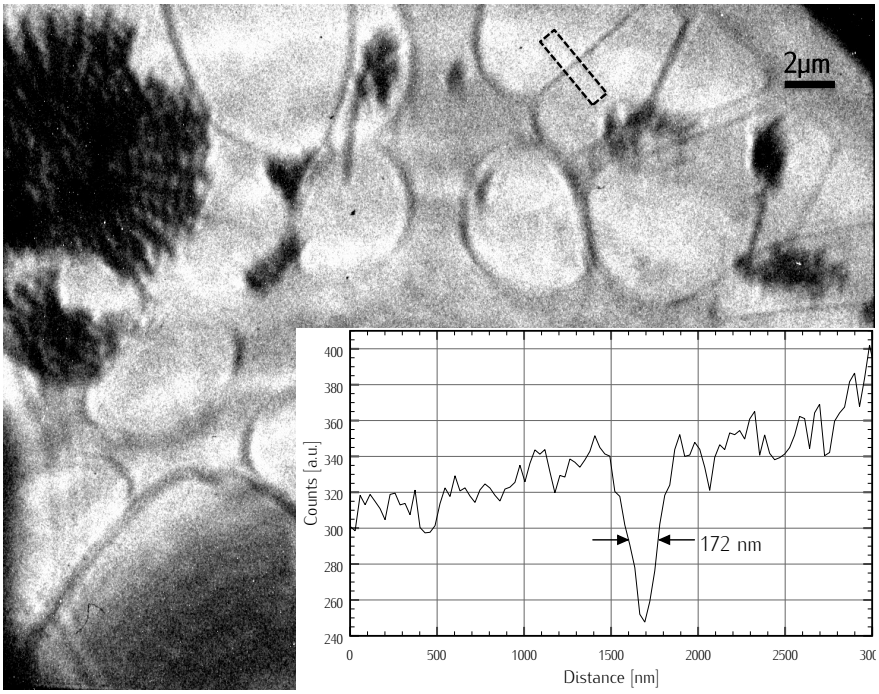

(d) Diatoms on 400 mesh Lacey carbon film. Exposure time: 15 min. Magnification: 698x. IR-Laser pulse energy: 250 mJ. Corresponding plot shows feature size of 172 nm (ImageJ, averaged over five lines).

Figure 5.21: Full field microscopic images acquired with zone plate M52 at $\lambda = 13$ nm.

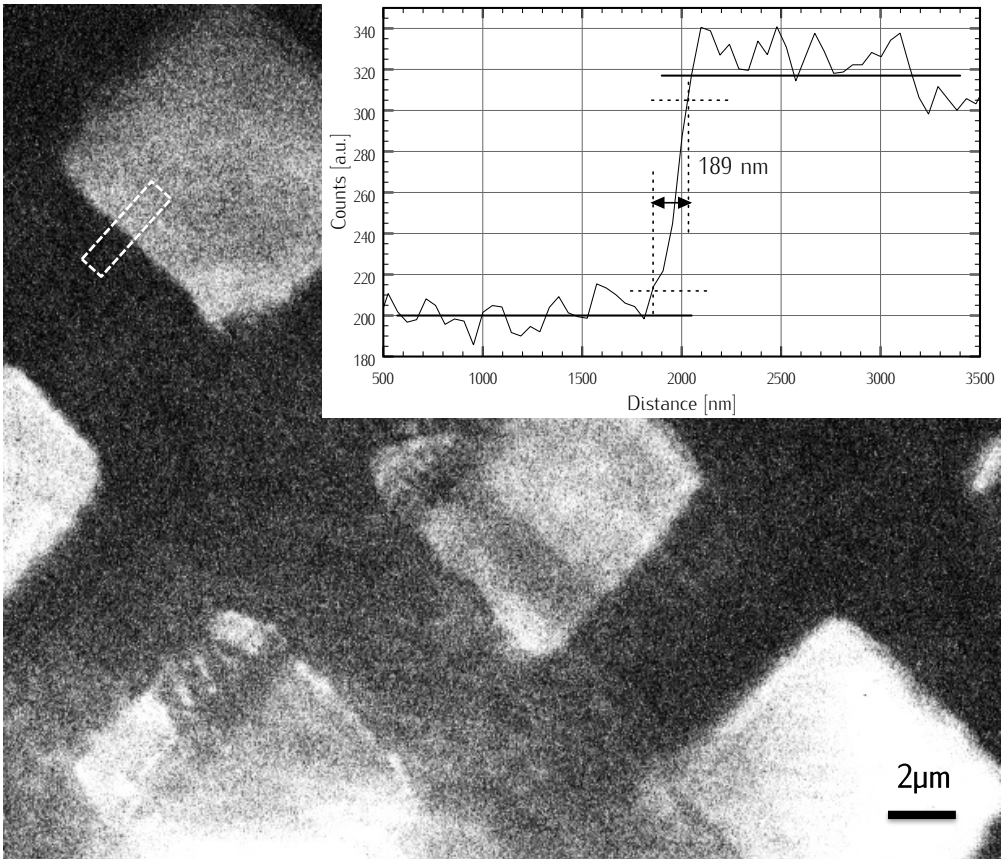

(a) Image acquired with zone plate W2 and corresponding plot showing edge profile (ImageJ, averaged over five lines). Exposure time: 30 min. Binning: 2x2.

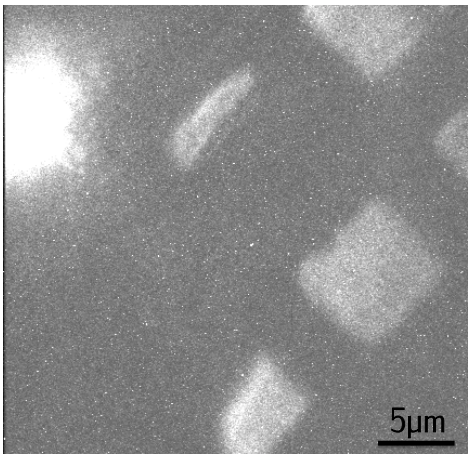

(b) Image acquired with zone plate W2. Exposure time: 10 min. IR-Laser pulse energy: 250 mJ. Binning: 3x3.

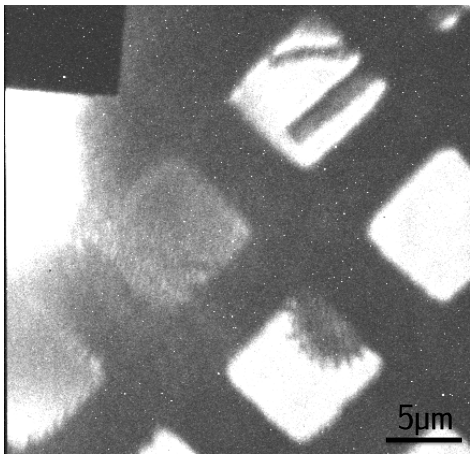

(c) Image acquired with zone plate M52. Exposure time: 10 min. IR-Laser pulse energy: 250 mJ. Binning: 3x3.

Figure 5.22: Full field microscopic images of diatoms on 2000 mesh copper grid acquired with zone plates W2 (a,b) and M52 (c) at $\lambda = 13$ nm. Magnification: 859x. Images (b) and (c) can directly be compared due to identical imaging conditions.

Measuring a 10 to 90 % edge profile in figure 5.22a confirms 189 nm imaging resolution for zone plate W2, slightly worse than the 172 nm for zone plate M52. The reason for this lies in the outer zone structures of the zone plate, which are mainly responsible for transferring the high spatial frequencies. As seen in figure 5.12e on page 75, the outer structures on zone plate W2 appear brighter compared to the inner zones. This means that the zones were not completely milled thorough the AuPd, which increases absorption and lowers resolution. Compared to zone plate M52, exposure times for W2 were higher by a factor of 3, which also means that diffraction efficiency is 1/3 of M52 and thus $\eta_1 \approx 4\,\%$.

5.2 Zone Plate Fabrication Raith ionLiNE

The zone plates M52 and W2 were fabricated on the *Zeiss XB1540*. The width of the outermost zone structures were limited by the stability of the FIB system and the characteristics of the ion beam. To overcome this, zone plates were fabricated on an FIB system optimized for lithography applications. In comparison to the *Zeiss XB1540*, a versatile laboratory tool for many applications, the *Raith ionLiNE* instrument is equipped with a laser interferometer controlled stage. The gallium column can be operated from 15 to 40 kV acceleration voltage at beam currents between 0.5 pA and 1 nA. Compared to the *Zeiss XB1540* system, longer exposure times can be realized because of the higher stability of the gallium ion source. As described before, no SEM functionality is built in, so imaging can solely be done by the ion-induced secondary electron signal. This chapter covers the fabrication of *Fresnel* zone plates with the *Raith ionLine* system and their application in a synchrotron-based X-ray microscope at $\lambda = 2.34$ nm.

To estimate the minimum outermost structure width that can be used during zone plate fabrication, linear diffraction gratings were milled (see figure 5.23). The structure of the freestanding gratings is similar to the ones described in chapter 4 [Lenz et al., 2009]. Compared to zone plates, the pattern was not only milled into the coating material, but completely through the substrate membrane. Hence, there is no loss due to absorption of photons in the substrate layer, which makes these freestanding gratins more efficient. The grating pattern was stabilized by 100 nm thick support stripes that run perpendicular to the grating period. Freestanding grating bars of 400 nm length showed sufficient stability during the fabrication process. The structures were milled into 100 nm silicon nitride membranes that had been coated with 25 nm of Cr for enhanced electric conductivity and thus to avoid charging effects during milling. An ion beam current of 7 pA was used for the experiments to attain highest

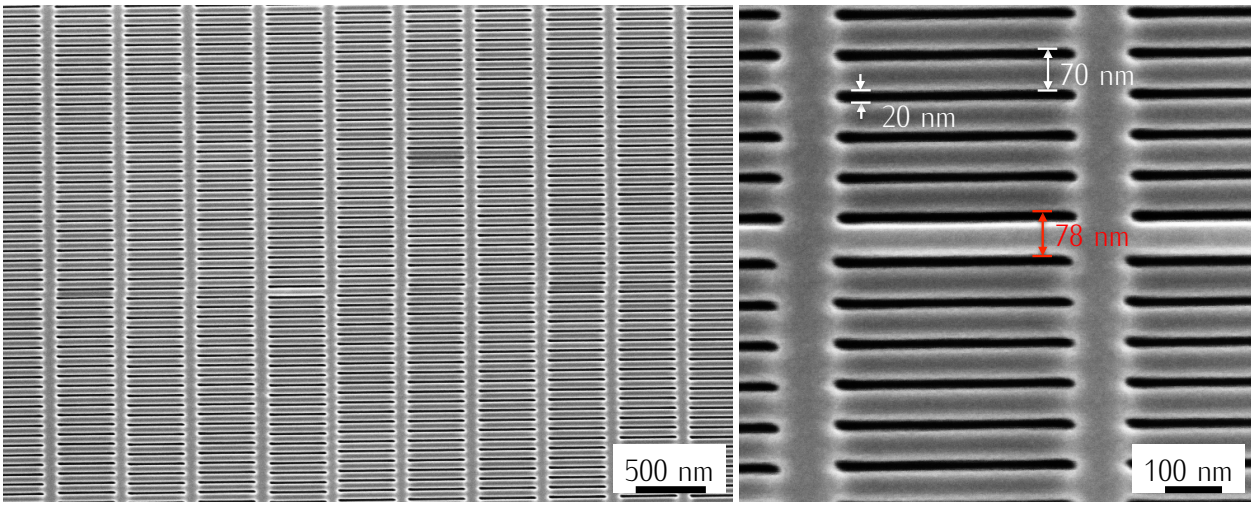

Figure 5.23: SEM image of freestanding diffraction grating with grating constant of g = 70 nm. Overall size of the grating is 25×63 µm^2. 900 grating periods. 100 nm support structure perpendicular to the grating. Length of the freestanding grating bars is 400 nm. Red arrow shows deviation of the grating constant by 8 nm due to ion source instabilities at the beginning of the milling process.

possible resolution. For the fabrication of zone plates, a trade-off between structure size and exposure time has to be made which makes the ion beam current larger for that kind of application. Nevertheless, by using such small beam currents for the resolution estimation, grating periods of 70 nm were fabricated. Figure 5.23 shows SEM images of the resulting grating. In total, 900 grating periods were milled, corresponding to 45.000 freestanding elements on an area of 25×63 µm^2. Total structuring time was 10.5 h. Due to ion source instabilities at the beginning of the milling procedure, one grating line was misplaced by 8 nm which would lead to a line doubling effect during use of the grating in a spectrograph. Nevertheless, the rest of the grating showed 20 nm gaps and 50 nm grating bar width, which leads to the estimation that zone plate fabrication with higher beam currents is possible for structure sizes slightly larger than 50 nm.

5.2.1 Material Choice

One of the biggest advantage of the IBL-based fabrication approach is the high degree of freedom for choosing suitable zone plate materials. For material changes in EBL-based processes, major parts of the fabrication process would have to be reshaped. For ion beam lithography, the only thing that has to be optimized is the applied ion dose to remove

the zone material down to the silicon nitride membrane. Even insulators could be milled if charging is avoided, e.g. by flooding the sample with negatively charged particles. To emphasize this extensive material choice, indium tin oxide (ITO) was used as zone material for the experiments. ITO is widely used in semiconductor industry, especially for LCD displays, as it is electrically conductive and at the same time translucent for visible light. It can be deposited by e-beam evaporation or sputter coating and forms continuous thin films.

Silicon frames (3 mm diameter) with 250 µm windows of Si_3N_4 (100 nm thickness) were used as zone plate substrates. On these substrates, 100 nm of ITO was coated by electron beam evaporation in an *UNAXIS BAK 640* coating device[31]. The vacuum chamber was pumped to a base pressure of $1.5 \cdot 10^{-7}$ mbar. During deposition, partial oxygen atmosphere of $2.0 \cdot 10^{-4}$ mbar was established at a deposition rate of 0.1 nm s^{-1}. The substrates were kept at room temperature to minimize enrichment of oxygen within the layers. To get accurate predictions for the diffraction efficiency of the zone plates, the material composition of indium, tin and oxygen had to be known and was therefore measured by *Auger* electron spectroscopy (AES). For this, the *Physical electronics PHI-AES 690* system utilizes *Auger* electrons ejected from the sample surface after electron bombardment. The kinetic energy of *Auger* electrons is element specific and can be used to gain quantitative information about the material composition. The atomic composition of the ITO layer determines the X-ray optical properties, and this can be measured by AES. The layer composition was measured as a mixture of 37% indium, 10% tin and 53% oxygen. For this distribution, first order diffraction efficiencies for zone plates with 100 nm ITO can be calculated to $\eta_1 = 11.0\%$ for $\lambda = 13$ nm and 2.3% for 2.34 nm [Schnopper et al., 1977].

5.2.2 Zone Plate Milling

A zone plate design with outermost zone structures of $\Delta r = 64$ nm and a diameter of 102 µm was calculated and milled into the 100 nm ITO coated substrate (zone plate AA03). This corresponds to 400 zones and focal lengths of $f = 2.8$ mm and 0.5 mm at $\lambda = 2.34$ nm and 13 nm, respectively. The resolution limit in full field imaging using the first diffractive order is 78 nm.

The zones were split up into three compartments containing the inner, the middle and the outer zones. These compartments were milled subsequently to each other. The gallium ion column was operated at 35 kV acceleration voltage and an ion beam current of 30 pA was

[31] Micro Systems Technology project group, research center caesar.

chosen as a trade-off between beam diameter and milling time. The zone plate was already mounted on a specially designed zone plate holder that was used during the IBL process as well as in the X-ray microscope. Figure 5.24 shows the design of the holder and a photograph of the same with a zone plate substrate mounted on it. The holder is equipped with an overhanging ring that protects the membrane from damage during handling and operation in FIB and X-ray microscope. Identical holders were used for zone plates M52 and W2 in the EUV microscope.

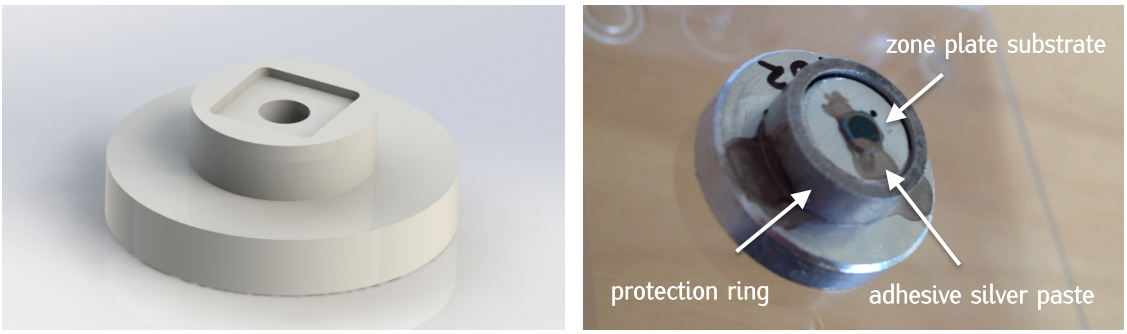

Figure 5.24: Zone plate holder design and photograph of the aluminium holder with a zone plate substrate mounted on it. A protection ring was glued onto the holder to prevent a damaging of the membrane. Adhesive silver paste was used to fix the zone plate and to ensure electric conduction during IBL milling.

The ideal dose for complete removal of the ITO layer was 16.0 mC/cm^2 for the inner zones. For zone widths smaller than 100 nm, the dose was gradually increased to 22.7 mC/cm^2 for the outermost zones to reach sufficient milling depth for the smaller structures. This dose was applied during 50 milling passes within approximately 10 h to remove the complete ITO layer, down to the silicon nitride membrane. Drift correction is performed in 200 µm distance from the zone plate, on the silicon frame of the zone plate substrate. As the instrument is equipped with a laser interferometer stage, the sample could be moved during the drift correction procedure without disturbing the process in terms of accuracy. 150 drift correction steps were applied during the fabrication. Drift pattern degradation due to sputtering during imaging was less problematic for a mark structure on the silicon frame, compared to a mark on the fragile membrane. The mark on the silicon frame could be milled much deeper as one was not dependent on imaging contrast between zone material and silicon nitride. Therefore, the mark was milled several hundred nanometers into the silicon and imaging contrast was gained from this topographic difference, rather than from material

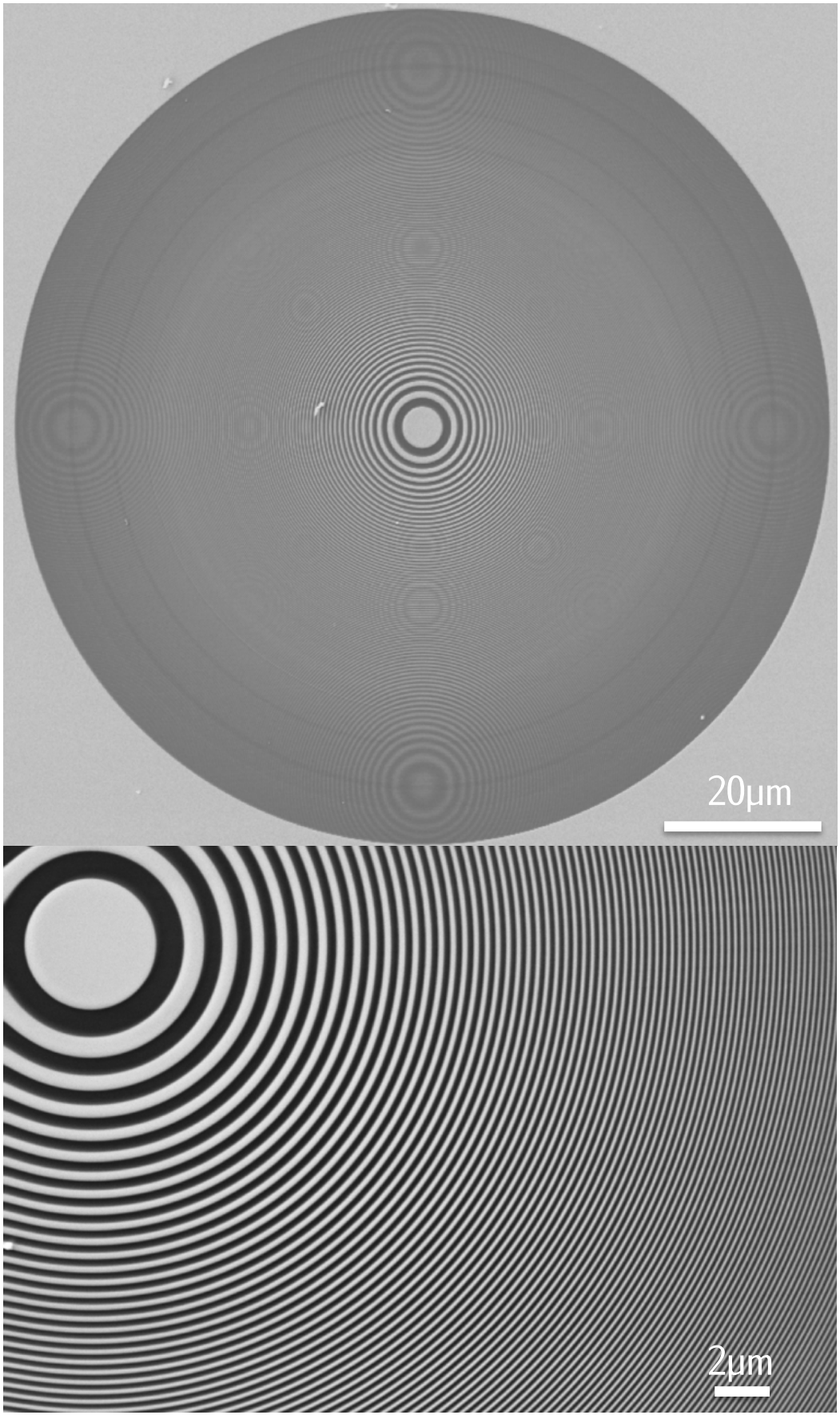

Figure 5.25: Zone plate AA03 on silicon nitride membrane. The outermost zone width is $\Delta r = 64\,nm$ at a zones height of 100 nm. Zone material is indium tin oxide (ITO).

difference. This reduced pattern degradation as the structures were extremely durable under ion beam influence.

Figure 5.25 shows SEM images of zone pate AA03. The high contrast between ITO (bright) and silicon nitride (dark) indicates that the zone structures are completely milled though the ITO. Zone placement accuracy was sufficiently high and over-all, the zone plate is very regular. In the outer region of the zone plate, faint dark rings can be observed at the radii where the dose was increased. It is unclear whether this effect originates from the changes in redeposition behavior in the regions of the dose change or if it is an SEM imaging artifact because of the asymmetry of the zones, induced by milling one two adjacent zones with different dose values.

5.2.3 Soft X-Ray Microscopy

Zone plate AA03 was tested in full field soft X-ray imaging at the synchrotron *PETRA III* at *DESY* in Hamburg. Originally commissioned for collider experiments in 1978, it was constructively re-designed to an X-ray emitting 6 GeV electron storage ring in 2009. The ring is 2.3 km long in total, but only a small fraction of the circumference is equipped with insertion devices that are used as light sources. 14 experimental stations are installed for different scientific applications. From the end of 2013 to 2015, user operation at the storage ring is stopped to install additional beamlines. The described experiment was carried out at the undulator beamline P04, the »Variable Polarization XUV« beamline. Table 5.7 summarizes its most important specifications. During the experiment, the storage ring was operated at 6.084 GeV energy and 95.28 mA beam current within 960 electron bunches. The photon energy at P04 was set to 530 eV, which corresponds to a wavelength of $\lambda = 2.34$ nm.

Table 5.7: Design specifications for the »Variable Polarization XUV« beamline P04 at *PETRA III* (*DESY*, Hamburg). Values from [Viefhaus et al., 2013].

undulator	72 periods of 65.6 mm, 10 kW max. power
energy range	250 eV – 3000 eV
photon flux	$> 10^{12}$ photons/s
resolving power (spectrally)	$> 10^{4}$

A soft X-ray microscope was constructed at P04 using a flexible environment, containing vacuum chambers and motorized positioning systems.[32] This modular environment was developed as an base for a broad range of imaging experiments at *PETRA III* and *FLASH*[33]. It utilizes up to three separated vacuum chambers, each equipped with a rail-guide system for up to five piezo motor stages. The stages offer 3-axis movement and optical encoders with custom designed closed-loop controllers. Travel ranges of 50 mm are possible with nm-precision at speeds up to 10 mm/s. As an example, the setup was used for imaging the magnetic orientation of nanostructured materials by X-ray magnetic circular dichroism (XMCD) contrast [Wessels et al., 2013].

Figure 5.26 shows the experimental setup. The cylindrically-shaped vacuum chamber contained the optical components of the microscope (shutter, condenser, object and zone plate). A glass flange at the side of the chamber (see figure 5.26a) allowed easy access to the components and gave optical feedback of the stage movement. It was covered with opaque fabric during image acquisition. A thinned CCD camera of type *Andor iKon-M* was used. Its CCD chip was cooled to -60°C and has 1024×1024 pixels of 13 µm edge length. It was set to a readout frequency of 1 MHz and was separately pumped to reduce contamination of the chip.

In the soft X-ray microscope, a segmented grating condenser was used to homogeneously illuminate the object. As shown in figure 2.13 on page 29, this type of condenser can be used at undulator beamlines to overcome problems originating from too high spatial coherence [Vogt et al., 2006]. The condenser was fabricated by electron beam lithography by *ZonePlates Ltd.*[34] It has $20 \times 20\,\mu m^2$ grating segments, distributed over 1 mm diameter and features an in-built central stop made of gold. The outermost structures show 50 nm structure size, which leads to a focal length of $f = 21.4$ mm at $\lambda = 2.34$ nm. The object was placed in the focal spot of the condenser and zone plate AA03 was used as lens. The imaging width, i.e. the distance between the zone plate and the CCD chip was adjusted to $b = 1700$ mm. This is large compared to the focal length of the zone plate of $f = 2.8$ mm. According to the imaging equation, this leads to an object distance of

$$g = \frac{1}{f^{-1} - b^{-1}} = 2.805 \simeq f$$

and a magnification of

$$V = \frac{b}{g} = 606x.$$

[32] Development within the BMBF project NanoFLASH at the »Institute for X-Optics« at RheinAhrCampus Remagen.

[33] FLASH: Free-Electron Laser in Hamburg

[34] ZonePlates Ltd, Claverings Industrial Estate, London, UK

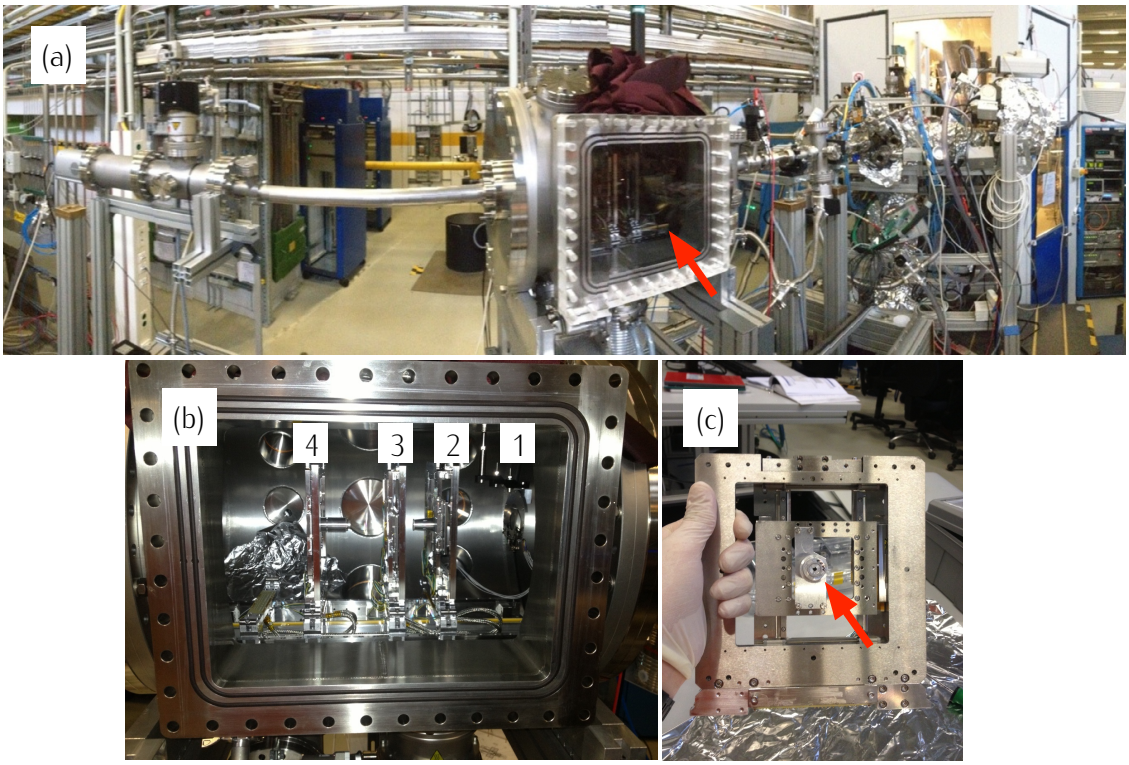

Figure 5.26: Microscopy setup at *PETRA III*, beamline P04. (a): Experimental setup. Beam direction from the right to the left. Arrow marks the microscopy chamber which is connected to the separately pumped CCD camera by a beam tube. (b): Detailed view of the microscope chamber with shutter (1) and motorized holders for the condenser (2), the object (3) and the zone plate (4). (c): Motorized zone plate holder with zone plate (red arrow) mounted on it.

For this magnification, the effective pixel size of the CCD chip was 21.4 nm at a field of view of 21.9 µm.

Copper grids and a *Siemens* star were used as test samples to judge the attainable resolution of zone plate AA03. Figure 5.27a shows a full field X-ray microscopic image of a 2000 mesh copper grid. The image was acquired within 20 s exposure time, which was an improvement by a factor of 100, compared to typical exposure times at the laser-induced plasma source. In the center of the image, a bright spot can be identified. It cannot be distinguished whether this is light of $\lambda = 2.34$ nm that was not blocked by the central stop of the condenser, or if it is a higher order wavelength of the undulator. As these higher orders have smaller wavelengths compared to the fundamental mode, the central stop shows higher transmission for it. Figure 5.27b shows the corresponding knife-edge plot extracted from the image. At the edge of the copper grid, 89 nm resolution can be measured. Compared to the ideal resolution of the zone plate of 78 nm, this is 14% less than possible, but well within the

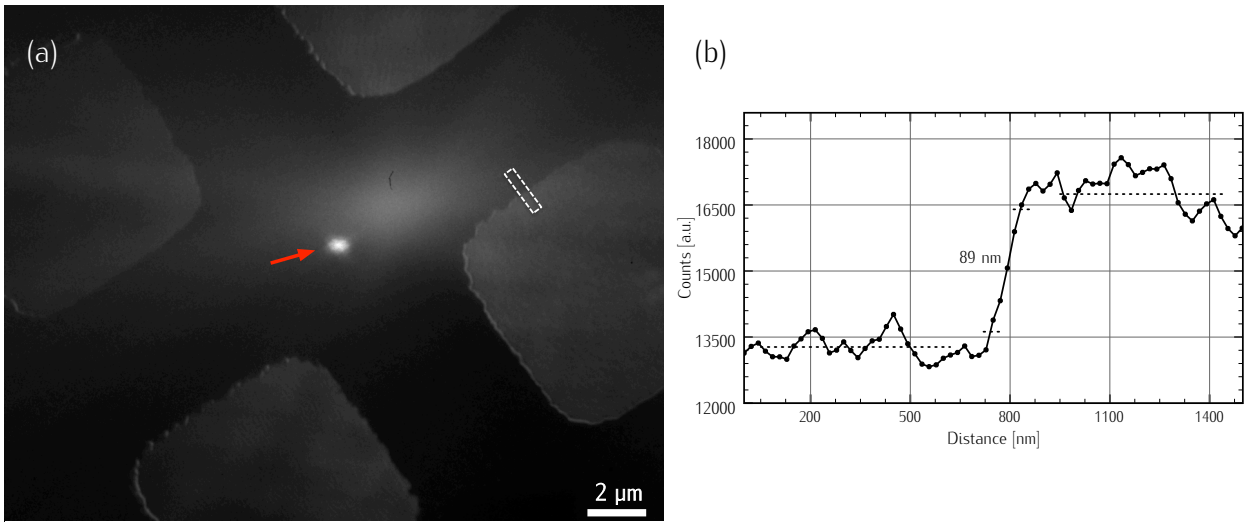

Figure 5.27: (a) Full field microscopic image of 2000 mesh copper grid acquired with zone plate AA03 at $\lambda = 2.34$ nm. Exposure time: 20 s. Magnification: 606x. Red arrow indicates bright spot originating from light that passed the central stop of the condenser. (b) Corresponding edge profile shows resolution of 89 nm.

expectations.

The second resolution test sample was a *Siemens* star (figure 5.28). It consists of spokes that originate from a common center and increase in size with increasing distance from this center. The pattern with 60 µm diameter was fabricated by electron beam lithography on a 30 nm thin silicon nitride membrane[35]. During the process, PMMA[36]-resist was exposed to an electron dose of 400 µC/µm^2 at 20 kV acceleration voltage and 300 pA beam current. The developed resist structure was coated with 2 nm Cr and 25 nm Au, before an acetone-based lift-off step finished the nanostructuring. Figures 5.28a and b show SEM images of the pattern. The periodic structures are intact upon 100 nm feature size. Smaller structures are degraded but an isolated feature of 83 nm size is visible in the center of the structure. Figure 5.28c and d show full field X-ray microscopic images of the *Siemens* star sample. Again, a magnification of 606-fold is used. To attain better signal-to-noise ratio, 10 images of 10 s exposure time each were averaged. Image processing was performed by dark-field subtraction and flat-field correction. Flat-field correction was necessary to correct for inhomogeneous background due to the condenser optics. Although beam wobbling was applied to the last optical element of the beamline (PM/PG-U), the high degree of spatial coherence lead to the imaging background shown in figure 5.28e. The sub-elements of the segmented grating condenser were visible within the background. Upon comparison of

[35] Lithography process conducted by F. von Cube and T. Weber (Nanophotonics Group, University Bonn)
[36] PMMA: Poly(methyl methacrylate)

images 5.28b and d, it can be concluded that imaging resolution is at least 83 nm. The individual gold feature (red arrow) can clearly be distinguished from the background. Overall, imaging contrast was extremely well and no zone plate-related image distortion could be observed.

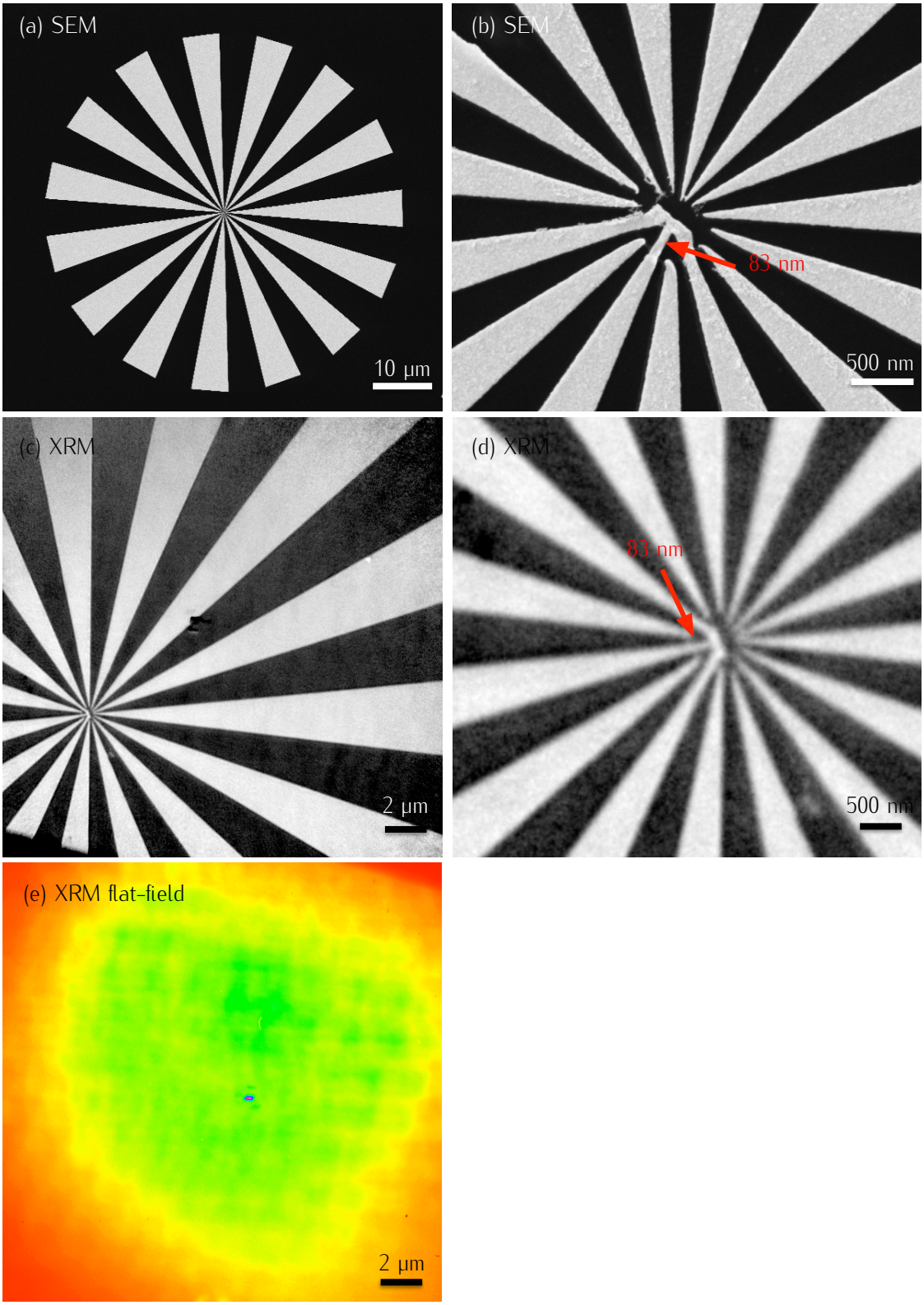

Figure 5.28: (a,b): SEM images of a *Siemens* star, 60 µm in diameter, fabricated by electron beam lithography on a 30 nm silicon nitride membrane. 25 nm gold and 2 nm Cr are used as material. Red arrow marks feature of 83 nm diameter. (c,d): Corresponding full field X-ray microscopic images acquired with zone plate AA03 at $\lambda = 2.34$ nm. Exposure time: 100 s. Magnification: 606x. XRM images are inverted to match the contrast of the SEM images. (e) Flat-field correction image used to correct image (c).

6 Summary and Discussion

This thesis describes the development of an alternative fabrication approach for *Fresnel* zone plates and their application as lenses in EUV and SXR microscopes. The developed process is based on the selective removal of matter by focused gallium ions. Substrate atoms are ejected from the surface by transfer of momentum, which leads to a change of the topography. By this, the individual zones of a zone plate are directly defined into metal-coated, X-ray transparent substrates. At the moment, electron beam lithography is the most commonly used fabrication method for *Fresnel* zone plates. In EBL, the exposed resist structures have to be transferred to the actual zone plate structures by several etching and plating steps. The IBL-based method described herein combines exposure and pattern transfer in one single step. However, the exposure step within the FIB system is long compared to EBL. Drift correction strategies have to be applied to keep the position of the ion beam, with respect to the sample, stable during the fabrication time of several hours. Although, the number of individual steps necessary to get from the zone plate substrate to the finished zone plate is much smaller.

Two FIB systems were used for the work described herein: The *Zeiss XB1540* system is a standard laboratory tool, which is routinely used for non-lithographic tasks like cryo TEM lamellae fabrication or cross-section cutting. To use it as an IBL tool, a lithographic attachment was installed (*Raith Elphy Plus*). This attachment controls the beam deflection system of the ion column and allows more complex writing procedures and a larger write field compared to the standard configuration. The second FIB instrument used was the *Raith ionLiNE* IBL system. It is optimized for lithographic applications in terms of ion beam size and overall stability.

The fabricated zone plates were applied as lenses in X-ray microscopic setups at EUV and SXR wavelengths to judge the proper function and the attainable resolution. An EUV microscope based on a laser-induced plasma source was constructed for the zone plates fabricated with the *Zeiss XB1540* system. An X-ray microscope operated at SXR wavelengths was constructed at the *PETRA III* electron storage ring for the zone plates that were structured with the *Raith ionLiNE* system.

6.1 Zone Plates M52 & W2

Zone plates M52 and W2 were fabricated on AuPd-coated silicon nitride membranes with the *Zeiss XB1540* system. First resolution estimations showed the potential of fabricating structure sizes of approximately 100 nm for zone plate diameters of 100 µm and less within reasonable structuring time. Ion beam currents of smaller 100 pA were chosen for the fabrication, as this allowed the removal of up to 300 nm thick layers of AuPd within 3.5 to 8.5 h. Two thicknesses of gold palladium coatings (100 & 300 nm) were chosen because these zone heights show the characteristics of phase and amplitude zone plates for $\lambda = 13$ nm wavelength. The metal layers were deposited onto the samples by magnetron sputtering in a *Baltec MED-020* sputter coater. Heating of the substrates showed crystalline structures with grain sizes >100 nm, which did not allow IBL structuring. Thus, the following depositions were performed at room temperature, deposition rates of 0.22 nm/s, which led to sufficiently smooth and flat surface characteristics. The smoothness and the crystalline structure of the substrate are especially important for IBL-based processes as they influence the sputter yield for incident gallium ions. Rough surfaces lead to inhomogeneous zones and therefore to lowered diffraction efficiencies. Crystalline structures lead to a local variation of the sputter yield within the write field and thus to locally differing zone heights of the zone plate.

During the zone plate fabrication process, the position of the ion beam relative to the substrate has to be kept stable within one third of an outermost zone width [Michette, 1986]. If this is not the case, the interference condition for forming a diffraction limited focal spot is not valid anymore. To ensure proper function of the zone plate, a drift correction procedure was developed. It is based on acquiring ion-induced secondary electron images of a mark pattern. This is done regularly during the fabrication process. Images of these marker structure are acquired and compared to a reference image. Shift values between the images are calculated and applied to the beam, which restores its original position. As every image scan degrades the imaging mark and thus makes comparison to a reference mark more difficult, a robust mark geometry is needed. Additionally, every scan mills the structure one step deeper into the underlying silicon nitride, making the membrane more fragile. Evaluating different mark geometries by their auto-correlation function resulted in the use of ring-shaped marks with 5 µm diameter. The stability of the ring markers was investigated for a maximum of 150 image scans, showing that approximately 100 scans can be acquired before pattern degradation decreases the cross-correlation signal. Compared to cross-shaped markers, degradation of the ring structures occurs in a symmetric way, which is favorable for the drift correction algorithm. The accuracy of the correction strategy was

measured with *Vernier* patterns. Different image acquisition parameters were investigated. Mean drift correction errors of $(\bar{x},\ \bar{y}) = (14\,\text{nm},\ 12\,\text{nm})$ were measured for the setting with the best trade-off between signal-to-noise ratio in the images and imaging dose. This fits well to the resolution limit of the microscope and makes zone plates with outermost zone widths of $\Delta r \approx 100\,\text{nm}$ feasible with the *Zeiss XB1540* FIB system. With the developed process, zone plates M52 and W2 with $\Delta r = 121\,\text{nm}$ were structured with ion dose values of 26 and $62\,\text{mC/cm}^2$, respectively. Ion beam currents of 74 pA (M52) and 53 pA (W2) were used and fabrication times were 3.5 h (M52) and 8.5 h (W2). Zone placement accuracy was sufficiently high for $\Delta r = 121\,\text{nm}$ and the drift correction algorithm worked stable during the fabrication time. The achieved structure size shows the inherent limit of the *Zeiss XB1540* FIB system for this type of task. More specific, the ion column does not allow stable and reproducible zone plate fabrication for structuring times $>10\,\text{h}$. To remove a sufficient amount of matter within a $100 \times 100\,\mu\text{m}^2$ write field, ion beam currents between 50 and 80 pA have to be used. As mentioned, these currents allow the fabrication of structures sized $\approx 100\,\text{nm}$, which limits the process in terms of resolution.

General problems during structuring arose from stress within the compound of AuPd and silicon nitride. If the applied dose had been slightly higher than needed, so that the ion beam milled through the silicon nitride layer, the membrane broke immediately. If too little dose was applied, the remaining AuPd layer acted as additional absorbing layer and lowered diffraction efficiency significantly. Precise dose control is therefor necessary for the IBL based fabrication of zone plates.

For the first time, full field imaging with IBL-fabricated zone plates (M52 and W2) was demonstrated with the constructed EUV microscope [Overbuschmann et al., 2012]. Based on an ethanol-jet, the laser-induced plasma source delivered approximately 10^{10} photons/s within the $\lambda = 12.99\,\text{nm}$ oxygen line ($1s^2 2p\text{-}1s^2 4d$), from which 10^5 photons/s were collected by the multi layer condenser system. The microscope could be operated at magnifications between $V = 700$ and 900x with exposure times of several minutes.

Images of diatom samples on different copper grids were acquired with the two zone plates. Image contrast was well-defined for the images and resolution values of 172 nm and 189 nm were measured for the zone plates M52 and W2, respectively. Compared to the ideal (diffraction limited) imaging resolution of 148 nm, this is 16% to 28% above the theoretical limit. Reasons for this are the long image exposure times in the EUV microscope of 15 to 45 min, as well as drifts and vibrations of the optic mounts during this time. The zone placement accuracy and therefore the accuracy of the drift correction strategy is a further reason for the deviation of the resolution from the ideal value. The image background for

both zone plates showed brighter and darker rings, originating from differing local diffraction efficiencies over the zone plate. These deviations, which originate from local zone placement errors, are visible because of the special illumination conditions of the condenser within the EUV microscope. The diffraction efficiency of zone plate M52 lies within the theoretical expectations. For zone plate W2, which had longer fabrication time and higher zones, a diffraction efficiency of 4% is estimated upon comparison to zone plate M52. The outer zones of W2 are not completely milled through the AuPd layer, leading to this decrease in efficiency.

Summarizing the experiments with the *Zeiss XB1540* FIB system, it was shown that zone plate fabrication by means of ion beam lithography is a suitable alternative to the existing methods. The resolution of EBL-based techniques is not reached because of the technological limitations of the used FIB system. It is a laboratory tool that is not optimized for the long exposure times at the level of accuracy needed for zone plate fabrication. However, the application of the fabricated zone plates in full field EUV microcopy was shown for the first time. To increase resolution, the *Raith ionLine* IBL system was used for patterning zone plates.

6.2 Zone Plate AA03

To obtain structure sizes <100 nm, zone plate AA03 was fabricated with a *Raith ionLine* IBL system. Preparatory experiments with diffraction grating patterns showed freestanding grating constants of 70 nm. This demonstrates what ion beam lithography can be capable of in terms of optics fabrication for X-ray applications. Fabricating freestanding structures by means of EBL is extremely challenging due to tensions in the substrate material and the number of structuring steps needed [Rehbein, 2001]. The IBL resolution tests showed structure sizes of 50 nm with 20 nm gaps in one single fabrication step. For the fabrication of zone plates, the achievable resolution is lower because of two reasons: Firstly, higher beam currents have to be used to achieve reasonable structuring times. Secondly, freestanding structures allow sputtered atoms to leave the milling site in reverse direction of the incident ion beam, as well as in the flight direction. This allows higher aspect ratios and lowers milling time for freestanding structures. Experiments to fabricate freestanding zone plates by this approach were conducted, but are not described within this thesis.

To show that IBL is capable of fabricating zone plates with any zone material, a mixture of indium oxide and tin oxide (ITO) was chosen for zone plate AA03. ITO has never been used as

zone plate material before; it shows excellent surface characteristics and is widely available. Layers of 100 nm ITO were deposited onto silicon nitride membranes by e-beam evaporation on an *UNAXIS BAK 640* coater. The ratio of In to Sn was measured by *Auger* electron spectroscopy to be 3.7 to 1. For such a composition and 100 nm zone height, diffraction efficiencies of 2.3% and 11% were calculated for $\lambda = 13$ nm and 2.3 nm, respectively.

Zone plates with outermost zone widths of $\Delta r = 64$ nm were successfully fabricated with a gallium ion dose value of 16 mC/cm^2. As for zone plate W2, the dose was increased towards the outer zones (to 23 mC/cm^2) to compensate for redeposition effects that occur at the smaller structures. The drift mark, which was regularly imaged for drift correction (150 times in total) was placed off the membrane, as the accuracy of the interferometer-controlled stage allowed to do so. Imaging this mark is not limited by the thickness of the membrane any more. Compared to zone plates M52 and W2, for which the marks had to be on the membrane, its position on the silicon frame allowed to fabricate the mark much deeper. This made the drift correction more stable. The zone plate was structured with a total exposure time of 10 h. For zone plate AA03, 50 milling passes were used instead of <10 for M52 and W2. This increases the smoothness of the zone structures.

Zone plate AA03 was applied in a full field soft X-ray microscope that was constructed at the electron storage ring *PETRA III* at *DESY* in Hamburg. A multi-purpose experimental framework was used. It was equipped with a rail-mount system for holding the optical elements. Piezo motor-driven stages allowed the manipulation of the geometry inside the vacuum chambers. A segmented grating condenser was used to collect the synchrotron light beam at $\lambda = 2.34$ nm. An EBL-fabricated *Siemens* star and copper grids were used as test samples, showing excellent imaging characteristics. The functioning of the zone plate was confirmed with an imaging resolution of 83 nm. The images acquired with AA03 have much shorter exposure times compared to M52 and W2 due to the higher photon flux of the synchrotron beam compared to the laser plasma source. Additionally, AA03 showed no zone plate-related imaging artifacts like e.g. local deviations of diffraction efficiencies that had been observed for zone plates M52 and W2.

Summarizing the results, zone plate AA03 shows the smallest outermost zone structures with $\Delta r = 64$ nm. The standard EBL-fabricated zone plates that are routinely used in full field X-ray microscopy at synchrotron radiation facilities have outermost structure sizes of $\Delta r = 25$ to 50 nm. The shown ITO zone plate almost reaches this level of resolution with a material that has not been used for zone plate fabrication up to now. With the already achieved freestanding grating structures of 50 nm grating bars and 20 nm gap width, it can be reasonably expected to reach EBL-like structure sizes also for IBL-based zone plate

fabrication in the near future. So, IBL shows promising prospects in the future development, especially regarding applications for which a specific material is more important than attaining highest possible resolution.

It was demonstrated that optics fabrication based on ion beam lithography is a suitable alternative to electron beam lithography. In the next years, technological improvements will further increase stability and resolution of ion beam columns. Methodical development in X-ray optics fabrication will benefit from this and ion beam lithography will become more widely used due to its advantages regarding process simplicity and material choice.

Bibliography

[Attwood, 2007] Attwood, D. (2007). *Soft X-Rays and Extreme Ultraviolet Radiation: Principles and Applications*. Cambridge University Press.

[Baez, 1952a] Baez, A. V. (1952a). Resolving power in diffraction microscopy with special reference to x-rays. *Nature*, 169(4310):963–964.

[Baez, 1952b] Baez, A. V. (1952b). A study in diffraction microscopy with special reference to x-rays. *Journal of the Optical Society of America*, 42(10):756–756.

[Bal-Tec AG, 2000] Bal-Tec AG (2000). Coating technique for electron microscopy. *Application Note*.

[Benk et al., 2008] Benk, M., Bergmann, K., Schäfer, D., and Wilhein, T. (2008). Compact soft x-ray microscope using a gas-discharge light source. *Optics Letters*, 33(20):2359–2361.

[Berglund et al., 1998] Berglund, M., Rymell, L., Hertz, H. M., and Wilhein, T. (1998). Cryogenic liquid-jet target for debris-free laser-plasma soft x-ray generation. *Review of Scientific Instruments*, 69(6):2361–2364.

[Bertilson et al., 2009] Bertilson, M., von Hofsten, O., Vogt, U., Holmberg, A., and Hertz, H. M. (2009). High-resolution computed tomography with a compact soft x-ray microscope. *Optics Express*, 17(13):11057–11065.

[Bertilson et al., 2007] Bertilson, M. C., Takman, P. A. C., Holmberg, A., Vogt, U., and Hertz, H. M. (2007). Laboratory arrangement for soft x-ray zone plate efficiency measurements. *Review of Scientific Instruments*, 78(2):026103.

[Born and Wolf, 1999] Born, M. and Wolf, E. (1999). *Principles of Optics: Electromagnetic Theory of Propagation, Interference and Diffraction of Light*. Cambridge University Press, 7th edition.

[Bunshah, 1994] Bunshah, R. (1994). *Handbook of Deposition Technologies for Films and*

Coatings: Science, Technology, and Applications. Materials science and process technology series. Noyes Publications.

[Carl Zeiss Microscopy, 2008] Carl Zeiss Microscopy (2008). Introducing the LEO 1560XB CrossBeam FESEM and FIB Workstation. Technical explanation of the Focused Ion Beam and the CrossBeam concept. Presentation Slides.

[Carl Zeiss Microscopy GmbH, 2003] Carl Zeiss Microscopy GmbH (2003). *Technical specifications LEO 1540XB*.

[Chao et al., 2012] Chao, W., Fischer, P., Tyliszczak, T., Rekawa, S., Anderson, E., and Naulleau, P. (2012). Real space soft x-ray imaging at 10 nm spatial resolution. *Optics Express*, 20(9):9777–9783.

[Chao et al., 2005] Chao, W., Harteneck, B. D., Liddle, J. A., Anderson, E. H., and Attwood, D. T. (2005). Soft x-ray microscopy at a spatial resolution better than 15 nm. *Nature*, 435(7046):1210–1213.

[Chao et al., 2009] Chao, W., Kim, J., Rekawa, S., Fischer, P., and Anderson, E. H. (2009). Demonstration of 12 nm resolution Fresnel zone plate lens based soft x-ray microscopy. *Optics Express*, 17(20):17669–77.

[Chapman, 1980] Chapman, B. N. (1980). *Glow discharge processes : sputtering and plasma etching*. Wiley New York.

[Coherent Inc., 1998] Coherent Inc. (1998). Infinity operators manual.

[Fiedorowicz et al., 1999] Fiedorowicz, H., Bartnik, A., Szczurek, M., Daido, H., Sakaya, N., Kmetik, V., Kato, Y., Suzuki, M., Matsumura, M., Tajima, J., Nakayama, T., and Wilhein, T. (1999). Investigation of soft x-ray emission from a gas puff target irradiated with a Nd:YAG laser. *Optics Communications*, 163(1 - 3):103 – 114.

[Freund and Suresh, 2009] Freund, L. B. and Suresh, S. (2009). *Thin Film Materials: Stress, Defect Formation and Surface Evolution*. Cambridge University Press.

[Giannuzzi et al., 2005] Giannuzzi, L. A., Prenitzer, B. I., and W., K. B. (2005). Ion-solid interactions. In Giannuzzi, L. A. and Stevie, F. A., editors, *Introduction to focused ion beams: instrumentation, theory, techniques, and practice*. Springer.

[Gierak et al., 2009] Gierak, J., Bourhis, E., Faini, G., Patriarche, G., Madouri, A., Jede, R., Bruchhaus, L., Bauerdick, S., Schiedt, B., Biance, A. L., and Auvray, L. (2009). Exploration of the ultimate patterning potential achievable with focused ion beams. *Ultramicroscopy*, 109(5):457–462.

[Gierak et al., 2005] Gierak, J., Bourhis, E., Mérat Combes, M., Chriqui, Y., Sagnes, I., Mailly, D., Hawkes, P., Jede, R., Bruchhaus, L., Bardotti, L., Prével, B., Hannour, A., Mélinon, P., Perez, A., Ferré, J., Jamet, J.-P., Mougin, A., Chappert, C., and Mathet, V. (2005). Exploration of the ultimate patterning potential achievable with focused ion beams. *Microelectronic Engineering*, 78:266–278.

[Gierak et al., 2007] Gierak, J., Madouri, A., Bausells, J., Abadal, G., Pérez-Murano, F., Biance, A., Bourhis, E., Patriarche, G., Ulysse, C., Lucot, D., Lafosse, X., Auvray, L., Bruchhaus, L., and Jede, R. (2007). Sub-5nm FIB direct patterning of nanodevices. *Microelectronic Engineering*, 84(5):779–783.

[Guttmann et al., 2009] Guttmann, P., Zeng, X., Feser, M., Heim, S., Yun, W., and Schneider, G. (2009). Ellipsoidal capillary as condenser for the BESSY full-field x-ray microscope. *Journal of Physics: Conference Series*, 186(1):012064.

[Haase et al., 1997] Haase, A., Landwehr, G., and Umbach, E., editors (1997). *Rontgen Centennial: X-Rays in Natural and Life Sciences*. World Scientific Pub Co Inc.

[Henke et al., 1993] Henke, B., Gullikson, E., and Davis, J. (1993). X-ray interactions: photoabsorption, scattering, transmission, and reflection at E=50-30000 eV, Z=1-92. *Atomic Data and Nuclear Data Tables*, 54(2):181–342.

[Hertz et al., 2012] Hertz, H. M., von Hofsten, O., Bertilson, M., Vogt, U., Holmberg, A., Reinspach, J., Martz, D., Selin, M., Christakou, A. E., Jerlström-Hultqvist, J., and Svärd, S. (2012). Laboratory cryo soft X-ray microscopy. *Journal of Structural Biology*, 177:267–72.

[Hutchinson, 2002] Hutchinson, I. (2002). *Principles of Plasma Diagnostics*. Cambridge University Press.

[Ilinski et al., 2001] Ilinski, P. P., Lai, B. P., Bassom, N. J., Donald, J., and Athas, G. J. (2001). X-ray zone plate fabrication using a focused ion beam. *Proceedings of SPIE, Advances in X-Ray Optics*, 4145:311–316.

[Inkson et al., 2001] Inkson, B., Mulvihill, M., and Möbus, G. (2001). 3D determination of grain shape in a FeAl-based nanocomposite by 3D FIB tomography. *Scripta Materialia*, 45(7):753–758.

[Jansson et al., 2004] Jansson, P. A. C., Hansson, B. A. M., Hemberg, O., Otendal, M., Holmberg, A., de Groot, J., and Hertz, H. (2004). Liquid-tin-jet laser-plasma extreme ultraviolet generation. *Applied Physics Letters*, 84(13):2256–2258.

[Kaulich, 1996] Kaulich, B. (1996). *Phasenzonenplatten für die Röntgenmikroskopie im Photonenenergiebereich von 2-8 keV*. PhD thesis, Georg-August-Universität zu Göttingen.

[Kaulich et al., 2005] Kaulich, B., Bacescu, D., Susini, J., David, C., Fabrizio, E. D., Morrison, G. R., Charalambous, P., Thieme, J., Wilhein, T., Kovac, J., Cocco, D., Salome, M., Dhez, O., Weitkamp, T., Cabrini, S., Cojoc, D., Gianoncelli, A., Vogt, U., Podnar, M., Zangrando, M., Zacchigna, M., and Kiskinova, M. (2005). TwinMic - A European Twin X-ray Microscopy Station Commissioned at. *IPAP Conference Series*, 7:22–25.

[Keskinbora et al., 2013a] Keskinbora, K., Grévent, C., Bechtel, M., Weigand, M., Goering, E., Nadzeyka, A., Peto, L., Rehbein, S., Schneider, G., Follath, R., Vila-Comamala, J., Yan, H., and Schütz, G. (2013a). Ion beam lithography for Fresnel zone plates in X-ray microscopy. *Optics Express*, 21(10):11747–56.

[Keskinbora et al., 2013b] Keskinbora, K., Grevent, C., Eigenthaler, U., Weigand, M., and Schuetz, G. (2013b). Rapid prototyping of fresnel zone plates via direct ga+ ion beam lithography for high-resolution x-ray imaging. *ACS Nano*, 7(11):9788–9797.

[Kirkpatrick and Baez, 1948] Kirkpatrick, P. and Baez, A. V. (1948). Formation of optical images by x-rays. *Journal of the Optical Society of America*, 38(9):766–773.

[Kirz and Jacobsen, 2009] Kirz, J. and Jacobsen, C. (2009). The history and future of X-ray microscopy. *Journal of Physics: Conference Series*, 186:012001.

[Klimontovich, 1967] Klimontovich, I. (1967). *The statistical theory of non-equilibrium processes in a plasma*. International series of monographs in natural philosophy. M.I.T. Press.

[Kohn, 1995] Kohn, V. G. (1995). On the theory of reflectivity by an x-ray multilayer mirror. *physica status solidi (b)*, 187(1):61–70.

[Kramida et al., 2013] Kramida, A., Yu. Ralchenko, Reader, J., and and NIST ASD

Team (2013). NIST Atomic Spectra Database (ver. 5.1), [Online]. Available: `http://physics.nist.gov/asd` [2013, November 29]. National Institute of Standards and Technology, Gaithersburg, MD.

[Lebert et al., 1999] Lebert, R., Bergmann, K., Schriever, G., and Neff, W. (1999). Comparison of laser produced and gas discharge based EUV sources for different applications. *Microelectronic Engineering*, 46(1-4):465–468.

[Lee et al., 1987] Lee, T. N., McLean, E. A., and Elton, R. C. (1987). Soft x-ray lasing in neonlike germanium and copper plasmas. *Physical Review Letters*, 59:1185–1188.

[Lenz, 2009] Lenz, J. (2009). Direct Structuring of Diffraction Gratings for XUV Applications by 30 kV Gallium Ions. Master's thesis, FH Koblenz, RheinAhrCampus Remagen and research center caesar Bonn.

[Lenz et al., 2011] Lenz, J., Krupp, N., Wilhein, T., and Irsen, S. (2011). Nanofabrication of optical elements for sxr and euv applications: Ion beam lithography as a new approach. *AIP Conference Proceedings*, 1365(1):104–107.

[Lenz et al., 2009] Lenz, J., Wilhein, T., and Irsen, S. (2009). Nanofabrication of diffractive elements for soft x-ray and extreme ultraviolet applications using ion beam lithography. *Applied Physics Letters*, 95(19):191118.

[Li-Jun et al., 1994] Li-Jun, L., Cocco, D., and Jark, W. (1994). Simple plane grating monochromator for synchrotron radiation. *Nuclear Instruments and Methods in Physics Research Section A: Accelerators, Spectrometers, Detectors and Associated Equipment*, 339(3):604 – 609.

[Lindblom et al., 2007] Lindblom, M., Tuohimaa, T., Holmberg, A., Wilhein, T., Hertz, H. M., and Vogt, U. (2007). High-resolution differential interference contrast x-ray zone plates: Design and fabrication. *Spectrochimica Acta Part B: Atomic Spectroscopy*, 62(6-7):539 – 543.

[Matthijs De Winter et al., 2009] Matthijs De Winter, D. A., Schneijdenberg, C. T. W. M., Lebbink, M. N., Lich, B., Verkleij, a. J., Drury, M. R., and Humbel, B. M. (2009). Tomography of insulating biological and geological materials using focused ion beam (FIB) sectioning and low-kV BSE imaging. *Journal of microscopy*, 233(3):372–83.

[Mayer et al., 2011] Mayer, M., Grévent, C., Szeghalmi, a., Knez, M., Weigand, M., Rehbein,

S., Schneider, G., Baretzky, B., and Schütz, G. (2011). Multilayer Fresnel zone plate for soft X-ray microscopy resolves sub-39nm structures. *Ultramicroscopy*, 111(12):1706–11.

[Michette, 1986] Michette, A. G. (1986). *Optical systems for soft X rays*. Plenum Press New York.

[Michette, 1990] Michette, a. G. (1990). Laser-generated plasmas: source requirements for x-ray microscopy. *Journal of X-ray Science and Technology*, 2(1):1–16.

[Nano-FIB, 2002] Nano-FIB (2002). `ftp://ftp.cordis.europa.eu/pub/nanotechnology/docs/n_s_nanofib_27052002.pdf`. *Last checked 2013-11-06*.

[Niemann et al., 2001] Niemann, B., Guttmann, P., Hambach, D., Schneider, G., Weiß, D., and Schmahl, G. (2001). A rotating condenser and off-axis zone plate monochromator for the txm at the undulator u41 at bessy ii. *Nuclear Instruments and Methods in Physics Research Section A: Accelerators, Spectrometers, Detectors and Associated Equipment*, 467–468, Part 2(0):857 – 860.

[Niemann et al., 1974] Niemann, B., Rudolph, D., and Schmahl, G. (1974). Soft x-ray imaging zone plates with large zone numbers for microscopic and spectroscopic applications. *Optics Communications*, 12(2):4–7.

[Niemann et al., 1976] Niemann, B., Rudolph, D., and Schmahl, G. (1976). X-ray microscopy with synchrotron radiation. *Applied Optics*, 15(8):1883–1884.

[Ohring, 1991] Ohring, M. (1991). *Materials Science of Thin Films, Second Edition*. Academic Press.

[Orloff et al., 2003] Orloff, J., Swanson, L., and Utlaut, M. W. (2003). *High resolution focused ion beams: FIB and its applications: the physics of liquid metal ion sources and ion optics and their application to focused ion beam technology*. Kluwer Academic/Plenum Publishers.

[Overbuschmann et al., 2012] Overbuschmann, J., Hengster, J., Irsen, S., and Wilhein, T. (2012). Fabrication of Fresnel zone plates by ion-beam lithography and application as objective lenses in extreme ultraviolet microscopy at 13 nm wavelength. *Optics Letters*, 37(24):5100–5102.

[Piel, 2010] Piel, A. (2010). *Plasma physics: An Introduction to laboratory, space, and fusion plasmas*. Springer.

[Rehbein, 2001] Rehbein, S. (2001). *Entwicklung von freitragenden nanostrukturierten Zonenplatten zur Fokussierung und Monochromatisierung thermischer Helium-Atomstrahlen*. PhD thesis, Georg-August-Universität zu Göttingen.

[Reinspach et al., 2009] Reinspach, J., Lindblom, M., von Hofsten, O., Bertilson, M., Hertz, H. M., and Holmberg, A. (2009). Cold-developed electron-beam-patterned ZEP 7000 for fabrication of 13 nm nickel zone plates. *Journal of Vacuum Science & Technology B: Microelectronics and Nanometer Structures*, 27(6):2593.

[Rudolph et al., 1982] Rudolph, D., Niemann, B., and Schmahl, G. (1982). Status of the sputtered sliced zone plates for x-ray microscopy. *Proceedings of SPIE, High Resolution Soft X-Ray Optics*, 0316:103–105.

[Rymell and Hertz, 1993] Rymell, L. and Hertz, H. (1993). Droplet target for low-debris laser-plasma soft x-ray generation. *Optics Communications*, 103(1–2):105 – 110.

[Schaefer et al., 2009a] Schaefer, D., Benk, M., Bergmann, K., Nisius, T., Wiesemann, U., and Wilhein, T. (2009a). Optical setup for tabletop soft x-ray microscopy using electrical discharge sources. *Journal of Physics: Conference Series*, 186(1):012033.

[Schaefer et al., 2009b] Schaefer, D., Wiesemann, U., Nisius, T., and Wilhein, T. (2009b). Degradation of thin-film filters irradiated by debris emission of a laser induced plasma. *Proceedings of SPIE, Damage to VUV, EUV and X-Ray Optics II*, 7361:73610V–73610V–8.

[Schäfer, 2010] Schäfer, D. (2010). *Entwicklung eines Transmissionsmikroskops für weiche Röntgenstrahlung und die Anwendung an Laborquellen*. PhD thesis, Julius-Maximilians-Universität Würzburg.

[Schmahl and Rudolph, 1969] Schmahl, G. and Rudolph, D. (1969). Lichtstarke Zonenplatten als abbildende Systeme für weiche Röntgenstrahlung. *Optik*, 29(6):577–585.

[Schmahl et al., 1982] Schmahl, G., Rudolph, D., and Niemann, B. (1982). Röntgenmikroskopie mit hoher Auflösung. *Physikalische Blätter*, 38(9):283–286.

[Schnopper et al., 1977] Schnopper, H. W., Speybroeck, L. P. V., Delvaille, J. P., Epstein, A.,

Källne, E., Bachrach, R. Z., Dijkstra, J., and Lantward, L. (1977). Diffraction grating transmission efficiencies for xuv and soft x rays. *Applied Optics*, 16(4):1088–1091.

[Sigmund, 1969] Sigmund, P. (1969). Theory of sputtering. i. sputtering yield of amorphous and polycrystalline targets. *Physical Review*, 184(2):383–416.

[Sigmund, 1981] Sigmund, P. (1981). Sputtering by ion bombardment theoretical concepts. In Behrisch, R., editor, *Sputtering by Particle Bombardment I*, volume 47 of *Topics in Applied Physics*, pages 9–71. Springer Berlin Heidelberg.

[Soret, 1875] Soret, J. L. (1875). Ueber die durch Kreisgitter erzeugten Diffractionsphänomene. *Annalen der Physik und Chemie*, 156:99–113.

[Spiller, 1994] Spiller, E. (1994). *Soft X-Ray Optics*. Society of Photo Optical, first edition edition.

[Stevie et al., 2005] Stevie, F. A., Giannuzzi, L. A., and Prenitzer, B. I. (2005). The focused ion beam instrument. In Giannuzzi, L. A. and Stevie, F. A., editors, *Introduction to focused ion beams: instrumentation, theory, techniques, and practice*. Springer.

[Surpi et al., 2007] Surpi, A., Valizadeh, S., Leifer, K., and Lagomarsino, S. (2007). Focused ion beam fabrication procedures of x-ray micro fresnel zone plates. *Journal of Micromechanics and Microengineering*, 17(3):617–622.

[Takman et al., 2007] Takman, P. a. C., Stollberg, H., Johansson, G. a., Holmberg, A., Lindblom, M., and Hertz, H. M. (2007). High-resolution compact X-ray microscopy. *Journal of Microscopy*, 226(Pt 2):175–81.

[Thornton, 1974] Thornton, J. A. (1974). Influence of apparatus geometry and deposition conditions on the structure and topography of thick sputtered coatings. *Journal of Vacuum Science and Technology*, 11(4):666.

[Tseng, 2007] Tseng, A. A. (2007). Fabrication of nanoscale structures using ion beams. In Yao, N., editor, *Focused Ion Beam Systems: Basics and Applications*. Cambridge University Press.

[Viefhaus et al., 2013] Viefhaus, J., Scholz, F., Deinert, S., Glaser, L., Ilchen, M., Seltmann, J., Walter, P., and Siewert, F. (2013). The variable polarization {XUV} beamline {P04} at {PETRA} iii: Optics, mechanics and their performance. *Nuclear Instruments and Methods*

in Physics Research Section A: Accelerators, Spectrometers, Detectors and Associated Equipment, 710(0):151 – 154. The 4th international workshop on Metrology for X-ray Optics, Mirror Design, and Fabrication.

[Vila-Comamala et al., 2009] Vila-Comamala, J., Jefimovs, K., Raabe, J., Pilvi, T., Fink, R. H., Senoner, M., Maassdorf, A., Ritala, M., and David, C. (2009). Advanced thin film technology for ultrahigh resolution X-ray microscopy. *Ultramicroscopy*, 109(11):1360–4.

[Voges, 1993] Voges, W. (1993). The ROSAT all-sky survey. *Advances in Space Research*, 13(12):391–397.

[Vogt, 1999] Vogt, U. (1999). *Laserinduziertes Plasma als Strahlungsquelle für weiche Röntgenstrahlung*. Diploma thesis, Georg-August-Universität Göttingen.

[Vogt, 2002] Vogt, U. (2002). *Röntgenemission aus laserinduzierten Plasmen: Einfluss von Laserintensität und Pulsdauer bei verschiedenen Targetsystemen*. PhD thesis, Technische Universität Berlin.

[Vogt et al., 2004] Vogt, U., Früke, R., Stollberg, H., Jansson, P. A. C., and Hertz, H. M. (2004). High-resolution spatial characterization of laser produced plasmas at soft x-ray wavelengths. *Applied Physics B*, 58:53–58.

[Vogt et al., 2006] Vogt, U., Lindblom, M., Charalambous, P., Kaulich, B., and Wilhein, T. (2006). Condenser for koehler-like illumination in transmission x-ray microscopes at undulator sources. *Optics Letters*, 31(10):1465–1467.

[Vogt et al., 2001] Vogt, U., Stiel, H., Will, I., Nickles, P. V., Sandner, W., Wieland, M., and Wilhein, T. (2001). Influence of laser intensity and pulse duration on the extreme ultraviolet yield from a water jet target laser plasma. *Applied Physics Letters*, 79(15):2336–2338.

[Volkert et al., 2007] Volkert, C., Minor, A., and guest editors (2007). Focused ion beam microscopy and micromachining. *MRS Bulletin*, 32:389–395.

[Wessels et al., 2013] Wessels, P., Schlie, M., Wieland, M., Ewald, J., Abbati, G., Baumbach, S., Overbuschmann, J., Nisius, T., Vogel, A., Neumann, A., Meents, A., Viefhaus, J., Oepen, H. P., Meier, G., Wilhein, T., and Drescher, M. (2013). Xmcd microscopy with synchronized soft x-ray and laser pulses at petra iii for time-resolved studies. *Journal of Physics: Conference Series*, 463(1):012023.

[Wieland, 2004] Wieland, M. (2004). *Entwicklung hochauflösender röntgenoptischer Verfahren für Hohe-Harmonische-Strahlung im extrem ultravioletten Spektralbereich*. PhD thesis, Rheinische Friedrich-Wilhelms-Universität Bonn.

[Wilhein et al., 1999] Wilhein, T., Rehbein, S., Hambach, D., Berglund, M., Rymell, L., and Hertz, H. M. (1999). A slit grating spectrograph for quantitative soft x-ray spectroscopy. *Review of Scientific Instruments*, 70(3):1694–1699.

[Wolter, 1952] Wolter, H. (1952). Spiegelsysteme streifenden Einfalls als abbildende Optiken für Röntgenstrahlen. *Annalen der Physik*, 445(1-2):94–114.

[Yao, 2007] Yao, N. (2007). Introduction to the focused ion beam system. In Yao, N., editor, *Focused Ion Beam Systems: Basics and Applications*. Cambridge University Press.

List of Figures

List of Tables

Danksagung

An dieser Stelle möchte ich allen Menschen danken, die mich während der Anfertigung der vorliegenden Arbeit auf vielfältige Art und Weise unterstützt haben:

Ganz besonders möchte ich mich bei Herrn Prof. Dr. Stefan Linden bedanken, der sich bereit erklärt hat, mich als externes Mitglied in seine Gruppe aufzunehmen, um mein Promotionsprojekt von universitärer Seite zu betreuen. Herrn Prof. U. Benjamin Kaupp danke ich für seine Unterstützung bei caesar und für die Übernahme des Zweitgutachtens.

Ich möchte Herrn Prof. Dr. Thomas Wilhein danken, der mich schon während des Studiums gefördert und unterstützt hat. Mein Dank gilt auch Herrn Dr. Stephan Irsen, der mich seit meiner Zeit als Master-Student in seiner Gruppe beherbergt hat. Beiden danke ich besonders für ihr Vertrauen, die vielen fruchtbaren Diskussionen und Anregungen; ohne Euch wäre meine Arbeit nicht möglich gewesen.

Allen jetzigen aber auch früheren Mitarbeitern der Forschungsgruppe EMA bei caesar danke ich für die mehr als angenehme Arbeitsatmosphäre und die vielen wertvollen Anregungen und Hilfestellungen. Besonders möchte ich Angelika Sehrbrock danken, die mir ihre FIB-Fähigkeiten auf die beste Art und Weise vermittelt hat. Dem gesamten IXO-Team am RheinAhrCampus, Johannes Ewald, Thomas Nisius, Stefan Baumbach und Gennaro Abbati danke ich für die vielen erfolgreichen, aber auch für die frustrierenden Experimentiertage und Strahlzeiten. Auch Julia Hengster und Nikolai Krupp möchte ich für die Unterstützung durch ihre Arbeiten im Labor besonders danken. Für die vielfältige Unterstützung während meines Promotionsprojekts sei dem IBL-Team der Raith GmbH, Sven Bauerdick und Achim Nadjzeyka, sowie dem TwinMic-Team bei Elettra in Triest gedankt. Für die Unterstützung bei Petra III danke ich Philipp Wessels, Marek Wieland, Leif Glaser und Jens Viefhaus. Außerdem gilt mein Dank den Mitgliedern der AG Nanophotonik der Universität Bonn für ihre vielfältige Hilfe, im Besonderen Felix von Cube für die Auflockerung des Labor-Alltags.

Mein größter Dank gilt schließlich meiner Frau Friederike für ihre fortwährende und bedingungslose Unterstützung. Meiner Tochter Charlotte danke ich für Ihre Existenz. Außerdem danke ich meiner Familie, meinen Eltern und meiner Schwiegermutter für deren Rückhalt während der Zeit meiner wissenschaftlichen Ausbildung.